UNIVERSITY OF ILLINOIS
URBANA

AERONOMY REPORT
NO. 34

PRODUCTION AND LOSS OF O(^{1}D) IN THE NIGHTTIME F REGION

by
Jeffrey M. Forbes

January 1, 1970

FACILITY FORM 602

N70-20444 (ACCESSION NUMBER)	(THRU)
112 (PAGES)	1 (CODE)
CR-108932 (NASA CR OR TMX OR AD NUMBER)	13 (CATEGORY)

MAR 1970
RECEIVED
NASA STI FACILITY
INPUT BRANCH

Supported by
National Aeronautics and Space Administration
Grant ~~NGR-11~~3 NGR-14-005-013

Aeronomy Laboratory
Department Electrical Engineering
University of Illinois
Urbana, Illinois

AERONOMY REPORT

NO. 34

PRODUCTION AND LOSS OF O(^{1}D) IN THE NIGHTTIME F REGION

by

Jeffrey M. Forbes

January 1, 1970

Aeronomy Laboratory
Department of Electrical Engineering
University of Illinois
Urbana, Illinois

Supported by
National Aeronautics and Space Administration
Grant ~~NGR-013~~ NGR-14-005-013

ABSTRACT

This paper is a study of the production and loss of $O(^1D)$ in the nighttime F region. Quenching of $O(^1D)$ is studied in detail, and is concluded to be an important mechanism in the OI(6300Å) night airglow. In addition, the dissociative recombination of O_2^+ is found to yield .12 ± .06 $O(^1D)$ atoms per recombination. This result is accomplished by comparing theoretical calculations of the OI(6300Å) night airglow vertical volume emission rate with ground-based photometer observations of OI(6300Å).

The experimental program is also described, and methods of data analysis are presented. Suggestions are made for future work on the OI(6300Å) night airglow at the University of Illinois.

ACKNOWLEDGEMENTS

Professor S. A. Bowhill is deserving of my sincerest thanks for his consistent encouragement and interest in my work.

I also wish to acknowledge the other members of the Aeronomy Laboratory for their helpful assistance. The efforts of Stanley Bengston (instrumentation) and Clayton Hull (data collection and calculations) are especially appreciated.

[redacted]

TABLE OF CONTENTS

TABLE OF CONTENTS (continued)

LIST OF FIGURES

LIST OF FIGURES (continued)

LIST OF FIGURES (continued)

LIST OF TABLES

1. REVIEW OF THE CHARACTERISTICS OF THE OI(6300Å) NIGHT AIRGLOW

1.1 Spectral Characteristics

Since about the year 1900 men have recognized the existence of a terrestrial component to the light of the night sky. Chamberlain (1961) gives a concise historical summary of early observations and investigations of this phenomenon. Most of these atmospheric optical emissions can be placed under one of two general classifications: aurora or airglow. Chamberlain (1961) defines aurora as the sporadic electromagnetic radiation that is emitted from the atmosphere and induced by extra-atmospheric atomic or subatomic particles, whereas airglow has its origin in photochemical reactions.

The OI(6300Å) night airglow is one of many optical emissions originating in the earth's upper atmosphere. OI(6300Å) is a shorthand notation used to indicate that the source of the 6300Å emission is the ^1D excited state of neutral atomic oxygen. Figure 1.1 illustrates a portion of the night airglow spectrum recently observed by Broadfoot and Kendall (1968). The spectrum between 6200Å and 6400Å contains the OI(6300Å) and OI(6364Å) lines and the OH(9-3) hydroxyl band. Under quiet or slightly disturbed geomagnetic conditions in non-polar regions, the nighttime intensity of OI(6300Å) usually lies between 50 and 100 Rayleighs (Chamberlain, 1961). One Rayleigh (R) is an apparent emission rate of 10^6 photons cm^{-2} (column) sec^{-1}. The reason for these units will become clear in Section 3.4.

1.2 Height Distribution

The 6300Å emission, or red line of atomic oxygen as it is sometimes called, is usually observed with highly sensitive instruments from the ground. Although these instruments are capable of being carried aloft by rockets,

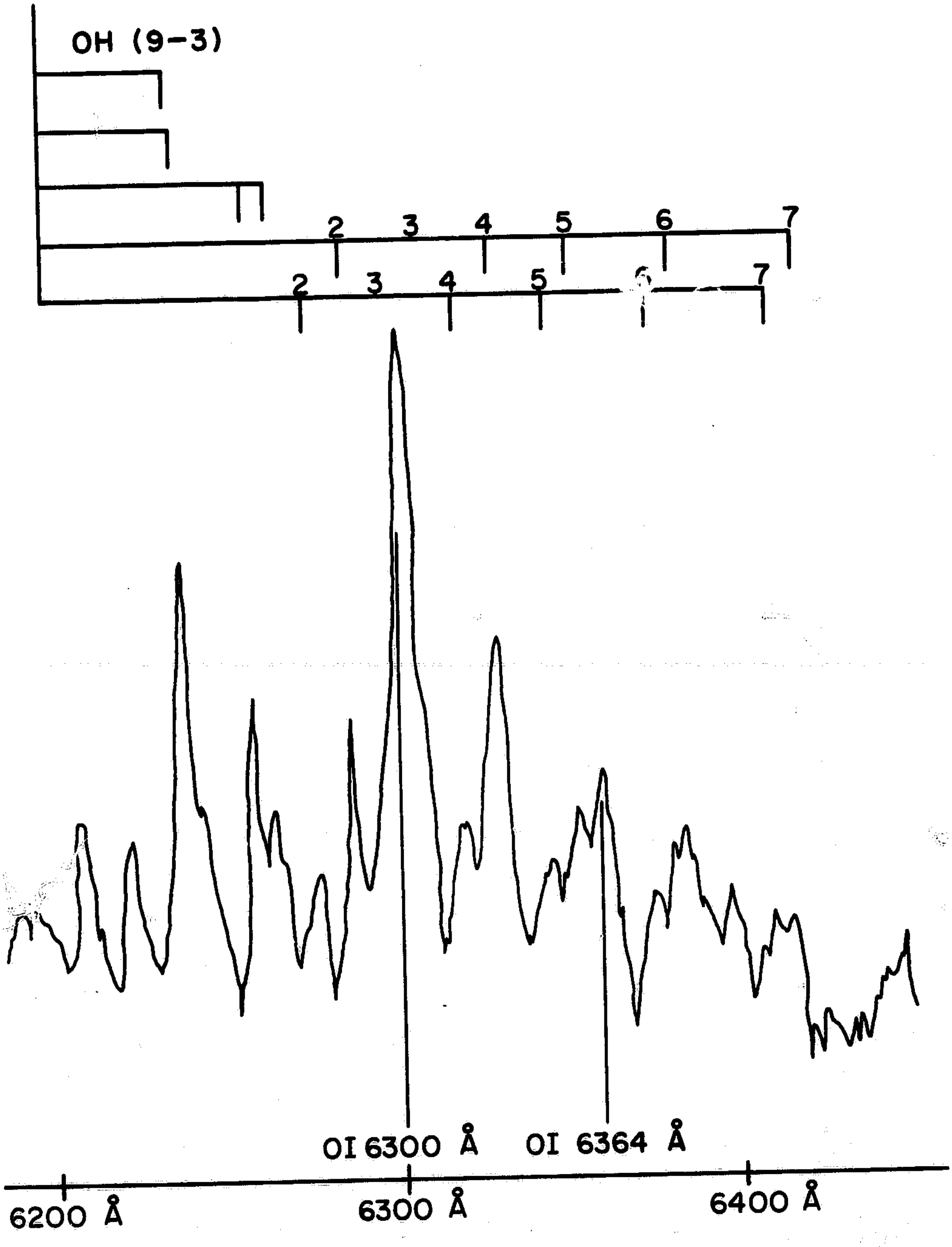

Figure 1.1 The night airglow spectrum near 6300Å (Broadfoot and Kendall, 1968).

this method has economic disadvantages and does not allow observation of the phenomenon for any more than a few minutes. An advantage of the rocket technique is that it allows determination of the height distribution of the emitting layer. With the rocket traveling upwards monitoring airglow intensities in the zenith, the airglow intensity remains constant until the emitting region is reached, decreases as the rocket passes through it, and is zero after emerging from the layer. Gulledge et al. (1968) used this technique and observed a layer with peak intensity at 245 km and a thickness of about 75 km. These observations are in agreement with calculations made with ground-based data taken at the same time and location.

1.3 Global Morphology

Shipboard observations (Nakamura, 1961; Davis and Smith, 1965; Greenspan, 1966) have revealed a latitude dependence of the red-line intensity. The intensities in the equatorial zone are generally stronger and undergo a larger variation than at other latitudes. The nighttime variation common to all latitudes is a post-twilight decay and an increase at dawn. At mid-latitudes the intensity usually reaches a minimum around midnight, and remains relatively constant until just before dawn. An intensity maximum is observed near local midnight in the equatorial regions, especially near 15° N and S geomagnetic latitudes. This maximum in intensity is followed by a gradual decrease afterwards. Deviations from the general behavior outlined above occur under geomagnetically disturbed conditions.

1.4 Time Variations

1.4.1 Seasonal variations

Evidence of a seasonal variation of red-line intensity is indicated by data taken at Kitt Peak, Arizona (lat. 32.0°N), and Haleakala (lat. 20.7°N)

(Smith and Steiger, 1968). Their observations of a maximum in summer and minimum in winter are in agreement with the shipboard observations of Davis and Smith (1965).

1.4.2 Nighttime variations

Although the red-line intensity has immense diurnal variations (Noxon, 1968), only variations during the night will be considered in this section. Bellew and Silverman (1966) have classified the general behavior of the 6300Å night-glow emission at Sacramento Peak, New Mexico (geographic lat. 32°43'N; long 105°45'W) into three groups (see Figure 1.2) according to correlation with the planetary magnetic index K_p and variation during the night:

I. Monotonic decrease following sunset to a minimum during the middle of the night usually followed by a pre-dawn increase. By comparison with observations at other stations, Bellew and Silverman conclude that this is the normal red-line behavior in temperate latitudes. This type of activity occurs during quiet or slightly disturbed geomagnetic conditions ($K_p \leq 3$).

II. Variable emission occurring on magnetically disturbed nights or on nights preceded by periods of high magnetic activity ($K_p \geq 4$). This type of variation is much more frequent during sunspot maximum than sunspot minimum, even for high K_p during sunspot minimum.

III. Variation with a maximum occurring between 0000 and 0200 hours local time. This is a northern extension of the equatorial behavior, and is seen much more often when the photometer is pointed towards the south instead of the zenith direction. This type of behavior often occurs on nights of high geomagnetic activity ($K_p \geq 4$).

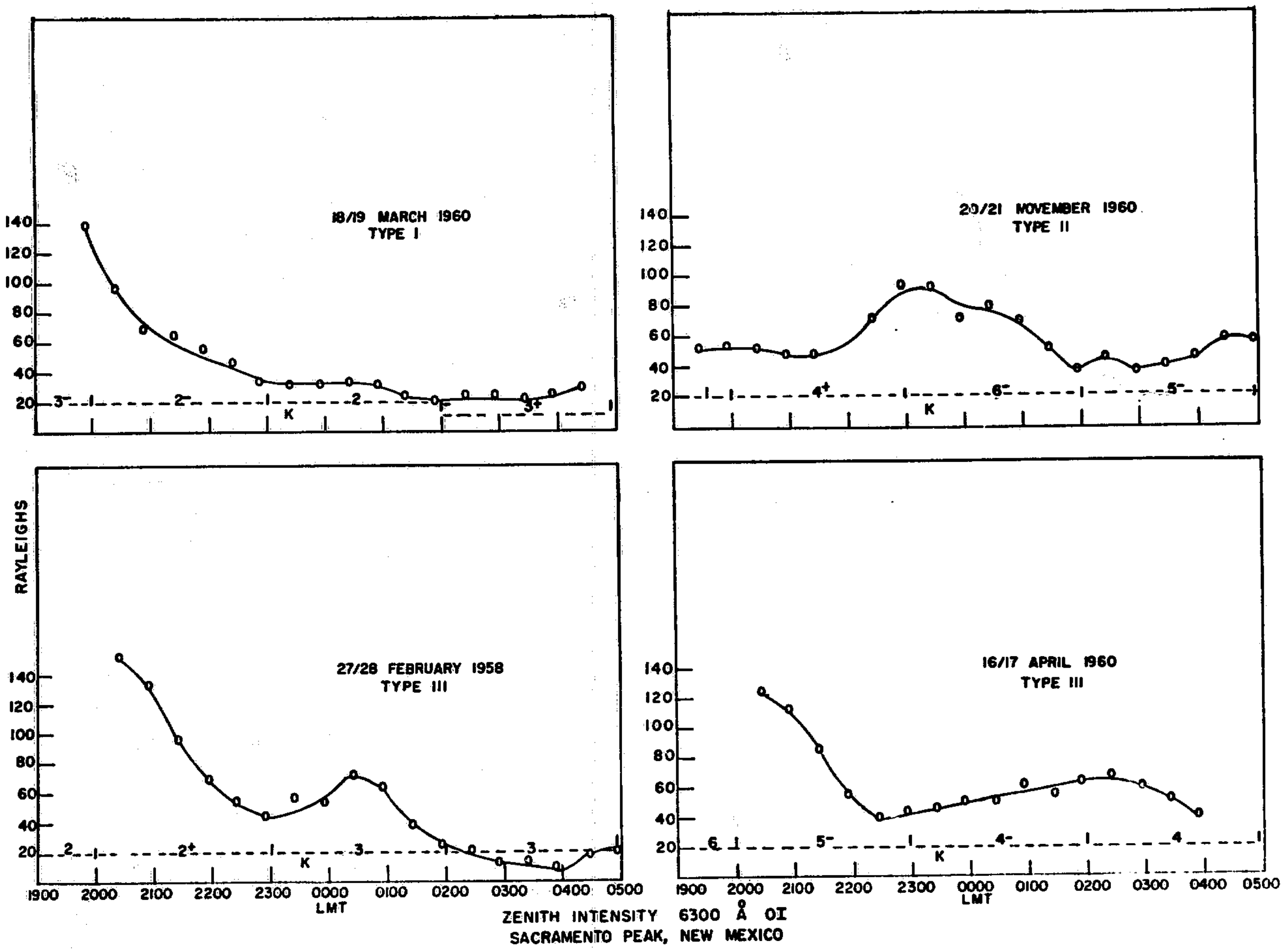

Figure 1.2 Examples of typical red line behavior at Sacramento Peak, New Mexico and the corresponding K_p (Bellew and Silverman, 1966).

1.5 Relationship to Ionization Density

It was previously mentioned that the OI(6300Å) emission was produced by radiative transitions of excited oxygen atoms. A major source of the excited atomic oxygen atoms responsible for this emission is the dissociative recombination of photoionization products created during the day by solar radiation:

$$XY^{+} + e \rightarrow X^{*} + Y^{*} \qquad (1.1)$$

where the asterisk denotes possible excited states of the atoms X and Y. This mechanism was first proposed by Bates (1946) and has since been verified by a number of workers, the most complete discussion of both theory and experiment being presented by Peterson *et al*. (1966).

Thus from reaction (1.1) the red-line intensity depends largely on the concentrations of XY^{+} and e and their rate of recombination. Vertical excursions are sometimes observed in the height of the F2 layer, especially near the equator (Van Zandt and Peterson, 1968). Downward movements of the layer increase the total number of available participants in the dissociative recombination reaction (1.1), thereby causing an increased production of X^{*} and Y^{*}, and a subsequent enhancement in the red line intensity. Van Zandt and Peterson (1968) propose that these vertical movements in the tropical region are caused by electromagnetic drifts which are in turn caused by westward electric fields originating in the E region. This theory is substantiated by experimental evidence (Balsley, 1969) which shows that the downward drift velocity of ionization in the equatorial F region is controlled by westward electric fields. It is this movement of the F2 layer in equatorial regions which causes the observed red line enhancements mentioned in Section 1.3.

2. THEORY OF THE OI(6300Å) NIGHT AIRGLOW

2.1 How the Emission is Produced

The excited states of atomic oxygen undergo depopulation by radiative transition, thus producing the quanta of light which constitute the airglow, the wavelength being proportional to the difference in energy of the levels between which the transitions take place. The low-energy portion of the energy-level diagram for atomic oxygen is shown in Figure 2.1. A is the Einstein coefficient of spontaneous emission for an energy level and is a measure of the probability that a transition will take place from that level in one second. The lifetime of this level is the reciprocal of the Einstein coefficient. The values of A for each transition appear in parentheses following the wavelength of the transition. The lifetime for $O(^1D)$ is rather long (110 sec) and hence $O(^1D)$ is called a metastable state.

A comparison of the Einstein coefficients for the various transitions gives an indication of the relative intensities of the different emissions providing the excited states are undisturbed by collisions. Take the ^1D state for instance. There are three possible transitions:

$$^1D \xrightarrow{6392\text{Å}} {}^3P_0$$

$$^1D \xrightarrow{6364\text{Å}} {}^3P_1$$

$$^1D \xrightarrow{6300\text{Å}} {}^3P_2$$

with respective Einstein coefficients 1.1×10^{-6} sec^{-1}, 2.2×10^{-3} sec^{-1}, and 6.9×10^{-3} sec^{-1}. Thus the probability that a 6392Å photon will be emitted is relatively small, and its contribution to the total emission from the ^1D level is negligible. A 6364Å emission occurs about one third as often as a 6300Å emission.

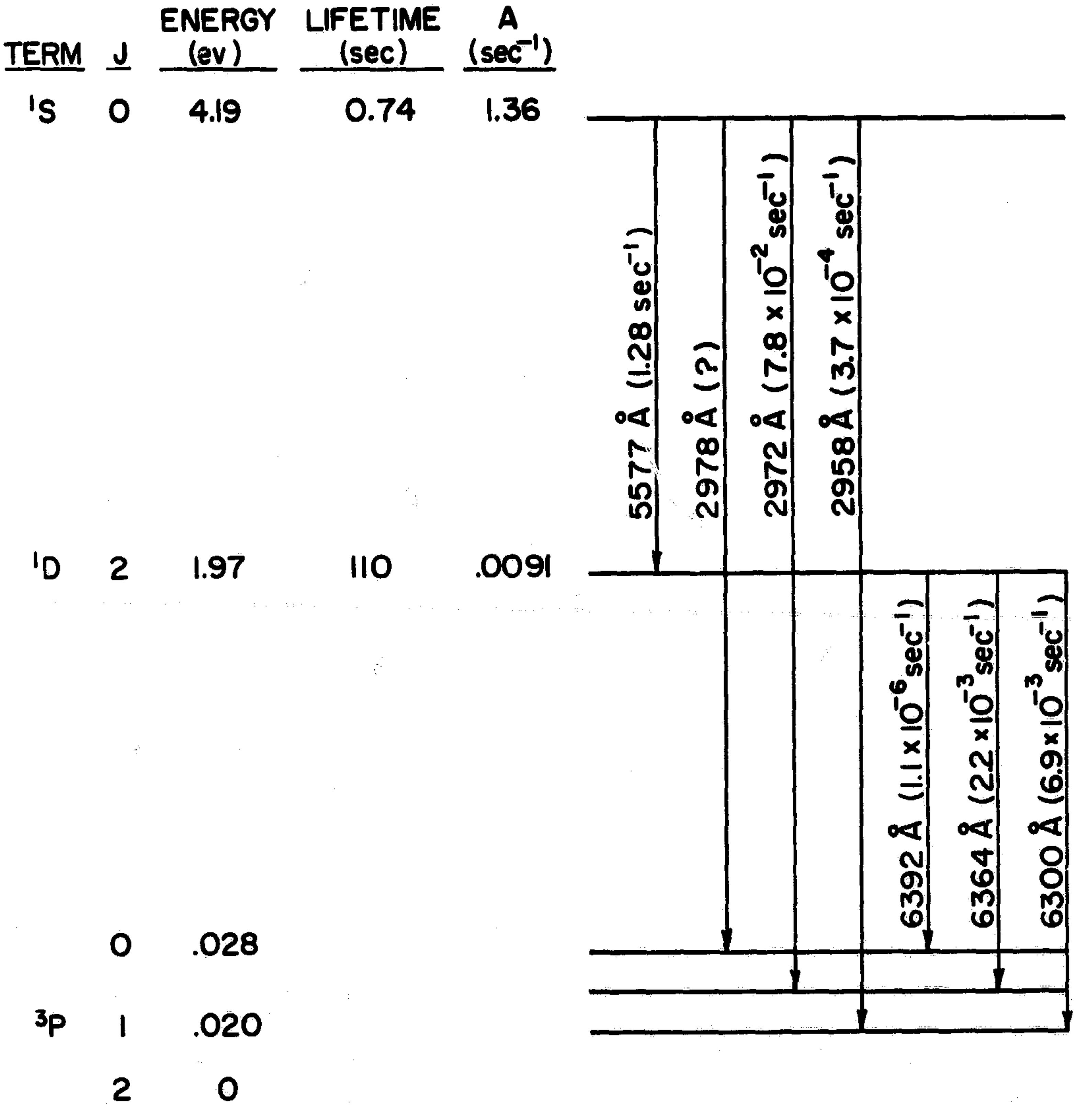

Figure 2.1 Low energy portion of the atomic oxygen energy level diagram (after Peterson *et al.*, 1966).

2.2 Excitation of $O(^1D)$ by Dissociative Recombination

The dissociative recombination of O_2^+ can produce several combinations of products:

$$O_2^+ + e \rightarrow O(^3P) + O(^3P) \qquad (2.1)$$

$$O_2^+ + e \rightarrow O(^3P) + O(^1D) \qquad (2.2)$$

$$O_2^+ + e \rightarrow O(^1D) + O(^1D) \qquad (2.3)$$

$$O_2^+ + e \rightarrow O(^1D) + O(^1S) \qquad (2.4)$$

The $O(^1D)$ then gives rise to the red line:

$$O(^1D) \rightarrow O(^3P) + h\nu \qquad (2.5)$$

There is some doubt as to whether the dissociative recombination of NO^+, which can follow either of the two reactions:

$$NO^+ + e \rightarrow N(^4S) + O(^1D) \qquad (2.6)$$

$$NO^+ + e \rightarrow N(^2D) + O(^3P) \quad , \qquad (2.7)$$

should be included in the theory of the 6300Å night airglow. Dalgarno and Walker (1964) point out that excitation of the O atom to the (^1D) level in reaction (2.6) violates conservation of spin. Although Peterson et al. (1966) suggest the alternative possibility of $O(^1D)$ formation by quenching (collisional deactivation) of $N(^2D)$ by $O(^3P)$, Wallace and McElroy (1966) suggest that quenching of $N(^2D)$ by O is unlikely, adding that the most likely quenching agent is probably O_2. Apparently neither (2.6) nor (2.7) is capable of producing a significant amount of $O(^1D)$. However, the possibility of a contribution from the dissociative recombination of NO^+ will be included in the discussion in Chapter 7. It is shown in Chapter 3 that during the night, the relative contribution to the airglow intensity of reactions (2.6) and (2.7) as opposed to (2.2) through (2.4) is given approximately by K_{D_2}/K_{D_1}, where:

K_{D_1} = number of excitations of $O(^1D)$ per recombination for O_2^+

K_{D_2} = number of excitations of $O(^1D)$ per recombination for NO^+ .

Therefore, a K_{D_1} determined in the data analysis (assuming the airglow is due only to dissociative recombination of O_2^+) which is greater than the maximum possible value of 2 would lead one to suspect that perhaps reaction (2.6) or (2.7) should be included in the theory.

Molecular oxygen ions are provided by the charge transfer mechanism

$$O^+ + O_2 \xrightarrow{\gamma_1} O_2^+ + O \qquad (2.8)$$

and NO^+ by the ion-atom interchange reaction

$$O^+ + N_2 \xrightarrow{\gamma_2} NO^+ + N \quad . \qquad (2.9)$$

The OI(6300Å) night airglow is known to be produced almost exclusively by dissociative recombination of O_2^+ and possibly NO^+. Airglow intensities calculated using this theory (Peterson and Steiger, 1966) have been in fairly good agreement with experimentally measured values. The agreement between theory and experiment has not been perfect however. One of the important factors which needs to be considered is the efficiency of the dissociative recombination reactions in producing O(^{1}D), namely the fraction of all recombinations which result in the production of an oxygen atom in the ^{1}D state. Also, one must consider the possibility that the O(^{1}D) atom will be collisionally deactivated before it has an opportunity to emit a 6300Å photon. These problems will be considered in detail in later sections. For the present, an additional means will be considered of exciting an oxygen atom to its ^{1}D state: excitation by inelastic collisions with photoelectrons.

2.3 Excitation of O(^{1}D) by Photoelectrons

Cole (1965) suggested that Barbier's (1959) observation of an enhancement in red-line intensity before dawn could be caused by photoelectrons which are produced by photoionization in the sunlit magnetically conjugate F region and stream along magnetic field lines to the region of observation. Hanson (1963) has shown that a sufficient flux of photoelectrons in the 10-30 eV range can escape upward after photodissociation to produce the observed conjugate effect. These electrons then spiral along magnetic field lines to the conjugate ionosphere where they first heat the upper F region through collisions with ambient electrons and lose the rest of their energy below 300 km through inelastic collisions with atomic oxygen (Cole, 1965; Carlson, 1966b). It is these inelastic collisions which excite the atomic oxygen atoms to their ^{1}D state. The O(^{1}D) then undergoes radiative transition and hence the red line enhancement. Some of Barbier's (1959) measurements are illustrated in Figure 2.2, showing large enhancements in red-line intensity well before dawn. Barbier points out that this behavior is most pronounced in winter and periods of high solar activity.

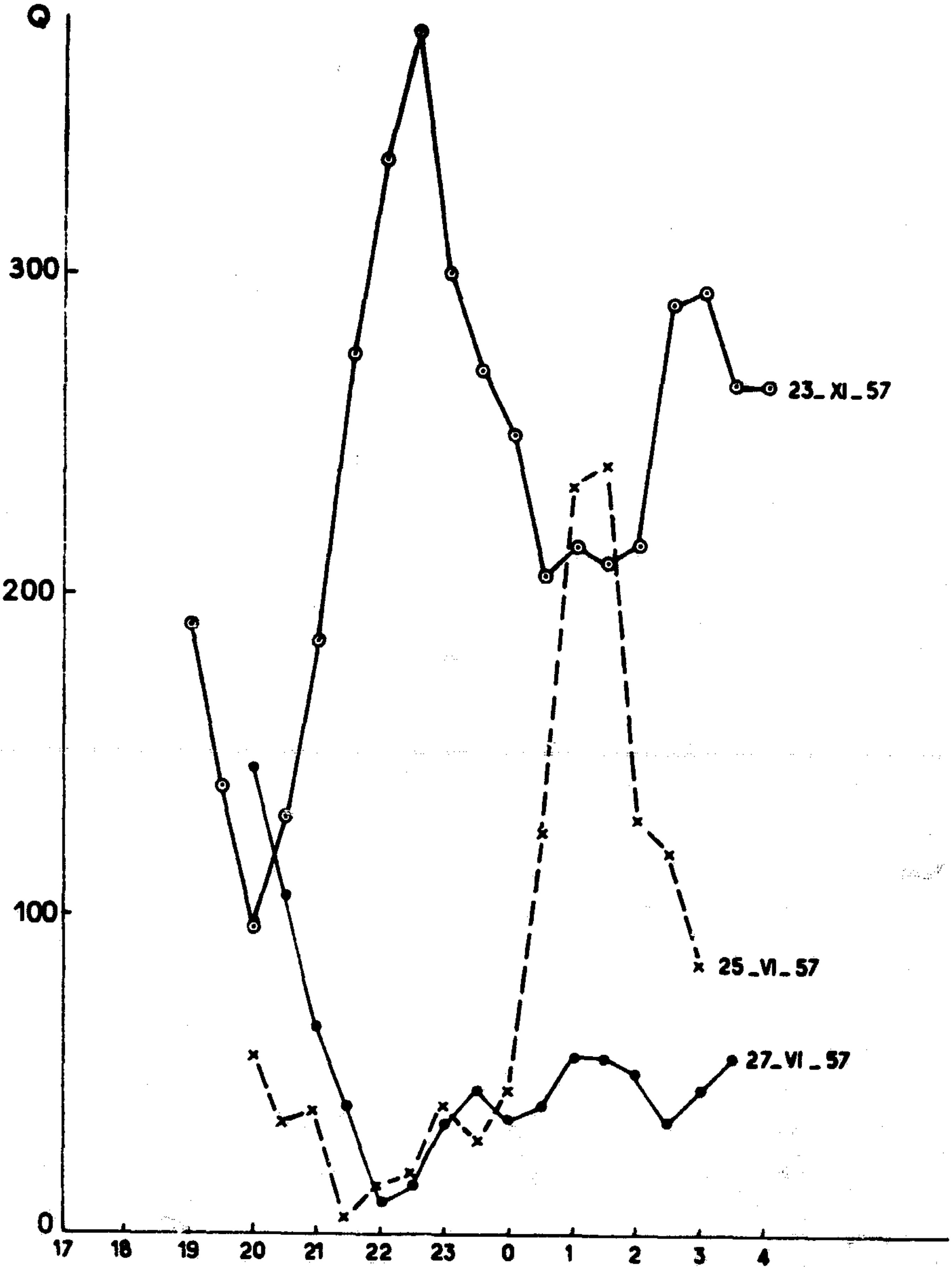

Figure 2.2 Barbier's observations of the predawn enhancement of OI(6300Å) (Barbier, 1959).

Cole (1965) remarks that there should be a post-twilight effect during the winter months since the conjugate point sunset occurs after local sunset. However this effect cannot be observed due to the more intense airglow being produced at this time by dissociative recombination.

The interval between sunset and the post-twilight effect and between the predawn enhancement and dawn depends on the difference in the sunset and sunrise times of the conjugate hemispheres and on the location of the observatory. This interval is greatest in winter and at midlatitudes. During the summer the conjugate point sunrise follows local sunrise and the conjugate point sunset precedes local sunset, and thus heating of the ionosphere due to conjugate effects is not observable during the summer.

Carlson (1966a, 1966b) has observed presunrise and postsunset ionospheric heating of the F region by Thomson-scatter radar, and finds that the onsets of these effects correlate well with magnetic conjugate-point sunrise times. At winter solstice this presunrise effect occured more than two hours before local sunrise. An ideal test of the theory presented by Cole would be a simultaneous measurement of the red line and of F-region temperature. The red-line intensity and temperature should increase in unison.

There appears to be no evidence for any significant amount of photoelectrons to exist locally during the nighttime in the absence of these conjugate effects. Chamberlain (1961) estimates that the contribution from higher-than-thermal energy electrons at the tail end of the Maxwellian distribution amounts to about 10^{-4} R. Therefore under normal nighttime conditions the effects of any excitation mechanisms other than dissociative recombination are assumed to be negligible. However, there are loss mechanisms of $O(^1D)$ which may compete with radiative transition, and this is the next topic of discussion.

2.4 Quenching of $O(^1D)$

2.4.1 Introduction

The $O(^1D)$ atom has a lifetime of about 110 seconds and will emit a 6300Å photon unless it is collisionally deactivated, or quenched. The term "quenching" seems more descriptive of the process since "collisional deactivation" suggests a physical process when, in fact, it may very well be a chemical one. The exact process for quenching of $O(^1D)$ has been somewhat elusive due to the difficulty of reproducing and observing atmospheric conditions in the laboratory. It is often difficult to distinguish between quenching by collisions with the walls and quenching by collisions with molecules. Also, $O(^1D)$ is a very reactive atomic species, and the emissions are difficult to observe under conditions which permit laboratory measurement of the reaction rate.

Quenching of an excited species can take place through a number of processes. There are two important general classifications into which these processes may be placed: physical quenching and chemical quenching. Both of these could be applicable to quenching of $O(^1D)$ and are described as follows:

(1) Physical quenching. The process of physical quenching involves the transfer of electronic energy into translational, electronic, vibrational, or rotational energy of the quenching particle through collisions, and does not involve any chemical change in the reactants. The electronic energy of X^* may be transferred into translational energy of the collision partners,

$$X^* + Y \rightarrow X + Y \qquad (2.10)$$

or energy transfer may occur through excitation of electronic or vibrational levels of the quenching particle:

$$X^* + Y \rightarrow X + Y^* \quad . \tag{2.11}$$

(2) Chemical quenching. Chemical quenching is characterized by a chemical change in the reactants. Quenching of X^* by a molecule YZ could be accompanied by dissociation of the quenching molecule where the products remain free,

$$X^* + YZ \rightarrow X + Y + Z \tag{2.12}$$

or where an association between the products takes place:

$$X^* + YZ \rightarrow XY + Z \tag{2.13}$$

There is also the possibility of an association taking place between the reactants to form a stable molecule,

$$X^* + Y \rightarrow XY \tag{2.14}$$

or an activated complex,

$$X^* + Y \rightarrow XY^* \tag{2.15}$$

where the activated complex XY^* is unstable and dissociates according to one of the following:

$$XY^* \rightarrow X + Y \tag{2.16}$$

$$XY^* \rightarrow X^* + Y \tag{2.17}$$

$$XY^* \rightarrow X + Y^* \tag{2.18}$$

To determine which of the previous processes is likely to be important, it is necessary to study the potential-energy surfaces for the interaction of the excited molecule and its quenching partner. If there is a crossing between any of these surfaces there is a good chance of an exact energy exchange taking place, and this is sometimes called a resonant reaction. However, if there is a separation between these surfaces, the probability of the reaction taking place is very small, depending on the size of the separation.

An important criterion by which many reactions are ruled out as quenching mechanisms is the Wigner spin-conservation rule (Laidler, 1950). When two particles interact, there may occur a so called resonance-splitting instead of a crossing of their potential-energy surfaces. When the surfaces are of the same multiplicity, the resonance separation is large (Figure 2.3). Therefore, the probability of a reaction taking place is very small. When the surfaces are of different multiplicity, resonance splitting is found to be very slight (Figure 2.4). In this case the system behaves as if the surfaces actually crossed and resists any change in spin angular momentum and hence multiplicity. This is called the Wigner spin-conservation rule.

Therefore, according to Wigner's rule, if the multiplicity of the reactants is the same as that of the products, then the reaction is favored. If they are different, the reaction is likely to be very slow. Some quenching mechanisms are presented below which have been considered by various workers on the basis outlined above.

2.4.2 Physical quenching

The two neutral molecules in the upper atmosphere which, because of their abundance, are most likely involved in quenching of $O(^1D)$ are N_2 and O_2. Bates and Dalgarno (1953) have suggested that the reaction

$$O(^1D) + O_2(X^3\Sigma_g^-)_{v''=o} \rightarrow O(^3P) + O_2(b^1\Sigma_g^+)_{v'\leq 2} \qquad (2.19)$$

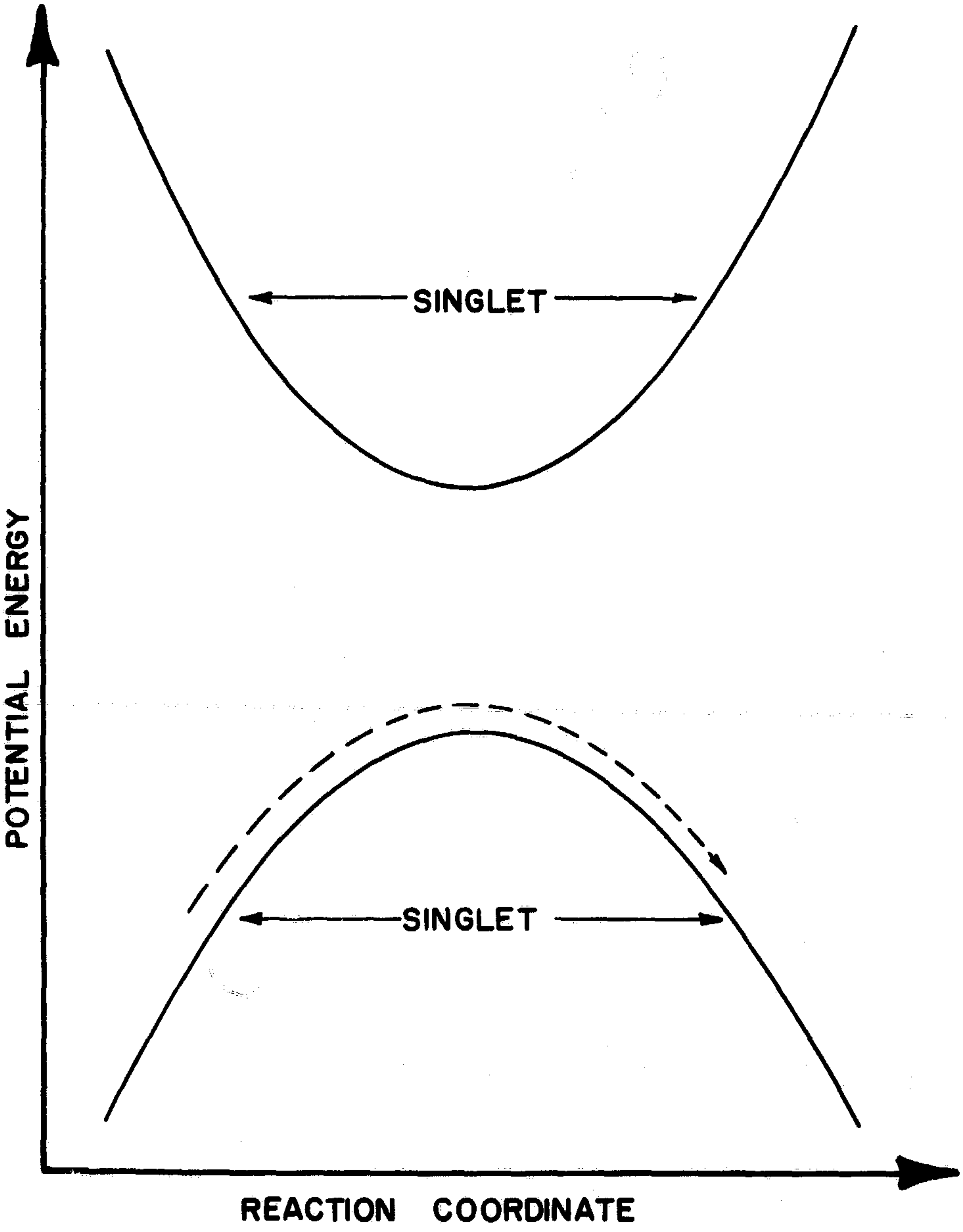

Figure 2.3 Potential-energy profiles for surfaces of the same multiplicity (Laidler, 1950).

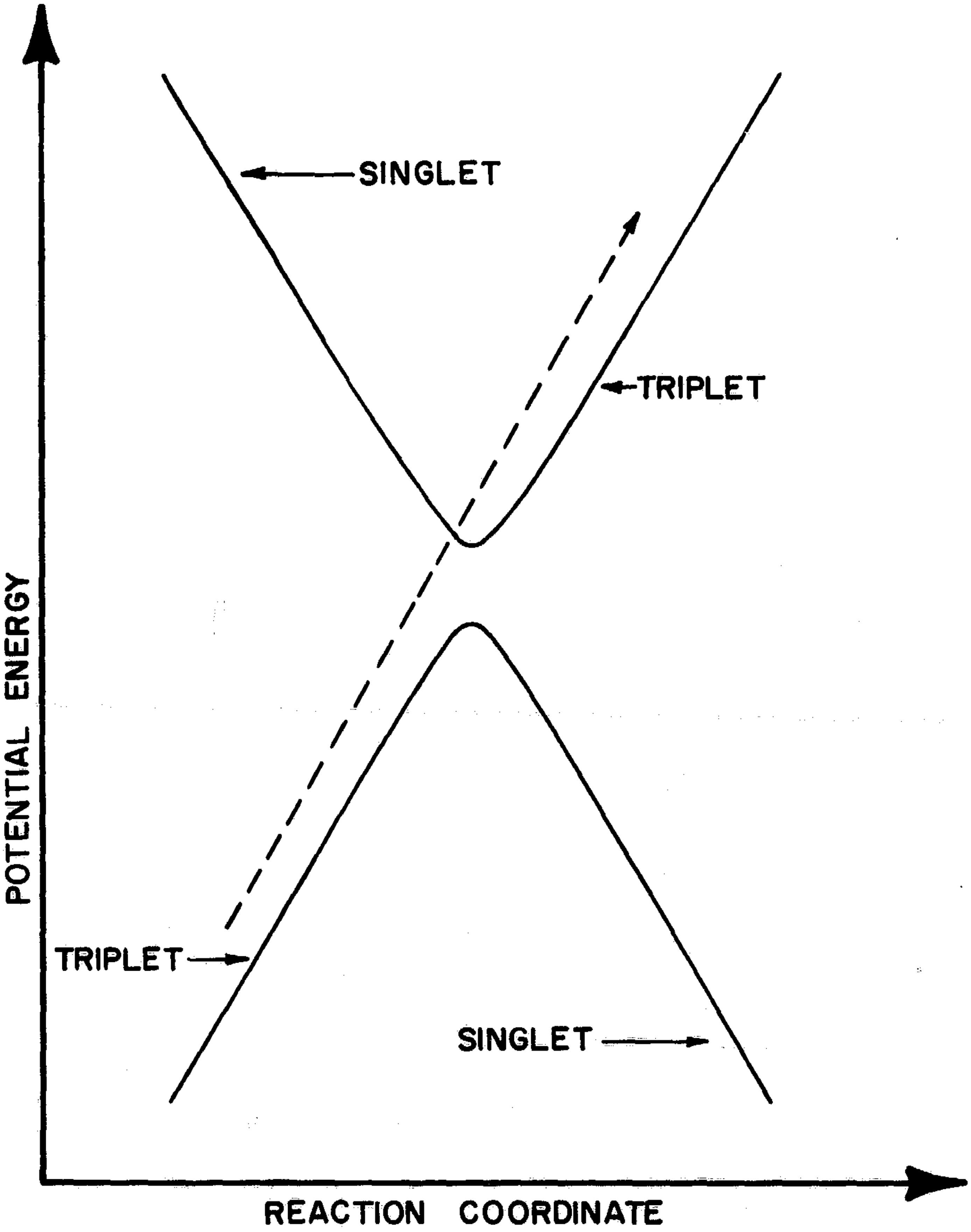

Figure 2.4 Potential-energy profiles for surfaces of different multiplicity (Laidler, 1950).

is efficient on the grounds that it is within .004 ev of resonance for v' = 2 and spin is conserved. This reaction is favored because the excitation energy of $O(^1D)$ is very close to an electronic or vibrational level of O_2. However, near resonance may not be enough in a reaction of this type (Chamberlain, 1961; Seaton, 1958). If resonance is very close, then the reverse of reaction (2.19) must also be considered. The important of this quenching process therefore depends on the probability that the $b^1\Sigma_g^+$ state of molecular oxygen will disappear by some other mechanism than the reverse of reaction (2.19). Chamberlain (1961) suggests radiative transitions to $X^3\Sigma_g^-$ and to $^1\Delta_g$, but adds that if these were the only routes of escape for $b^1\Sigma_g^+$, the resonance reaction (2.19) would not be important. Seaton (1958) proposed that the transition $b^1\Sigma_g^+ \rightarrow A^1\Delta_g$ may have a high probability, but there is no experimental evidence to validate his statement. The excited oxygen molecule may also be removed by electron transfer or atom-atom interchange reactions (Chamberlain, 1961).

On the basis of the foregoing argument a resonance reaction of $O(^1D)$ with N_2 has been considered unimportant because of the absence of any suitable electronic levels in N_2. A possible reaction would be (Demore and Raper, 1964)

$$O(^1D) + N_2(X^1\Sigma_g^+) \rightarrow O(^3P) + N_2(X^1\Sigma_g^+) \ , \qquad (2.20)$$

but this demands a 45.5 kcal net change of electronic energy and a change of spin. Hunten and McElroy (1966) point out the reaction

$$O(^1D) + N_2(^1\Sigma^+) \rightarrow O(^3P) + N_2^*(^1\Sigma^+)_{v''=7} \qquad (2.21)$$

in which the seventh vibrational level of N_2 is within .001 eV of exact resonance, but also note that spin is not conserved. Since no conclusive evidence for reactions (2.19), (2.20), and (2.21) really exists, and because the theoretical justification for the efficiency of these reactions is not fully convincing, there is still some doubt whether they are very efficient mechanisms for quenching of $O(^1D)$.

Although quenching of $O(^1D)$ by electrons is efficient (Hunten and McElroy, 1966), the electron concentration at night is usually no more than 10^6 cm^{-3}, which is small enough to make the effect of quenching by electrons negligible.

2.4.3 Chemical quenching

Demore and Raper (1962, 1964) and Snelling and Blair (1967) present convincing experimental and theoretical evidence that the reactions of $O(^1D)$ with N_2 and O_2 involve intermediate formation of N_2O^* and O_3^* respectively. Demore and Raper (1962) submit the following bimolecular reaction for quenching of $O(^1D)$ by N_2:

$$O(^1D) + N_2 \rightleftarrows N_2O^* \rightarrow N_2 + O(^3P) \qquad (2.22)$$

where N_2O^* is a vibrationally excited complex capable of predissociating to N_2 and $O(^3P)$. The efficiency of this process thus depends on the lifetime of N_2O^* with respect to redissociation to the original reactants and predissociation to N_2 and $O(^3P)$. It is interesting to note that predissociation to N_2 and $O(^3P)$ is a violation of the Wigner spin-conservation rule, but because of spin-orbit interaction there is a finite probability that the reaction will take place. Wigner's rule loses its applicability under these conditions, resulting in a sufficiently high reaction rate for (2.13) to be of importance.

The lifetime of N_2O^* is on the order of 10^{-11} sec, so at the very low pressures of the upper atmosphere it is not likely to be collisionally deactivated to a lower vibrational state before it proceeds in any direction by reaction (2.22). Since third-body stabilization is required in the formation of N_2O,

$$O(^1D) + N_2 + M \rightarrow N_2O + M \quad , \tag{2.23}$$

it is expected that formation of N_2O due to reaction (2.23) is very slow in the upper atmosphere. In addition, reaction (2.22) is about 75 times faster than reaction (2.23) due to a feature of the N_2O potential energy surfaces (Demore and Raper, 1962).

A similar mechanism for quenching by O_2 is as follows (Demore and Raper, 1964):

$$\begin{array}{c} O(^1D) + O_2(X^3\Sigma_g^-) \rightleftarrows O_3^* \text{ (triplet)} \rightarrow O(^3P) + O_2(b^1\Sigma_g^+) \\ \downarrow \\ O(^3P) + O_2(a^1\Delta_g) \end{array} \tag{2.24}$$

Since both predissociative reactions are exothermic and spin-allowed Demore and Raper argue that they would compete favorably with redissociation.

A closer look at the decomposition of N_2O^* can yield some indication of the temperature dependence of reaction (2.22). Figure (2.5) illustrates the potential energy diagram for N_2O, and reaction (2.22) written in more detail (Snelling and Blair, 1967) becomes

$$O(^1D) + N_2 \rightleftarrows {}^1NO^+ \rightleftarrows N_2O^* \rightarrow {}^3N_2O^+ \rightarrow N_2 + O(^3P) \tag{2.25}$$

The repulsive states $^3\Pi$ and $^3\Sigma$ are formed by the interaction of N_2 and $O(^3P)$,

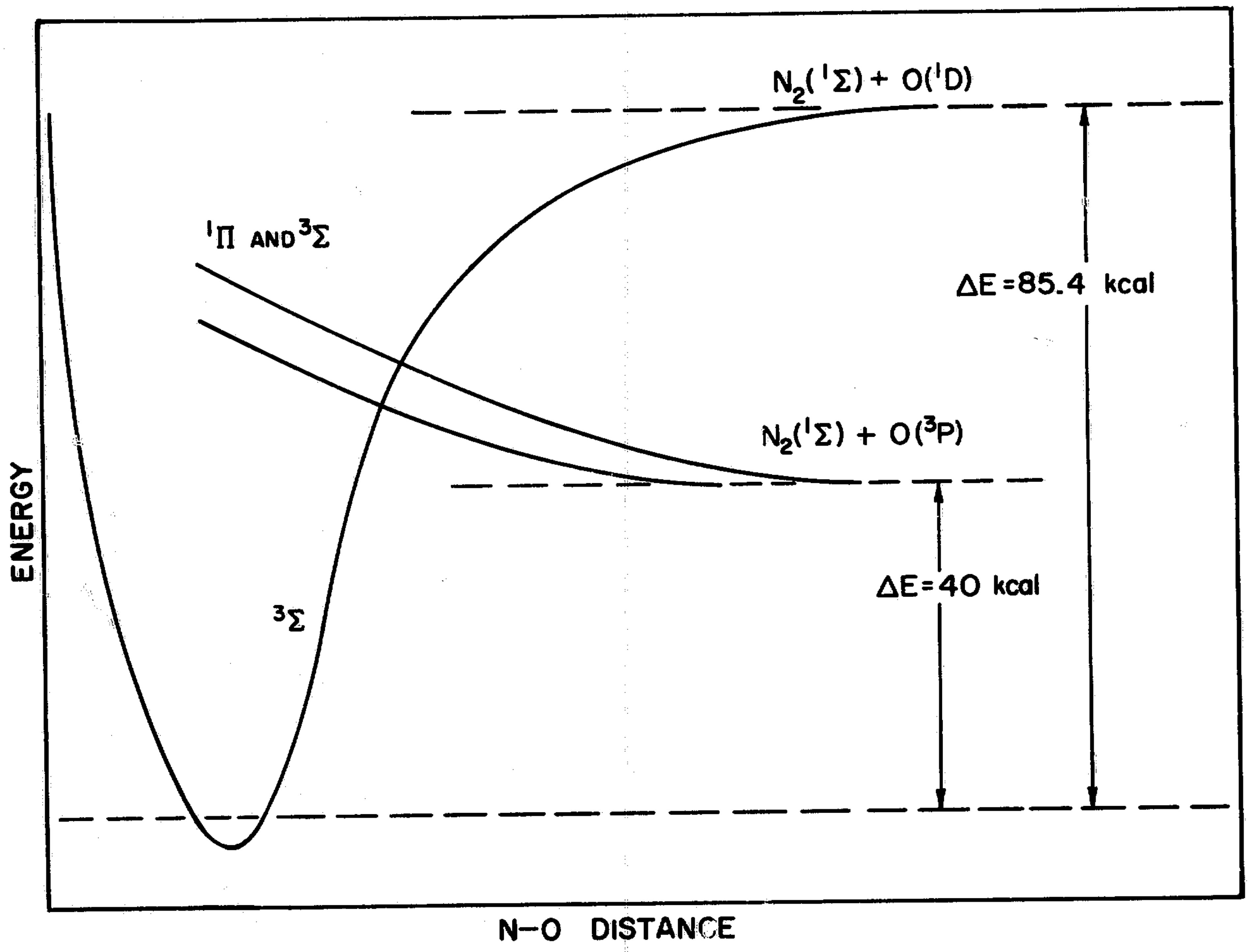

Figure 2.5 Potential-energy diagram for N_2O (Demore and Raper, 1962).

and are representative of the activated complex $^3N_2O^+$ in reaction (2.25) which then leads to products of triplet multiplicity. $^1N_2O^+$ is an activated complex which leads to products in the singlet state. The $^3\Pi$ and $^3\Sigma$ states cross (in the first approximation) the ground state of N_2O, and spin-orbit interaction results in a finite probability that a molecule in the $^1\Sigma$ state with sufficient energy will undergo a transition to the $^3\Pi$ or $^3\Sigma$ state and subsequent predissociation to N_2 and $O(^3P)$. The probability of predissociation is a function of the excess energy of N_2O^* above a critical energy which corresponds to the energy where the curves representing the states in Figure (2.5) cross. The energy of the molecule above the critical energy for predissociation is insensitive to temperature, whereas the excess energy of N_2O^* above the critical energy for redissociation is proportional to the thermal energy of the reactants (Demore and Raper, 1964). Therefore, a decreasing efficiency with increasing temperature is predicted for quenching of $O(^1D)$ by this mechanism.

2.5 Statement of the Problem

Demore and Raper estimate that the rate coefficient for quenching by N_2 is on the order of 10^{-11} - 10^{-10} cm^3/sec. Although no information is available on the potential energy surfaces of O_3^*, they have shown experimentally that the rate for quenching by O_2 is of the same order of magnitude as the rate for N_2. These results are in general agreement with most recent laboratory and aeronomical calculations (Young et al. 1968; Gulledge et al. 1968; Zipf, 1968; Peterson and Van Zandt, 1969; Noxon, 1968). However, there is as much as an order of magnitude difference in these results, indicating a need for further work in this area. In addition, the efficiency of the dissociative recombination of O_2^+ in producing $O(^1D)$ is poorly known, and must be determined with accuracy before airglow intensities can be calculated with confidence.

The basic problem at hand is to study the production and loss mechanisms of O(^{1}D) in the upper atmosphere during the nighttime. The determination of the following receives special attention in the following chapters:

(1) The rate coefficient for quenching of O(^{1}D).

(2) The efficiency of the dissociative recombination of O_2^+ in producing O(^{1}D).

(3) The temperature dependence of the above two quantities.

(4) The importance of quenching in studies of OI(6300Å).

The general procedure which will be followed is (1) Theoretical calculation of the red-line intensity (Chapter 3), (2) Experimental measurements of the red-line intensity (Chapters 4 and 5), and (3) Comparison of theoretical calculations and experimental observations to deduce certain parameters which define the efficiency of the production and loss mechanisms of O(^{1}D) (Chapters 6 and 7).

3. GROUND-BASED MEASUREMENTS OF OI(6300Å) INTENSITY

3.1 Characteristics of Zenith Measurements

All observations of the red-line intensity in this investigation are in the zenith direction. Thus the quantity observed by the photometer is an emission rate integrated over a vertical column of unit cross-sectional area. The rayleigh is an apparent emission rate of 10^6 photons cm^{-2} sec^{-1}. The rayleigh is a true emission rate only if the emission is isotropic and there are no radiative transfer effects between the source and the instrument. The justification for neglecting radiative transfer effects and a discussion of uncertainties of the experimental technique may be found in Chapter 4. The purpose of the present chapter is to analyze the ion chemistry of the nighttime F region, to derive an expression for the integrated emission rate in the vertical direction, and to compare this expression with a semi-empirical one derived by Barbier (1959).

3.2 Ion Chemistry of the F2 Layer

An expression will be derived in Section 3.3 which relates the integrated 6300Å emission rate to $[O_2]$, $[N_2]$, and [e]. To greatly simplify this derivation there are certain assumptions which can be made by considering the ion chemistry of the F2 layer. This is done below by solving the continuity equations for $O(^1D)$, NO^+, and O_2^+, and utilizing the results to derive an equation for the concentration of $O(^1D)$ at F region altitudes.

During the nighttime, F region molecular ions recombine with electrons:

$$O_2^+ + e \xrightarrow{\alpha_1} O + O \qquad (3.1)$$

$$NO^+ + e \xrightarrow{\alpha_2} N + O \qquad (3.2)$$

The rate coefficients for these reactions are $\alpha_1 = 10^{-7}$ cm^3 sec^{-1} at 700 K (Kasner and Biondi, 1968) and $\alpha_2 = 3 \times 10^{-7}$ cm^3 sec^{-1} at 400 K (Weller and Biondi, 1968). These rate coefficients decrease inversely with the first power of temperature.

O_2^+ is provided by the charge transfer mechanism

$$O^+ + O_2 \xrightarrow{\gamma_1} O_2^+ + O \tag{3.3}$$

and NO^+ by the ion-atom interchange reaction

$$O^+ + N_2 \xrightarrow{\gamma_2} NO^+ + N \quad . \tag{3.4}$$

The rate coefficients for reactions (3.3) and (3.4) are $\gamma_1 = 2.5 \times 10^{-11}$ cm^3/sec and $\gamma_2 = 2 \times 10^{-12}$ cm^3/sec at 1000 K (Warneck, 1967; Bohme <u>et</u> <u>al</u>. 1967). The measurements of Bohme <u>et</u> <u>al</u>. (1967) and Dunkin (1968) indicate a slightly increasing γ_1 with temperature; from about 1.3×10^{-11} cm^3 sec^{-1} at 600K to 3×10^{-11} cm^3 sec^{-1} at 1200K. Since $\gamma_1[O^+][O_2]$ and $\gamma_2[O^+][N_2]$ are much less than $\alpha_1\ [O_2^+][e]$ and $\alpha_2\ [NO^+][e]$, reactions (3.3) and (3.4) effectively determine the rate of recombination of O_2^+ and NO^+ and are thus a rate-limiting step in nighttime F-layer ion chemistry.

Consider now the continuity equation for a constituent X:

$$\frac{\partial[X]}{\partial t} = P_x - L_x - \text{div}\ ([X]\underline{v}_x) \tag{3.5}$$

where

$X \equiv O(^1D)$, NO^+, or O_2^+

P_x = rate of production of X

L_x = rate of loss of X

$\underline{v}_x$ = mean velocity vector of X

The divergence term represents the motions (drift and diffusion) of the constitutent X. Assuming vertical motions to be predominant, their effect is negligible if the mean vertical displacement Δh of a minor constituent during its mean lifetime τ is much less than its scale height H. Peterson et al. (1966) write this condition as follows:

$$\left|\frac{\Delta h}{H}\right| \approx \left|\frac{k\tau}{H[R]}\left(\frac{\partial \ln [M]}{\partial h} + \frac{1}{H}\right)\right| << 1 \tag{3.6}$$

where $k = 10^{19}\ \mathrm{cm}^6\ \mathrm{sec}^{-1}$

[M] = concentration of the minor unstable constituent

[R] = concentration of the rest of the atmosphere ,

and show that it holds for $O(^1D)$, O_2^+, and NO^+ up to a few scale heights above the peak of the $O(^1D)$ distribution. Since contributions to the integrated emission rate Q above these heights is negligible, the divergence term can be neglected. Equation (3.5) thus becomes

$$\frac{\partial [X]}{\partial t} = P_x - L_x \tag{3.7}$$

Peterson et al. show that the series solution for Equation (3.7) yields the following condition

$$\frac{\partial \ \ln P_x}{\partial t} << \frac{L_x}{[X]} \tag{3.8}$$

for time equilibrium of [X] to exist. They also demonstrate that condition (3.8) is met by $O(^1D)$, $O_2{}^+$, and NO^+ above 150 km. Accordingly, the rate of loss of these constituents equals their rate of production:

$$\alpha_1\ [e][O_2{}^+] = \gamma_1\ [O_2][O^+] \tag{3.9}$$

$$\alpha_2 \, [e][NO^+] = \gamma_2 \, [N_2][O^+] \tag{3.10}$$

$$(A_D + d_D)[O(^1D)] = P_D \tag{3.11}$$

Equations (3.9) and (3.10) follow directly from equations (3.1) - (3.4). Equation (3.11) is written by assuming that the only mechanisms involved in the loss of the $O(^1D)$ are quenching and radiative transition. The rate of loss (cm^{-3} sec^{-1}) is then equal to the product of the concentration (cm^{-3}) of $O(^1D)$ and the coefficient for depopulation (sec^{-1}). The quenching coefficient is d_D and A_D is the Einstein coefficient for the (^1D) state.

Since the atmosphere is electrically neutral,

$$[NO^+] + [O_2{}^+] + [O^+] = [e] \quad , \tag{3.12}$$

and imposing the additional condition

$$[O^+] >> [NO^+] + [O_2{}^+] \quad , \tag{3.13}$$

one can assume that $[O^+] = [e]$. This now gives

$$\alpha_1 \, [O_2{}^+] = \gamma_1 \, [O_2] \tag{3.14}$$

$$\alpha_2 \, [NO^+] = \gamma_2 \, [N_2] \tag{3.15}$$

The rates of the reactions for dissociative recombination of O_2^+ and NO^+ are $\alpha_1[O_2^+][e]$ and $\alpha_2[NO^+][e]$ respectively. The rate coefficients for dissociative recombination are α_1 and α_2, and [e] is the electron concentration. The rate of production of $O(^1D)$ is therefore given by

$$P_D = k_{D_1} \, \alpha_1 \, [O_2^+][e] + k_{D_2} \, \alpha_2 \, [NO^+][e] \tag{3.16}$$

where k_{D_1} = number of excitations of $O(^1D)$ per recombination of O_2^+

k_{D_2} = number of excitations of $O(^1D)$ per recombination of NO^+

The singlet state can also be produced by the emission of a 5577Å photon from $O(^1S)$, but since $O(^1S)$ arises significantly only from 3-body collisions (Chamberlain, 1961), the inclusion of this excitation process is not necessary in the F-region. However, some $O(^1D)$ will be formed by the $^1S \rightarrow {}^1D$ cascade following reaction (2.4). Any contributions due to this source are of course included in k_{D_1} as it is defined above.

Equating (3.11) and (3.16),

$$(A_D + d_D)[O(^1D)] = k_{D_1} \alpha_1 [O_2^+][e] + k_{D_2}\alpha_2[NO^+][e] \qquad (3.17)$$

an expression may now be written for $[O(^1D)]$:

$$[O(^1D)] = \frac{k_{D_1}\alpha_1[O_2^+][e]}{A_D + d_D} + \frac{k_{D_2}\alpha_2[NO^+][e]}{A_D + d_D} \qquad (3.18)$$

Substituting (3.14) and (3.15) into (3.18),

$$[O(^1D)] = \frac{k_{D_1}\gamma_1[O_2][e]}{A_D + d_D} + \frac{k_{D_2}\gamma_2[N_2][e]}{A_D + d_D} \quad . \qquad (3.19)$$

The quenching coefficient is defined as the product of the rate coefficient for quenching and the concentration of the quenching molecule. Using the notation of Peterson et al. (1966), the quenching coefficient is given by

$$d_D = S_D(O_2)[O_2] + S_D(N_2)[N_2] \qquad (3.20)$$

where $S_D(XY)$ = rate coefficient for quenching by XY

$[XY]$ = concentration of XY

Since $S_D(O_2) \leq S_D(N_2)$ (Young et al. 1968; Noxon, 1968) and $\frac{[N_2]}{[O2]} \approx 10$ between 200 km and 400 km (U.S. Standard Atmosphere Supplements, 1966), it is concluded that the predominant quenching agent of $O(^1D)$ in the upper atmosphere is N_2. The total contribution of $S_D(O_2)[O_2]$ to d_D is probably no more than 10%, and on this basis the quenching coefficient hereafter referred to will be defined as

$$d_D = S_D(N_2)[N_2] \qquad (3.21)$$

Thus the height distribution of $[O(^1D)]$ is now given in terms of k_{D_1}, $S_D(N_2)$, and other quantities which can be determined experimentally or from a model atmosphere. This result will now be utilized to find an expression for the integrated emission rate which can be compared with observations of the red line intensity to deduce K_{D_1} and $S_D(N_2)$.

3.3 Integrated 6300Å Volume Emission Rate

The rate of emission for a transition is given by the Einstein coefficient for that transition. Therefore, the 6300Å emission rate ε_D (photons cm^{-3} sec^{-1}) may be written as

$$\varepsilon_D(h) = .0069 \ [O(^1D)] \qquad (3.22)$$

where

$[O(^1D)]$ = concentration (cm^{-3}) of $O(^1D)$ at the height h(cm)

.0069 = Einstein coefficient (sec^{-1}) for the 6300Å emission.

The emission rate integrated in the vertical direction is

$$.0069 \int_0^\infty [O(^1D)] \, dh \text{ photons } cm^{-2} \ sec^{-1} , \qquad (3.23)$$

which is the experimentally measured quantity in airglow observations. Converting the units of this emission rate to a more convenient photometric unit, the rayleigh (1 rayleigh (R) = 10^6 photons cm^{-2} sec^{-1}), Q_D is now defined:

$$Q_D = .0069 \times 10^{-6} \int_0^\infty [O(^1D)]\, dh \text{ rayleighs.} \qquad (3.24)$$

Substituting (3.19) and (3.21) into (3.24), Q_D may be rewritten:

$$Q_D = \frac{.0069}{.0091} \times 10^{-6} \left[k_{D_1} \gamma_1 \int_0^\infty \frac{[O_2][e]}{1 + \frac{S_D(N_2)[N_2]}{.0091}}\, dh + k_{D_2} \gamma_2 \int_0^\infty \frac{[N_2][e]}{1 + \frac{S_D(N_2)[N_2]}{.0091}}\, dh \right] \qquad (3.25)$$

The k_D's and γ's may have a temperature dependence, but since the temperature profile is nearly isothermal for the F region during the night (U.S. Standard Atmosphere Supplements, 1966), these quantities have been brought outside the integral signs while writing Equation (3.25). The $[O_2]$ and $[N_2]$ can be calculated from a model atmosphere, [e] is obtained from ionograms taken simultaneously with the airglow measurements, and laboratory determined values can be used for γ_1 and γ_2.

Since $[O_2] \approx .1\ [N_2]$ between 200 km and 400 km (U. S. Standard Atmosphere Supplements, 1966) and $\gamma_2 \approx .1\ \gamma_1$ (Warneck, 1967; Bohme et al. 1967), the integrals in (3.25) become approximately equal, and thus the relative contribution to the airglow intensity of the dissociative recombination of NO^+ as opposed to the dissociative recombination of O_2^+ is given approximately by K_{D_2}/K_{D_1}. For the time being only contributions due to the dissociative recombination of O_2^+ will be considered, leaving

$$Q_D = 7.6 \times 10^{-7} k_{D_1} \gamma_1 \int_0^\infty \frac{[O_2][e]}{1 + 1.1 \times 10^2 S_D(N_2)[N_2]} \, dh \quad . \qquad (3.26)$$

This equation will now be compared with a semi-empirical one derived by Barbier (1959).

3.4 Barbier's Formula

The formula developed by Barbier (1959) relates the red line intensity to F-region ionospheric parameters:

$$Q_D = B(f_oF_2)^2 \exp[-(h'F - h_o)/H] + A \qquad (3.27)$$

where f_oF_2 = F layer critical frequency in MHz
$h'F$ = minimum virtual height of the F layer in km
H = scale height of O_2 in km
h_o = reference height in km

and A and B are empirical constants defined below.

The description "semi-empirical" often attached to this equation denotes that there did not seem to be a firm theoretical foundation for the equation at the time, although it did agree well with observations. The theoretical basis for this formula has since been analyzed in detail by Peterson (1968) with special attention to the various approximations made in its derivation.

The essentials of Barbier's derivation will be reproduced below, and comparisons will be made with formula (3.26) which is based on more fundamental considerations. Comments are also made on the validity and usefulness of Barbier's formula and are in agreement with those made by Peterson (1968).

Barbier proceeds as follows: Assuming the dominant processes are recombination of O_2^+,

$$O_2^+ + e \rightarrow O + O \tag{3.28}$$

and the charge transfer reaction

$$O^+ + O_2 \rightarrow O + O_2^+ \quad , \tag{3.29}$$

the number of recombinations per second integrated in a vertical column is

$$Q_D = K \int_0^\infty [O_2][e]\, dh \tag{3.30}$$

where K is a coefficient whose value is poorly known, but which can be evaluated within an order of magnitude from observations of the recombination rate of the F layer. (Note that Equation (3.30) is very similar to Equation (3.26) with the exception that the effect of quenching has been excluded.) Providing the width of the F2 layer is not too great, a mean value of $[O_2]$ in the F2 layer, designated by $<[O_2]>$, is assumed, yielding

$$Q_D = K<[O_2]> \int_0^\infty [e]\, dh \quad . \tag{3.31}$$

If $[O_2]_o$ is the value of $[O_2]$ at a reference height h_o, then

$$<[O_2]> = [O_2]_o \exp\, [- \frac{h_{max}-h_o}{H}] \tag{3.32}$$

assuming diffusive equilibrium of O_2 and a constant scale height H. The height of the F2 layer peak is h_{max}. Now since the maximum electron density of the F2 layer is proportional to $(f_oF2)^2$, the total electron content in a vertical column is proportional to $(f_oF2)^2$:

$$\int_0^\infty [e]dh = \alpha(f_oF2)^2 \tag{3.33}$$

This assumes that the electron density at all heights decreases at the same rate. An F layer following this behavior is said to be "shape preserving" because the height of the maximum electron density (h_{max}) remains constant, and although the total electron content is decreasing, the shape of the electron density profile remains the same. This approximation is good providing there are no abrupt changes of electron density at any height. Shape preserving behavior is generally a good assumption at low to midlatitudes, providing of course that the atmosphere is not in a disturbed state. More will be said about this shape preserving behavior in Section 5.3.

Under the assumption of a shape-preserving layer, the height of the peak electron density differs from the virtual height of the bottom of the F2 layer by a constant:

$$h_{max} = h'f + \Delta h \quad ; \tag{3.34}$$

inserting (3.32), (3.33), and (3.34) into (3.31) one obtains

$$Q_D = B(f_oF2)^2 \exp - [(h'f - h_o)/H] \tag{3.35}$$

The additive constant A in Equation (3.27) represents contributions from sources other than dissociative recombination of O_2^+, and is small compared to the first term. This completes Barbier's derivation.

The F2 layer critical frequency f_oF2 and minimum virtual height h'f can be read directly from ionograms, h_o is arbitrary, and H is determined from the exospheric temperature. Methods of calculating exospheric temperatures will be presented in Section 5.3. The constant B remains and is expressed as follows:

$$B = \alpha K[O_2]_o \exp[- \frac{\Delta h}{H}] \qquad (3.36)$$

Barbier's assumption of (3.30) has been justified by considering the ion chemistry of the F region in Sections 3.2 and 3.3. Equation (3.26) establishes the validity of Barbier's assumption. Neglecting quenching for the moment ($S_D(N_2) = 0$), a comparison of Equations (3.30) and (3.26) yields an expression for K:

$$K = .76 \times 10^{-6} K_{D_1} \gamma_1 \qquad (3.37)$$

and thus

$$B = .76 \times 10^{-6} K_{D_1} \gamma_1 \alpha [O_2]_o \exp[- \frac{\Delta h}{H}] \qquad (3.38)$$

The rate coefficient γ_1 has been determined in the laboratory, $[O_2]_o$ can be taken from a model atmosphere, and K_{D_1}, α, and $\Delta h/H$ can be calculated from experimental data. A comparison will be made between observed airglow intensities and those calculated from Barbier's formula in Chapter 7.

It is important to note that Barbier's formula neglects the effect of quenching which results in serious error for a low layer of emission. However, the formula enables a quick estimate of airglow intensity when other ionospheric data is available. Although it is not as accurate as equation (3.26), because of the additional approximations which enter its derivation, it can be used to separate contributions of the red line due to dissociative recombination of O_2^+ from other means of excitation such as particle impact providing this is the dominant contribution. Thus it has possible uses in the study of the predawn enhancement or auroras. Application of this formula to large amounts of world wide ionospheric data can give the variation of red line intensity with season, geographic location, and solar and geomagnetic activity.

A discussion of the experimental method used to measure airglow intensities and ionospheric parameters will now be presented to aid in the data analysis and evaluation of the results.

4. EXPERIMENTAL

4.1 Purpose of the Experimental Program

It is the purpose of the experimental program to provide some of the unknown quantities in equation (3.26), namely Q_D and [e]. Calculation of $[O_2]$ and $[N_2]$ from a model atmosphere is discussed in Chapter 5 along with the determination of [e]. A laboratory-determined value of γ_1 is used, leaving only K_{D_1} and $S_D(N_2)$ unknown. Calculation of these latter quantities is a primary objective of this analysis and a detailed discussion is found in Chapters 6 and 7. The present chapter deals primarily with experimental technique, calibrations, corrections, and other pertinent experimental information. The experimental data and associated calculations are presented in Chapter 5.

4.2 Description of Instrument

The airglow measurements were taken with the airglow photometer designed by Purdy et al. (1961) and built by Fish (Fish and Bowhill, 1968). The photometer is designed to observe the night sky through 4 filters which are moved over the photometer in sequence with a turret mechanism. When a filter stops over the photometer a standard light reference reading, a sky reading, and a dark reading are taken. This is accomplished by another turret mechanism positioned over the first. Thus there is a full rotation of the top turret for every quarter rotation of the bottom turret. Since each reading lasts ten seconds, and 15 seconds is reserved to record each reading, the total time for one cycle is 5 minutes.

The light entering the instrument is focused on a photomultiplier tube which then gives off pulses of current. The number of pulses present and their amplitude is a strong function of the voltage applied to the photomultiplier tube. These pulses are then amplified by a nuvistor preamplifier circuit in the photometer. The pulses from the nuvistor preamplifier go into a linear amplifier with adjustable (20-1200) voltage gain. The output of the linear amplifier then goes to a pulse height discriminator which puts out a 10 volt .15 microsecond wide pulse for every input pulse which has an amplitude greater than a threshold value. The threshold can be set from .3 to 10 volts by a ten-turn helipot. The pulses from the discriminator then go to a counter and are recorded digitally on paper tape.

4.3 Linearity of the Data-taking System

For each filter three separate readings are taken in sequence: a standard-light reference reading, a sky reading, and a dark reading. The dark reading provides an indication of the noise in the system and is subtracted from the other two readings. In addition, the line intensity is calculated in Section 4.5 by subtracting the continuum intensity from the observed combination of continuum and line intensities. A basic assumption underlying this method of correction is that the system is linear. That is, that the reading obtained from the sum of two sources is indeed the same as the sum of the readings of the two sources taken separately. Therefore, the range of linearity of the data taking system had to be determined.

It is apparent that there are settings of the photomultiplier tube voltage, the linear amplifier gain, and the pulse height discriminator which may cause the system to behave in a non-linear fashion. The settings must be such that the pulses leaving the discriminator (maximum rate = 500 KHz) does not exceed the maximum counting rate of the counter (300 KHz) and thus cause erroneous counts. Also, the rate of pulses entering the discriminator at amplitudes greater than the threshold may exceed the amount it can accept.

This is the so-called pulse pile-up problem. The discriminator may not be triggered for every input pulse thereby preventing the proper number of output pulses from reaching the counter. This discrepancy will occur if the time between any two successive pulses entering the discriminator greater than its threshold value is less than the reset time of the discriminator (2×10^{-6} sec). Assuming the pulses from the photomultiplier approximate a Poisson distribution (Gadsden, 1964, 1965) the effective pulse rate N' reaching the counter is related to the original pulse rate N by

$$N' = \frac{N}{1 + Nt} \qquad (4.1)$$

where t is the reset time of the discriminator. The highest rate of incoming pulses is about 5×10^3 sec^{-1}, which does not produce any significant effect on the pulse rate reaching the counter.

Another possible source of non-linearity is the photomultiplier tube. It was decided that the possibility of contributions to non-linearity from this and other sources warranted determination of the linearity of the data-taking system as a whole. The following experiment was therefore performed to find a useful range of settings with optimum linearity.

Two small incandescent lights powered by regulated voltage supplies were placed in the field of view of the photometer. If the system is linear, the counter reading for the intensity of the lights together should equal the sum of the readings of the two lights taken separately. This experiment was performed for a range of amplifier and discriminator settings, the photomultiplier tube voltage being kept constant at 1100 volts.

The experimentally determined quantity chosen to represent the linearity of the system is the ratio of the sum of the two separate readings to the reading when the two lights are both on. This ratio, R, is plotted versus discriminator settings in Figure 4.1 for several values of linear amplifier gain. An exactly linear system is given by R = 1. For the settings represented here, the best linearity is given by gain setting (CG) = $\frac{1}{4}$ and discriminator settings (D) between 035 and 055.

The range of discriminator settings for any gain setting is determined by the maximum counting rate of the counter and the minimum number of pulses which are needed for statistical accuracy. Since the pulses from the photomultiplier approximate a Poisson distribution (Gadsden, 1965), the standard deviation of the number of pulses in any reading is equal to the square root of the number of pulses. The standard deviation increases as the number of pulses decreases, so it is necessary to keep the number of pulses entering the counter as large as possible. It is also desirable to keep the standard light count on the same order of magnitude as the sky count, so for this reason the discriminator setting for CG = $\frac{1}{4}$ is kept below 065, which allows a count rate of at least 7.5×10^2 sec^{-1}. For CG = $\frac{1}{4}$ and D = 030, the pulses enter the counter at 9.5×10^3 sec^{-1}. Since the counter can accept no more than 10^4 sec^{-1} for a ten second sampling before it overflows, this combination of settings allows nearly the maximum permissible number of pulses to reach the counter. The small deviation from linearity for these settings is probably due to pulse pile-up.

It should be mentioned that the intensities of the lights remain constant, and their values do have some significance. The total intensity of the two lights passing through the 37.2Å wide filter is the same as the intensity

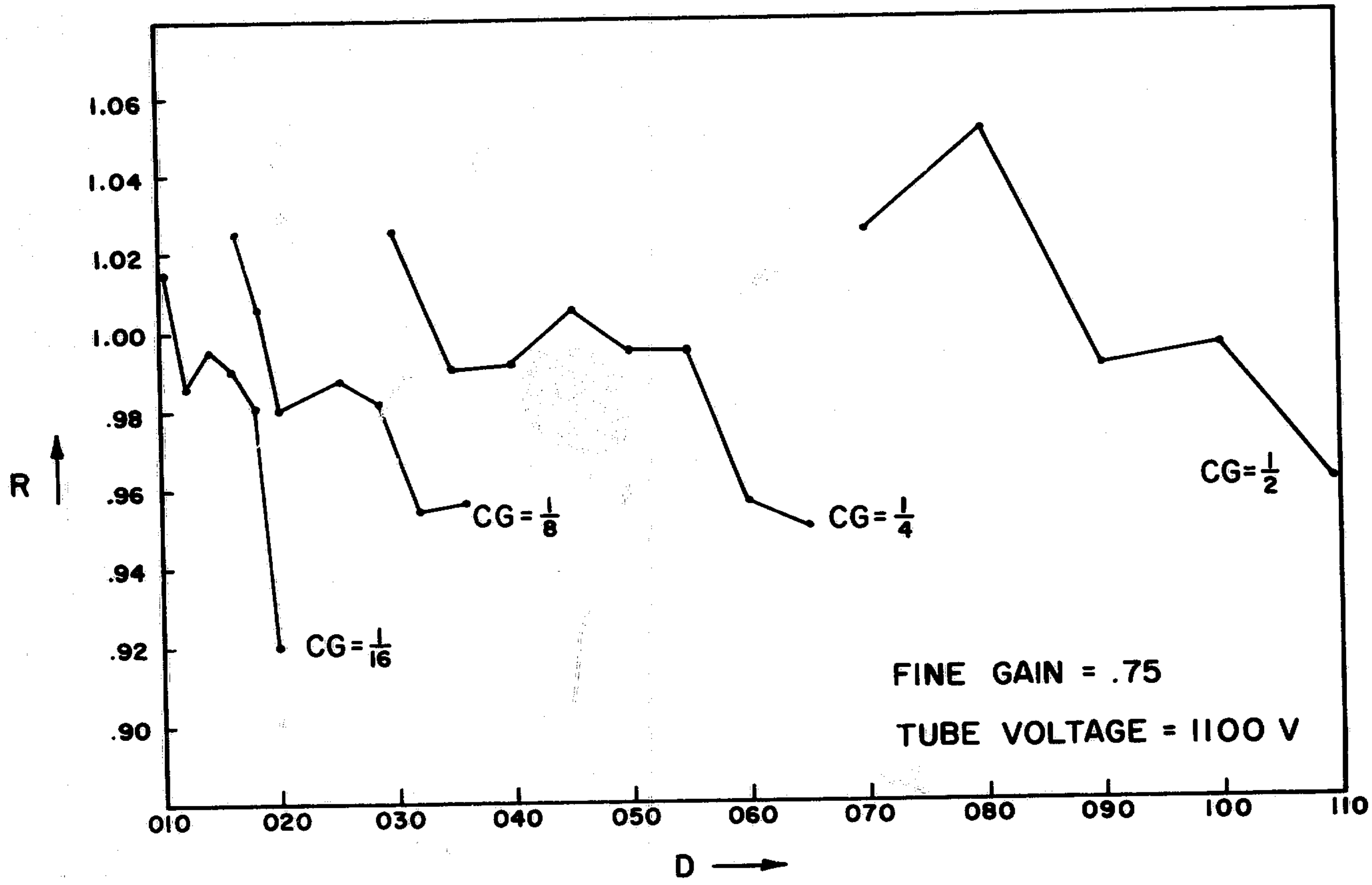

Figure 4.1 Linearity (R) of the data-taking system vs. discriminator setting (D) for coarse gain (CG) = $\frac{1}{16}$, $\frac{1}{8}$, $\frac{1}{4}$, $\frac{1}{2}$.

of the standard light source transmitted by the same filter. The counter reading for this intensity is about 5 x 10^4 for D = 040 and CG = $\frac{1}{4}$. The standard count for the broad red (BR) filter is plotted against the ratio R for several values of CG (Figure 4.2). From this graph it is possible to outline an operating procedure to obtain optimum linearity for this range of settings: After sunset adjust the CG to $\frac{1}{16}$ and the D to 016. The counter reading for the standard light passing through the BR filter should be approximately 6 x 10^3. This will allow a maximum reading of airglow intensity of 200 rayleighs. When the sky reading lowers to 6 x 10^3, change the CG to $\frac{1}{4}$ and the D to about 040. The standard count should now be near 5 x 10^4. This setting may be used throughout the night provided the airglow intensity does not exceed 70 rayleighs. At sunrise it will be necessary to return the settings to their sunset positions.

4.4 Calibrations

4.4.1 Standard light source

The standard light source is a carbon-14 activated phosphor which emits a light of known intensity from 3800Å to 6660Å. It was last calibrated in June, 1969, at Kitt Peak National Observatory. The calibration data appears in Table I. The radiance of the phosphor varies somewhat with time (Kulkarni and Sanders, 1964; Blacker and Gadsden, 1966, 1967) and must be calibrated every six months. Also, since the radiance of the phosphor decreases about five percent per degree centigrade in the range 4000-7000Å, temperature control to within a few degrees centigrade is maintained in the compartment which houses the photometer.

4.4.2 Interference filters

Since the characteristics of the interference filters may vary with time

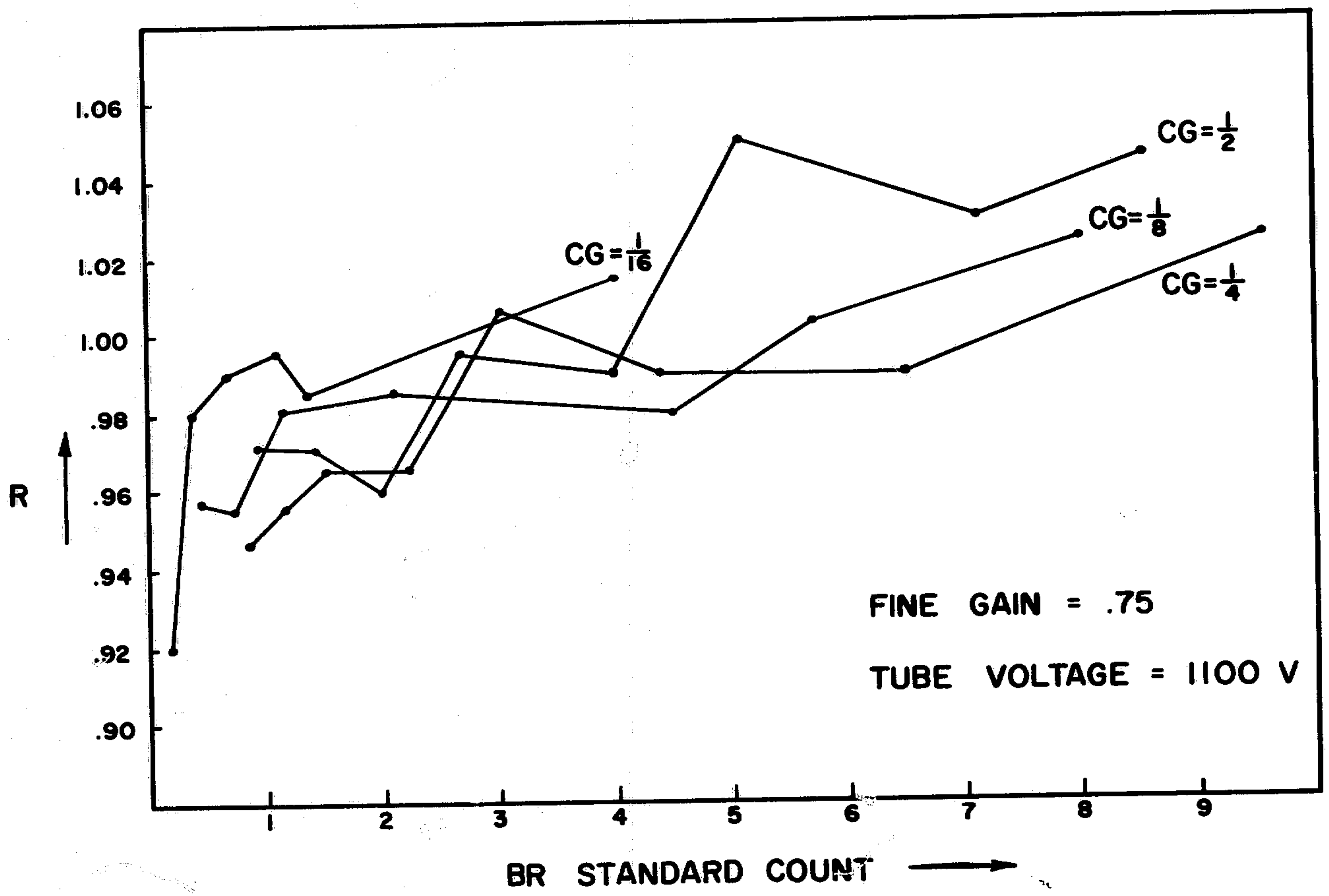

Figure 4.2 Linearity (R) of the data-taking system vs. broad red (BR) standard count for coarse gain (CG) = $\frac{1}{16}, \frac{1}{8}, \frac{1}{4}, \frac{1}{2}$.

TABLE I

C^{14} Brightness Calibration

C^{14} 7.5 MC
Material USRC - 51093
10-63
vs Kitt Peak LBS #1
June 10, 1969

Wavelength Å	Brightness R/Å
3800	.053
3900	.183
4000	.731
4100	2.15
4200	4.10
4330	6.65
4400	7.11
4500	6.66
4660	4.96
5000	2.84
5200	2.73
5330	2.27
5577	2.08
5660	2.28
5893	3.78
6000	4.71
6300	7.39
6330	6.93
6364	7.55
6660	6.50

(Blacker and Gadsden, 1967), it is advisable to calibrate the filters every six months. The 6300Å filters were last calibrated in September, 1969. The measurements were made with a Cary Model 14 spectrophotometer, and the results are given in Figure 4.3, illustrating the variation of the center transmittance with wavelength. The transmission of each filter at each wavelength was found by taking a reading at the center of the filter, and several peripheral to the center, and averaging the transmissions. The area under the transmittance versus wavelength curve was then calculated to determine the equivalent widths of the filters. The equivalent width is defined as the area under the transmittance vs. wavelength curve.

The angle of incidence and variation of temperature also affect the performance of interference filters (Blifford, 1966). Variations occur in the center wavelength, bandwidth, and percentage transmittance. Consequently, temperature control to within a few degrees centigrade and accurate orientation of the filters are required in order to ensure desired accuracy.

4.5 Corrections

4.5.1 Contamination from other light sources

The 6300Å emission line is separated from the night sky spectrum (Figure 2.1) by a narrow band (equivalent width = 11.5Å) interference filter. In order to remove contamination from other light sources (airglow continuum, zodiacal light, integrated starlight, and scattered light from Champaign, 8 km away), contributions due to these sources as determined by observation through a 37.2Å wide filter (also centered on 6300Å) are subtracted in the data analysis.

One source of contamination in particular that should be mentioned is the OH(9-3) band with band head near 6256Å. This has been a troublesome

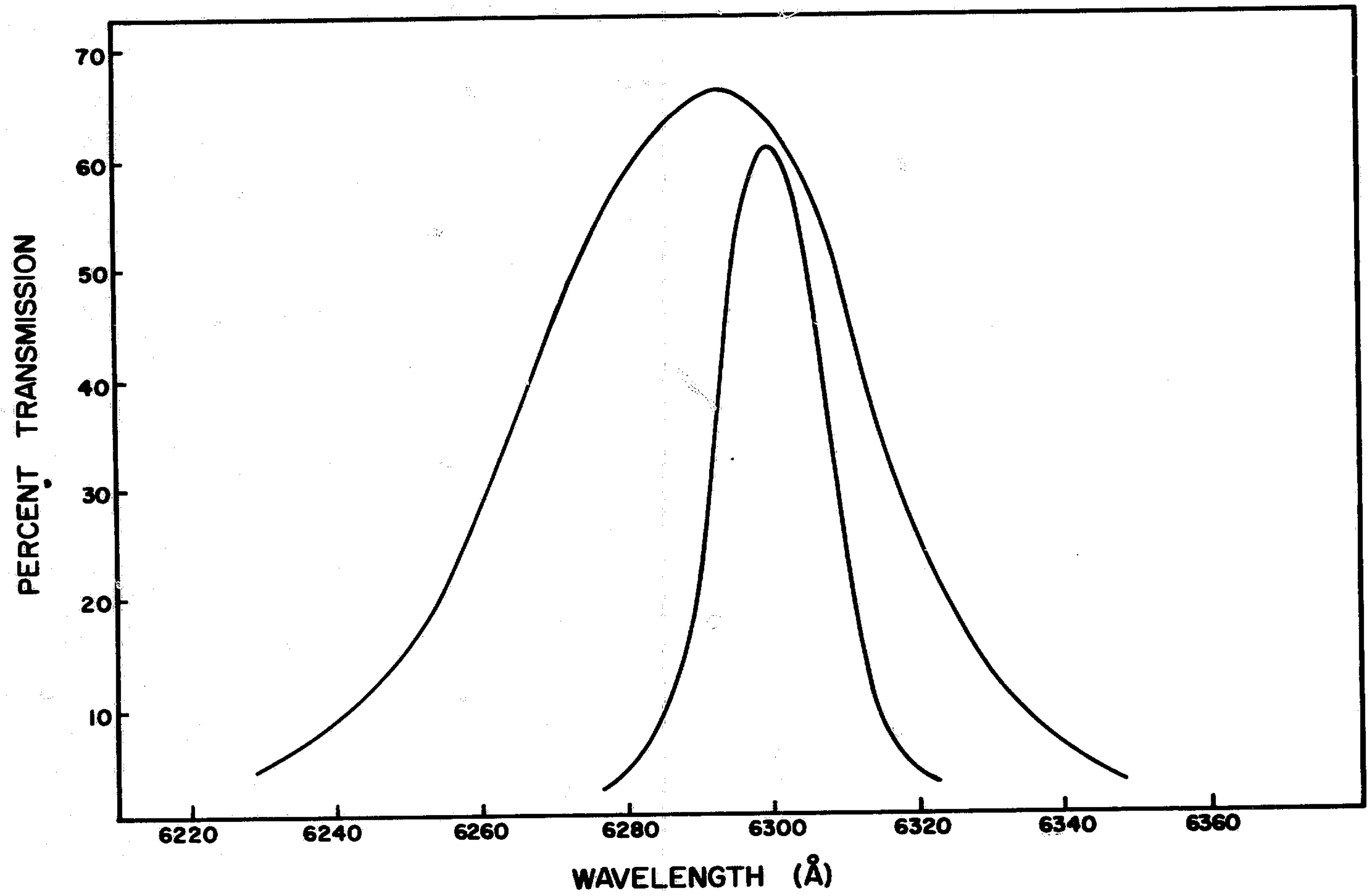

Figure 4.3 Center transmissions for broad and narrow 6300Å interference filters.

contaminant in all studies of the 6300Å line and necessitates, in our method of correction at least, that the width of the filters not be too large.

The sky emission I_{SKY} transmitted by a filter is equal to the sum of the background and line intensities transmitted:

$$I_{SKY} = I_c W + I_e T \tag{4.2}$$

where I_c = background intensity in R/Å

W = equivalent width of the filter in Å

I_e = line intensity in R

T = transmission of the filter at the emission line wavelength,

and providing the background emission is constant over the width of the filter. The emission from the standard source I_{ST} transmitted by the filter is given by

$$I_{ST} = WQ \quad . \tag{4.3}$$

The quantity Q is the spectral radiance of the standard source in R/Å and is assumed to be constant over the width of the filter. Since the data taking system was shown to be linear, the sky and standard intensities, I_{SKY} and I_{ST}, are in the same ratio as their respective counts, C_{SKY} and C_{ST}:

$$\frac{I_{SKY}}{I_{ST}} = \frac{C_{SKY}}{C_{ST}} \tag{4.4}$$

C_{SKY} and C_{ST} are the values after contributions due to noise have been subtracted. Combination of (4.2), (4.3) and (4.4) for both the narrow and broad filters yields the line intensity I_e and background intensity I_c:

$$I_e = W_1 W_2 Q \frac{\frac{C_{SKY2}}{C_{ST2}} - \frac{C_{SKY1}}{C_{ST1}}}{W_1 T_2 - W_2 T_1} \tag{4.5}$$

$$I_c = Q \frac{C_{SKY1}}{C_{ST1}} - I_e \frac{T_1}{W_1} \tag{4.6}$$

$$I_c = Q \frac{C_{SKY2}}{C_{ST2}} - I_e \frac{T_2}{W_2} \tag{4.7}$$

The subscripts 1 and 2 refer to the narrow and broad filters respectively.

Equations (4.6) and (4.7) can be used as a check on the ratio of the filter widths, W_1/W_2. From the spectrophotometer calibration, this ratio is measured to be 3.23. Calculation of this quantity from airglow data yields values of 3.35 ± .15, and thus provides an indication of calibration error.

4.5.2 Effect of extinction by the atmosphere

Light entering the photometer has traversed troposphere, and the effects of extinction (scattering and absorption) must be considered before drawing any conclusions based on observed airglow intensities. Radiation from the emitting layer is absorbed by ozone and water vapor and is scattered by molecules, water droplets, dust, and aerosols. Not only must the loss of radiation be considered, but also scattering of light into the line of sight from an essentially infinite (and curved) layer is of importance. These two effects tend to cancel one another, and it is believed that the total effect is small in the zenith direction (Chamberlain, 1961). Therefore extinction by the atmosphere will be neglected.

2 of 2

4.5.3 Transmission of outside glass

The sky emissions pass through a glass-covered hole in the top of the photometer housing. Therefore, the standard light had to be corrected to outside the instrument. Care was taken to insure that the photometer received light from the same field of view for both positions of the standard light. To prevent variations due to temperature of the spectral radiance of the standard light source, the experiment was performed when the temperature outside the photometer housing was the same as that inside. The combined transmission of the two parallel glass plates was found to be .91. This should remain a constant correction provided the glass is kept clean.

5. EXPERIMENTAL DATA

5.1 Introduction

The purpose of this chapter is to present experimental data and to illustrate the methods of data reduction which were used in the analysis. The final aim of the experimental program is to provide airglow intensities and electron density profiles. These measurements will then be utilized in Chapter 6 to deduce values for K_{D_1} and $S_D(N_2)$.

The ionosonde and airglow equipment are both on the same field site (geographic lat. 40° 10' 03" N, long. 88° 09' 32" W) in Urbana, Illinois. Ionograms were always taken at 15 minute intervals and airglow intensities were usually taken every 5 or 10 minutes. All airglow intensities were measured in the zenith direction. The data used in the calculations is only from clear nights during the lunar last quarter through lunar first quarter when interference from moonlight was at a minimum.

The data used in the analysis is from 4 nights in July, 12 nights in August, and 4 nights in September, 1969. During some nights complete observations were obtained when on others only portions of the night could be studied because of clouds, haze, and difficulties with the instruments. Also, other data had to be disregarded due to such difficulties as mispunching of the digital tape, spread F on the ionograms, and interruptions in the ionosonde operation.

5.2 Airglow Intensities

OI(6300Å) measurements for nights when a major portion of the intensity variation was observed are presented in Figures 5.1 to 5.10. Some of the red line intensity variations which were observed followed a monotonic decrease throughout the night (Figures 5.1-5.4) much like the type I behavior described

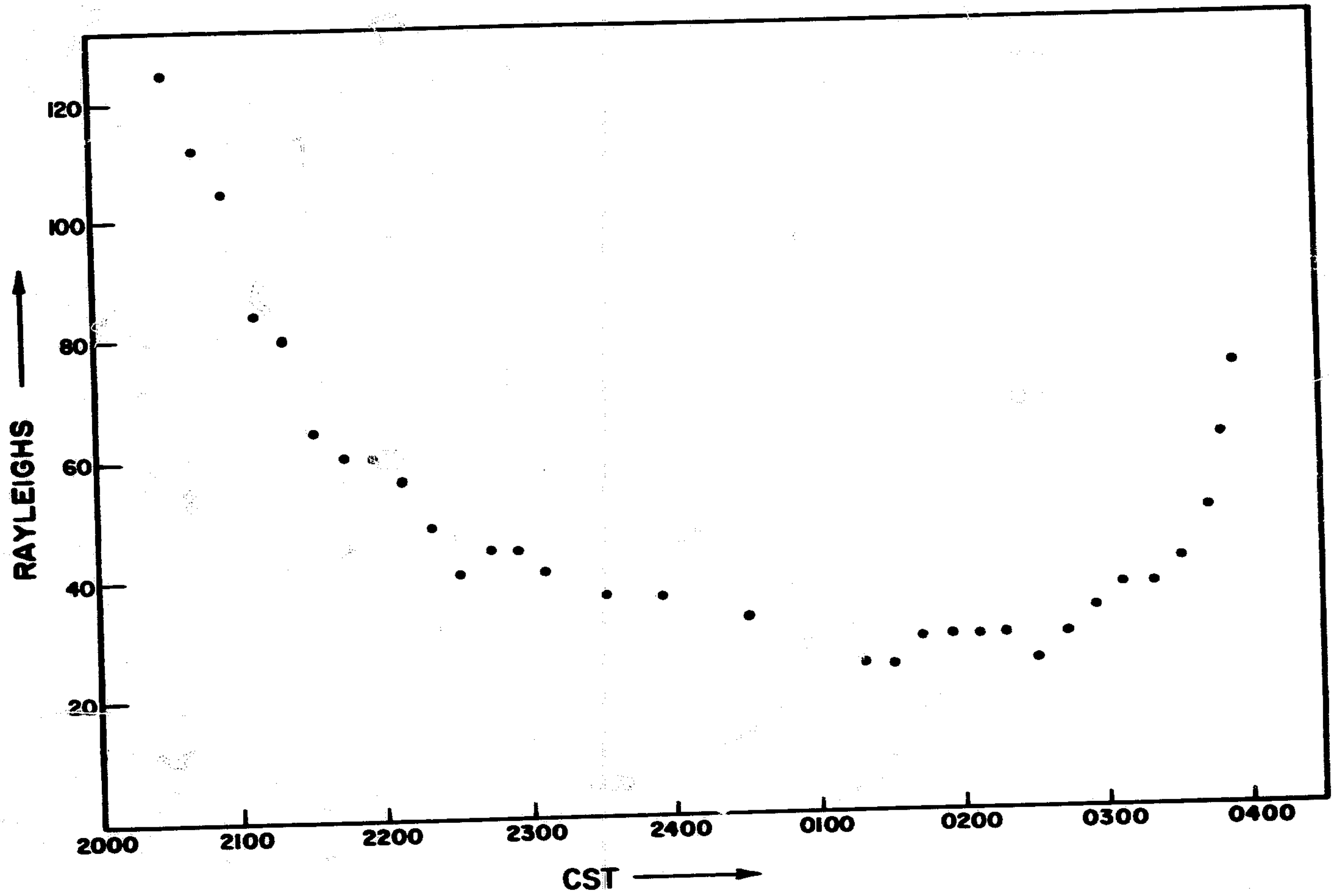

Figure 5.1 OI(6300Å) zenith intensities on the night of August 6/7, 1969.

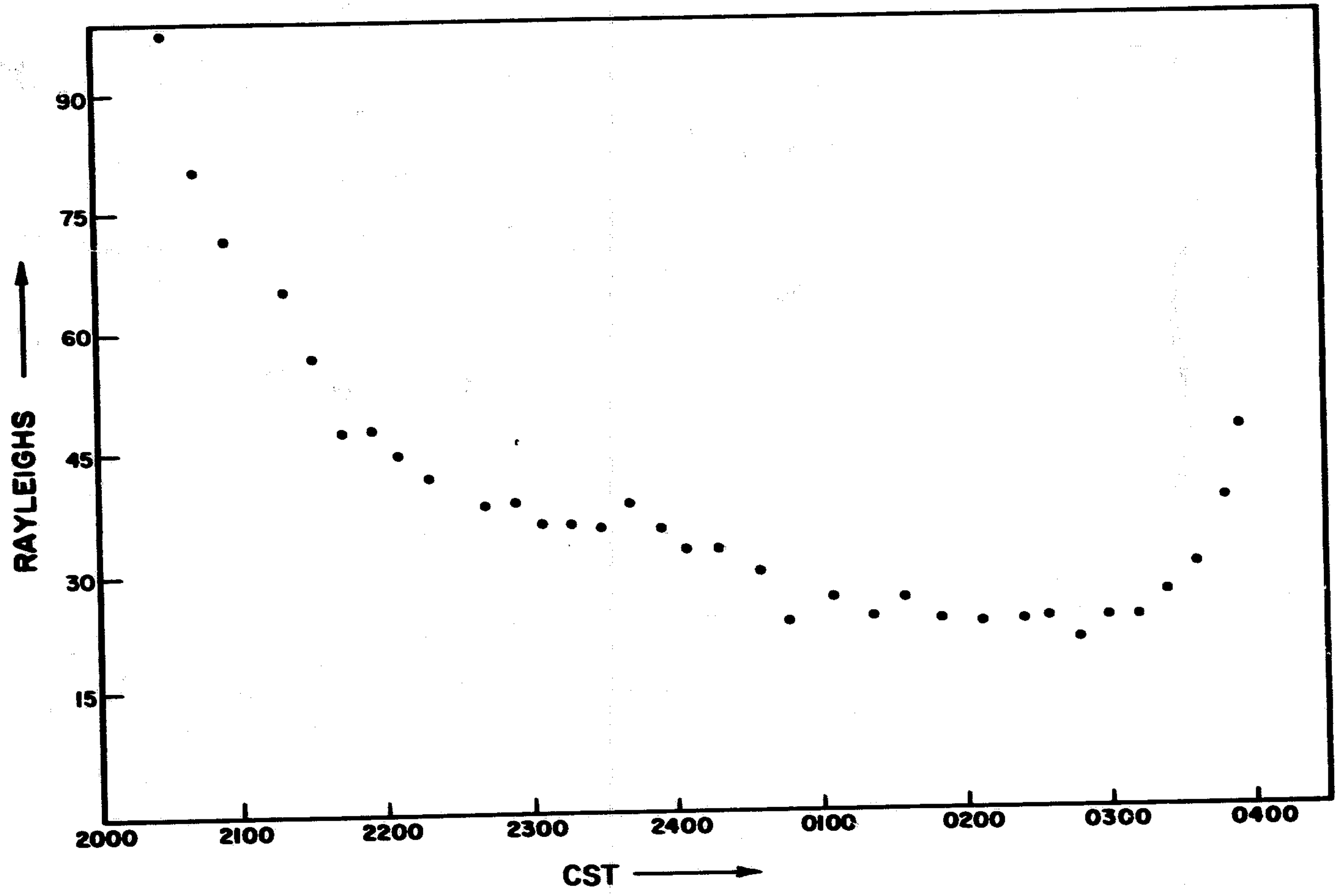

Figure 5.2 OI(6300Å) zenith intensities on the night of August 10/11, 1969.

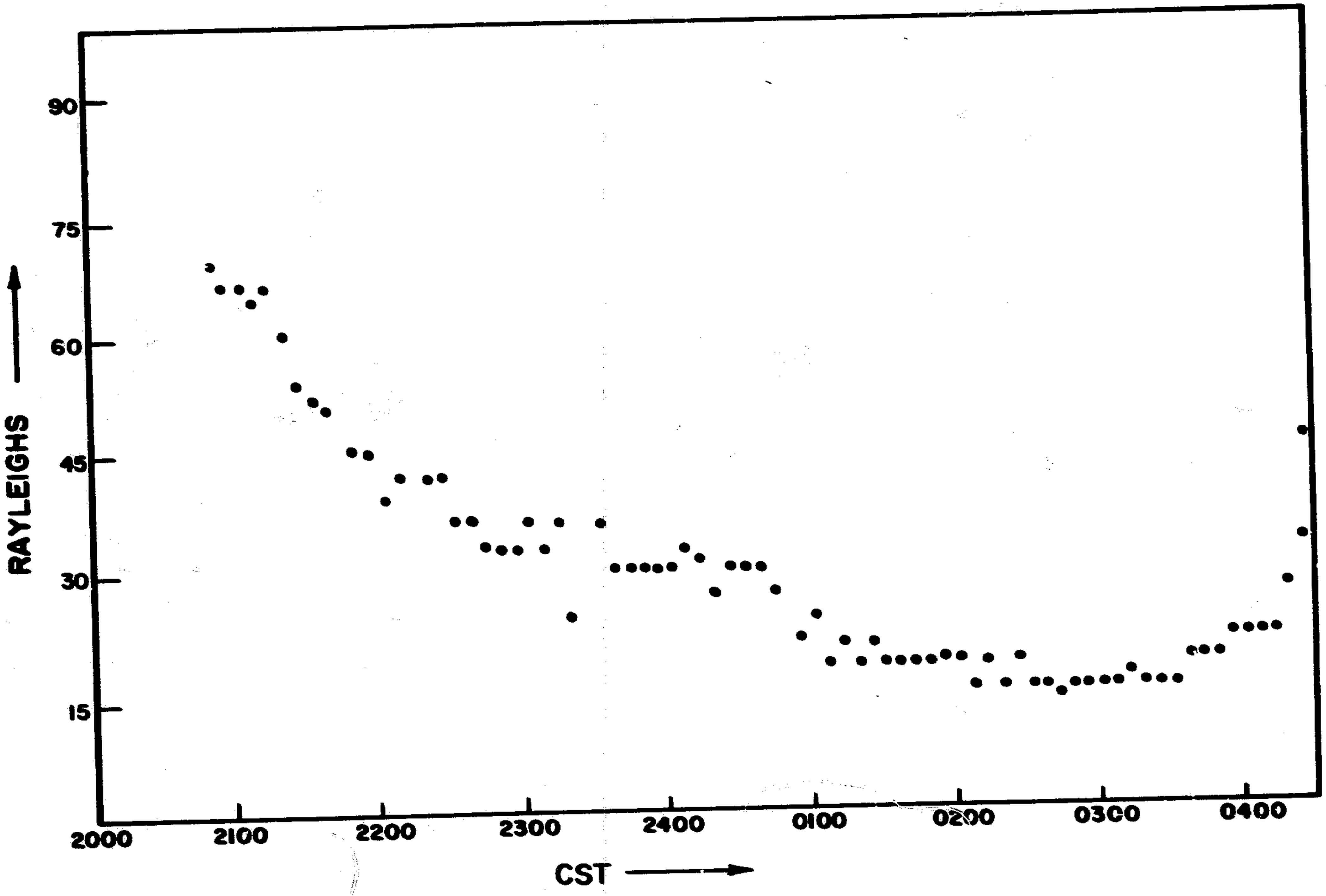

Figure 5.3 OI(6300Å) zenith intensities on the night of September 8/9, 1969.

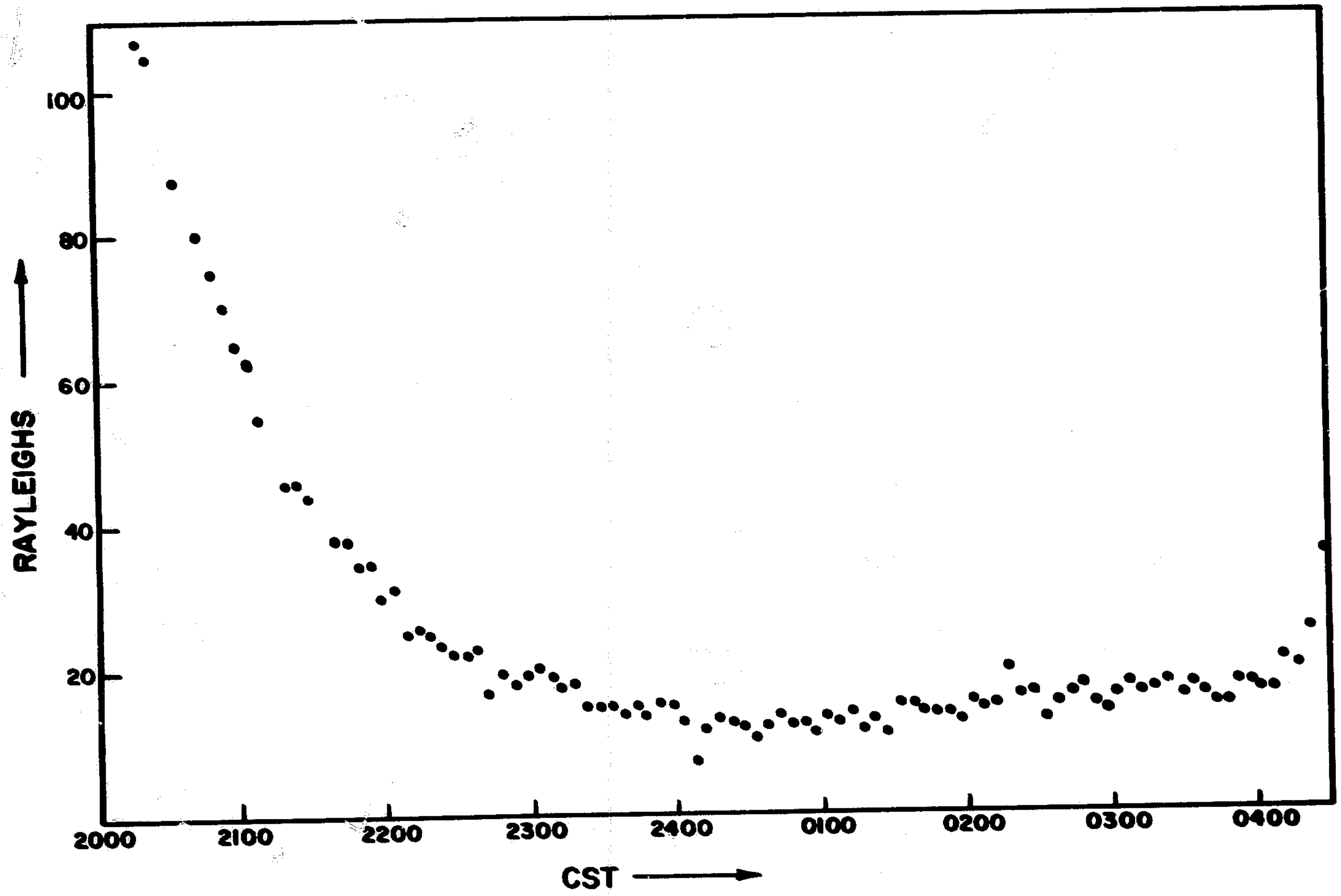

Figure 5.4 OI(6300Å) zenith intensities on the night of September 12/13, 1969.

by Bellew and Silverman (see Section 1.4). On other nights (Figures 5.5-5.10) variations similar to type III behavior were observed. Red line intensities generally reached a minimum of about 15R-30R on all nights.

5.3 Electron Density Profiles

5.3.1 Reduction of ionograms

The bottomside electron density profiles are determined from ionograms taken by a Model J5W Magnetic AB sweep-frequency ionosonde. The ionograms show the variations of virtual height of reflection as a function of the radio frequency. To obtain the actual height of reflection the virtual height must be corrected for the velocity of propagation of the radio wave in the ionosphere.

For the case of radio waves of frequency f vertically incident on the ionosphere the virtual height h'(f) is given by

$$h'(f) = \int_0^{h_o} \mu'(N,f)\, dh \qquad (5.1)$$

where h = height above the ground in km.
h_o = actual height of reflection in km.
$\mu'(n,f)$ = group refractive index
$N(h)$ = electron density at height h
f = radio frequency in MHz.

When the effects of collisions and the earth's magnetic field are taken into account, it is not in general possible to solve this integral analytically and numerical techniques must be employed.

The method used to reduce the ionograms is due to Doupnik and Schmerling (1965) and involves fitting the electron density profile with a set of parabolic laminations, which is a more accurate and convenient method than that

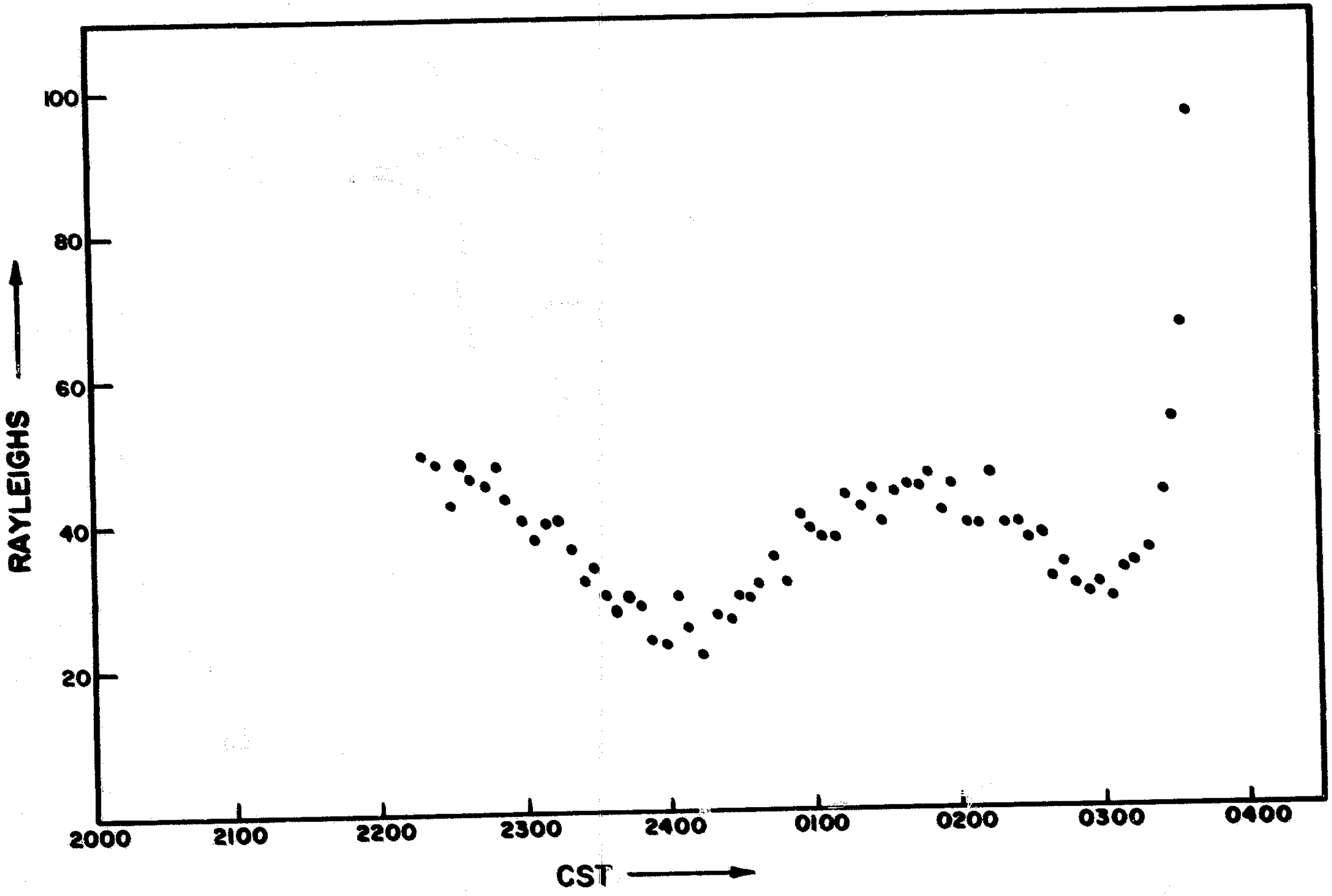

Figure 5.5 OI(6300Å) zenith intensities on the night of July 16/17, 1969.

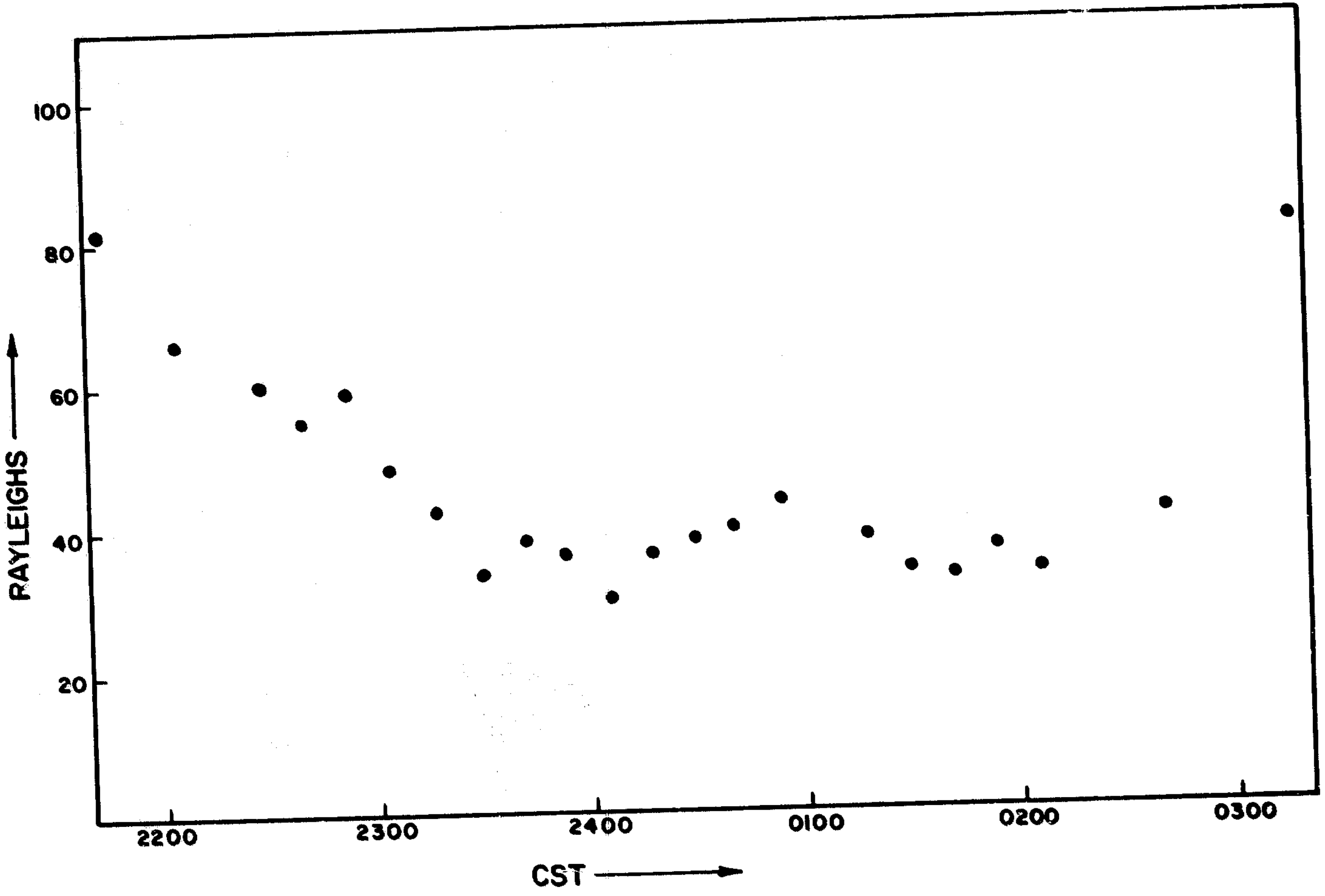

Figure 5.6 OI(6300Å) zenith intensities on the night of July 1/2, 1969.

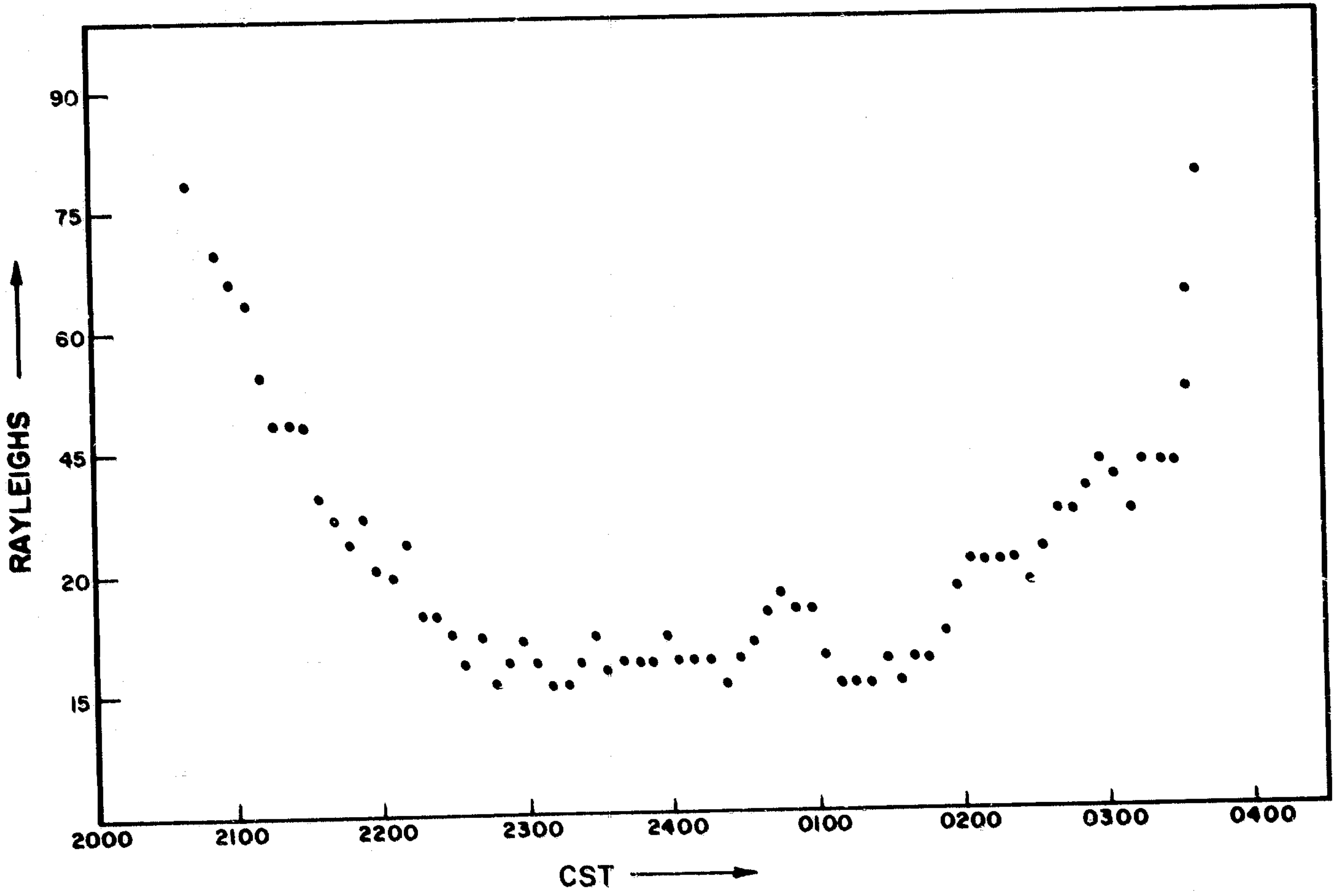

Figure 5.7 OI(6300Å) zenith intensities on the night of July 24/25, 1969.

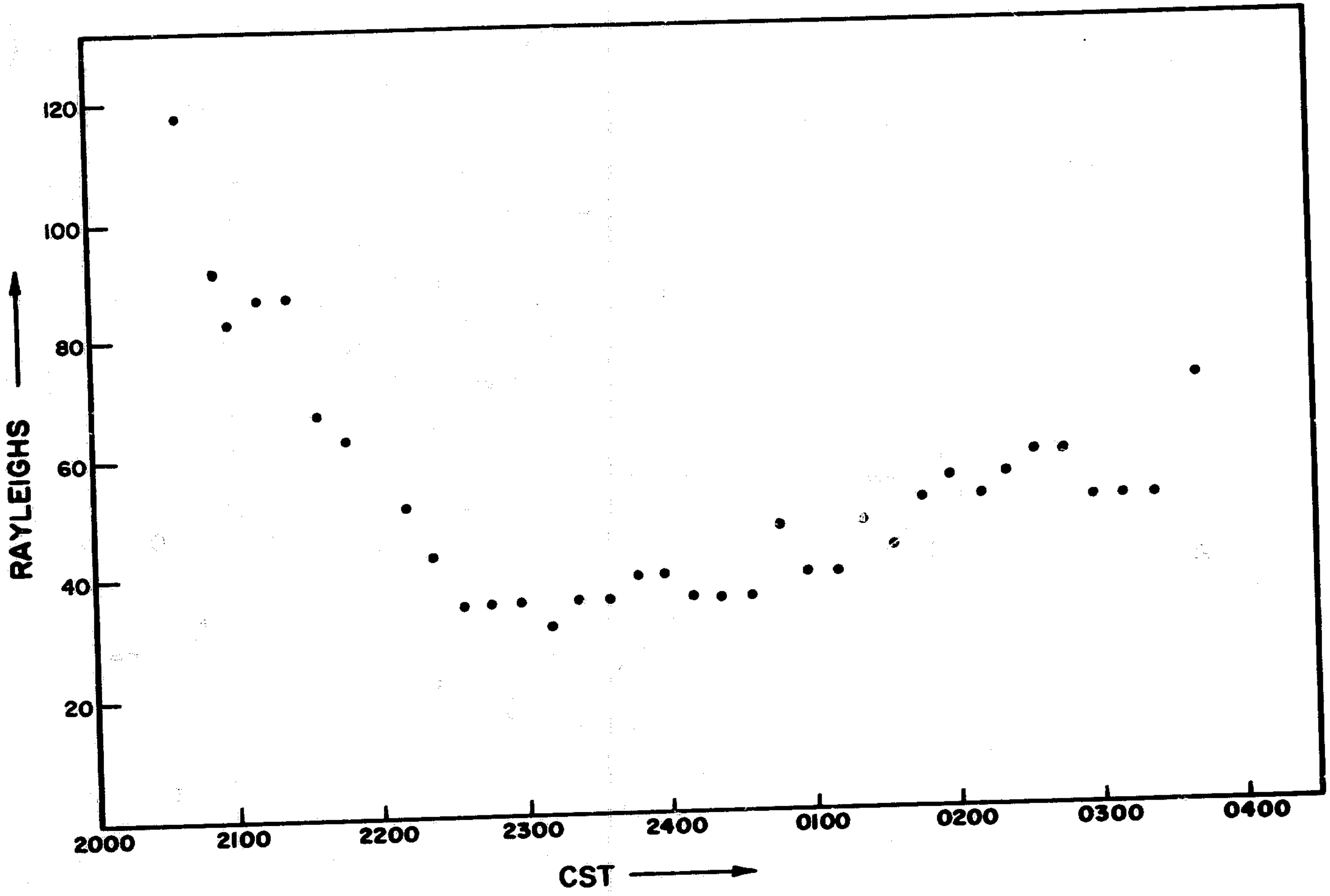

Figure 5.8 OI(6300Å) zenith intensities on the night of August 5/6, 1969.

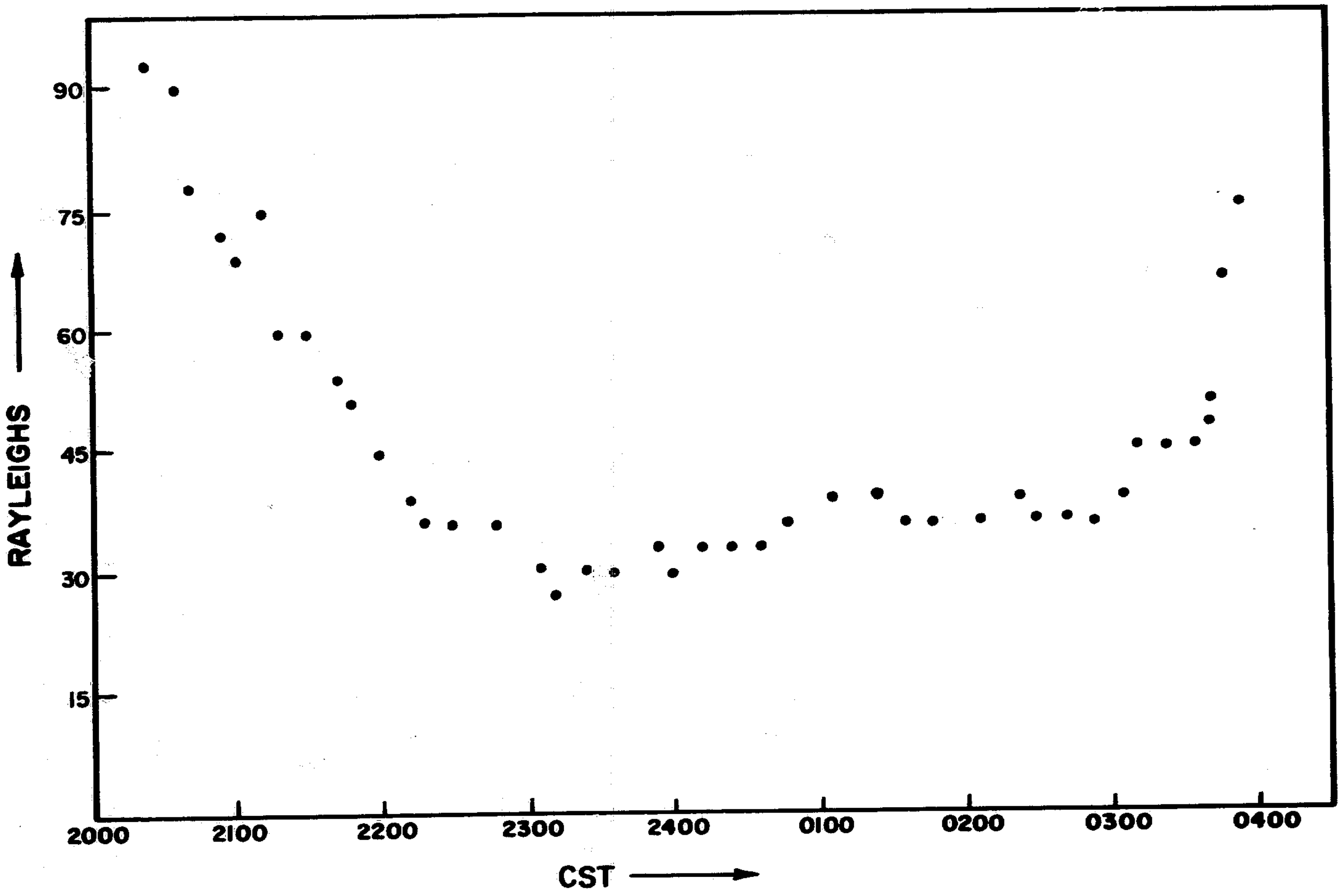

Figure 5.9 OI(6300Å) zenith intensities on the night of August 9/10, 1969.

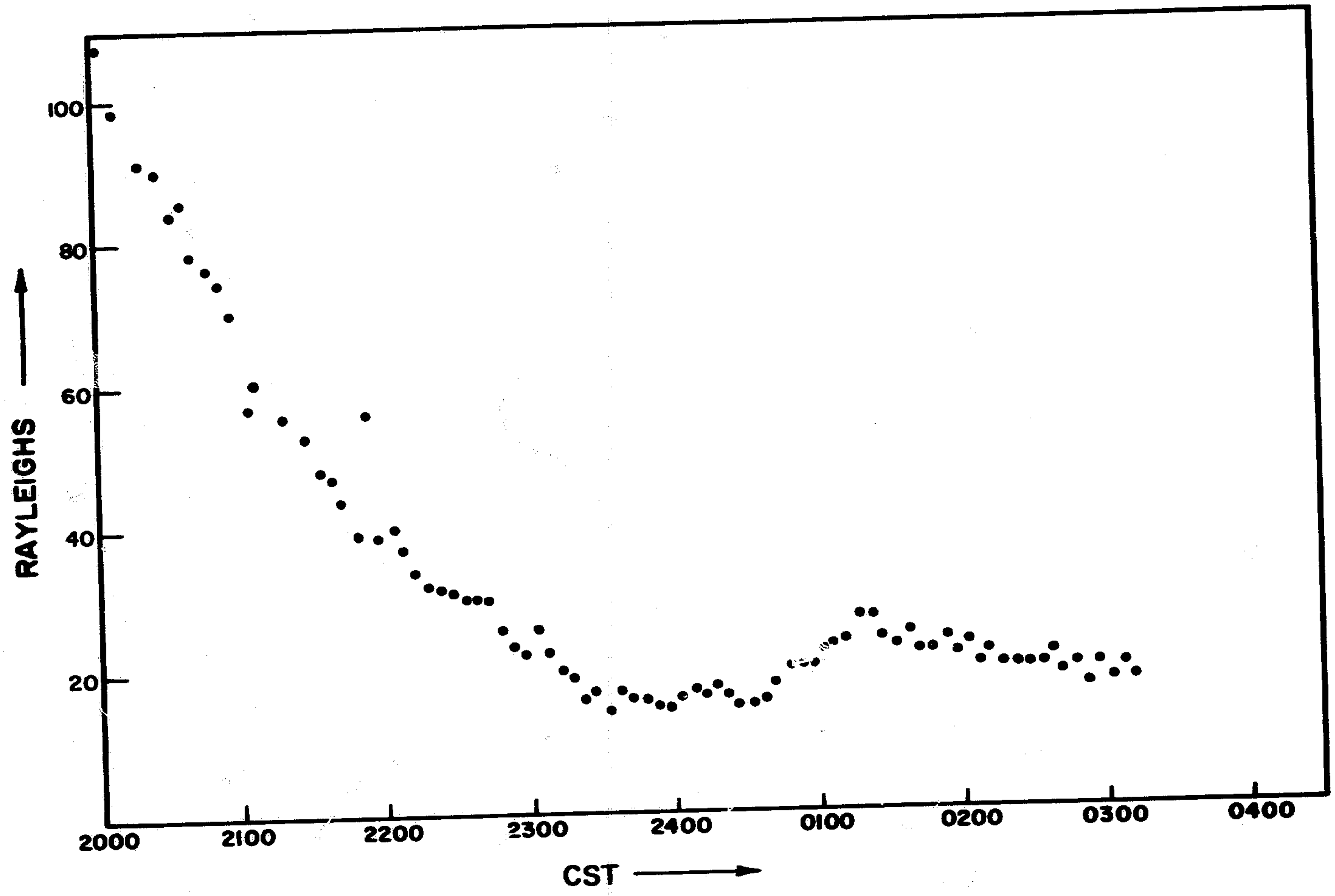

Figure 5.10 OI(6300Å) zenith intensities on the night of September 11/12, 1969.

developed by Budden (1954) which employs linear segments. The method of Doupnik and Schmerling was developed for use on a high speed digital computer and may be scaled at any frequency and for any geographic location. The computer program which is used was written by Dr. N. N. Rao, Electrical Engineering Department, University of Illinois.

The ionograms are recorded photographically on 35 mm film. A digital read-out device is used to convert this 35 mm data to IBM cards for computer input. The accuracy of this instrument is about 3 microns on the 33 mm film, and it is expected that h'(f) traces are able to be read accurately to within 5 km.

5.3.2 Shape preserving solutions of electron continuity equation

The electron density distribution can be theoretically calculated by solving the electron continuity equation:

$$\frac{\partial[e]}{\partial t} = -\beta[e] + \frac{\partial}{\partial z}\left[\sin^2 i D(z)\left(\frac{\partial[e]}{\partial z} + \frac{[e]}{2H_1}\right)\right] \tag{5.2}$$

where β = electron loss coefficient = $\gamma_1[O_2]$

$D(z)$ = ambipolar diffusion coefficient

H_1 = scale height of O

i = angle of inclination of the magnetic field to the horizontal.

Dalgarno's (1964) calculations for the diffusion of O^+ through O may be approximated by

$$D(z) = \frac{.4 \times 10^6 T + 2.9 \times 10^{18}}{[O]} \text{ cm}^2 \text{ sec}^{-1} \tag{5.3}$$

near 1000K.

The solution to Equation (5.2) (Dungey, 1956; Chamberlain, 1961) is a set of eigenfunctions

$$[e] = \sum_{j=o}^{\infty} [e]_j e^{-\lambda_j t} \tag{5.4}$$

where the eigenvalues obey the relation

$$\lambda_j > \lambda_{j-1} \quad . \tag{5.5}$$

The higher order eigenfunctions, because of their time dependence, are short lived and an hour or so after sunset the electron density may be expressed as a linear combination of the first two or three eigenfunctions. The large j's correspond to the base of the F region which is rapidly depleted of electrons in the absence of the sun's radiation. After a few hours the electron density distribution reaches its limiting form

$$[e] = [e]_o e^{-\lambda_o t} \quad . \tag{5.6}$$

The electron distribution curve is given by

$$[e] = Ke^{-z/2H_1} \exp[-H_1 (\frac{\beta_o}{D_o})^{1/2} e^{-z/H_1}] \quad . \tag{5.7}$$

The quantity K is a constant, z is the distance from a reference height, and β_o and D_o are the values of β and D at this reference height. This limiting form is a Chapman layer and its height and shape should not vary with time. Figure 5.11 illustrates electron density profiles at four times for the night of August 6/7, 1969. Note the preservation of shape and approximately constant height of the F layer. Data from most of the other nights behaved consistently in the same manner as outlined above.

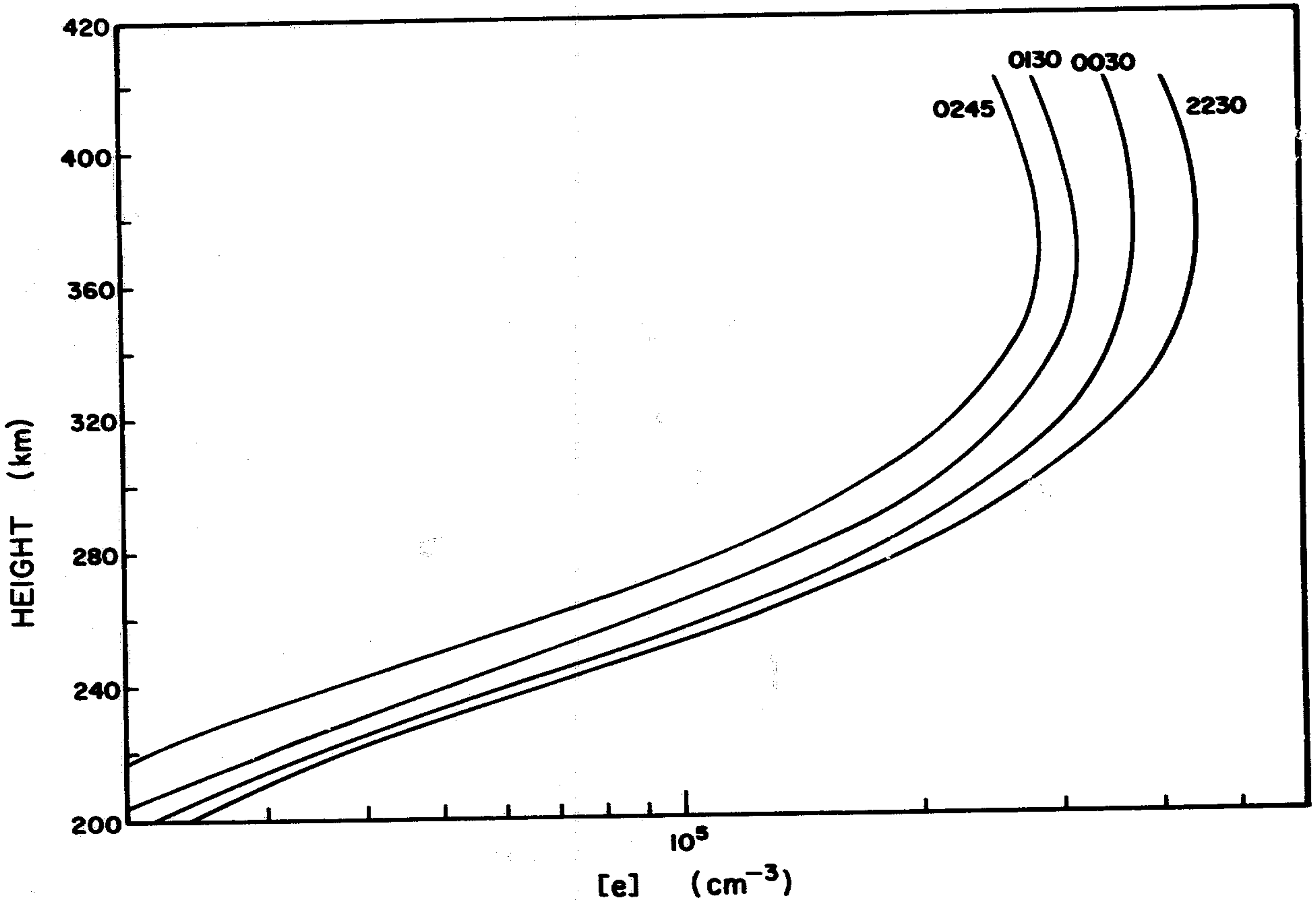

Figure 5.11 Electron density profiles at four times for the night of August 6/7, 1969, illustrating shape-preserving behavior of the F2 layer.

Substituting (5.6) into (3.26), one obtains

$$Q_D = \left[7.6 \times 10^{-7} k_{D_1} \gamma_1 \int_0^\infty \frac{[O_2][e]_o}{1 + 1.1 \times 10^2 \, S_D(N_2)[N_2]} \, dh \right] e^{-\lambda_o t} \quad . \tag{5.8}$$

Thus according to the theory presented in this section and in Chapter 3, the red-line intensity should decrease exponentially with the same time constant as the electron density. To illustrate the validity of this theory, experimental data from the night of August 6, 1969 is presented in Figures 5.12-5.14. Figure 5.12 shows the variation in red-line intensity and height of the F2 layer peak throughout the night. The red-line intensity clearly approximates an exponential decay between 2000 and 0200 CST. Intensity variations which are superimposed on the $e^{-\lambda_o t}$ variation are due to upward and downward movements of the F2 layer. This is because a change in electron density at any height affects the rate of the dissociative recombination reaction responsible for the production of $O(^1D)$. This correlation between the height of the F2 layer and the red-line intensity is supported by the experimental evidence in Figure 5.12, which shows that changes in the height of the F2 layer are in antiphase with changes of the red-line intensity.

Figure 5.13 illustrates the decay of electron density at various altitudes. According to Equation (5.6) a semi-log plot of [e] for different heights vs. time should yield parallel straight lines of constant negative slope. The experimental data in Figure 5.13 agrees with this prediction. There are deviations at the lower altitudes, but since the contribution to the total electron content from this region is small, they are of minor importance. The rate of decay of Q_D and [e] are plotted in Figure 5.14. The slopes of the

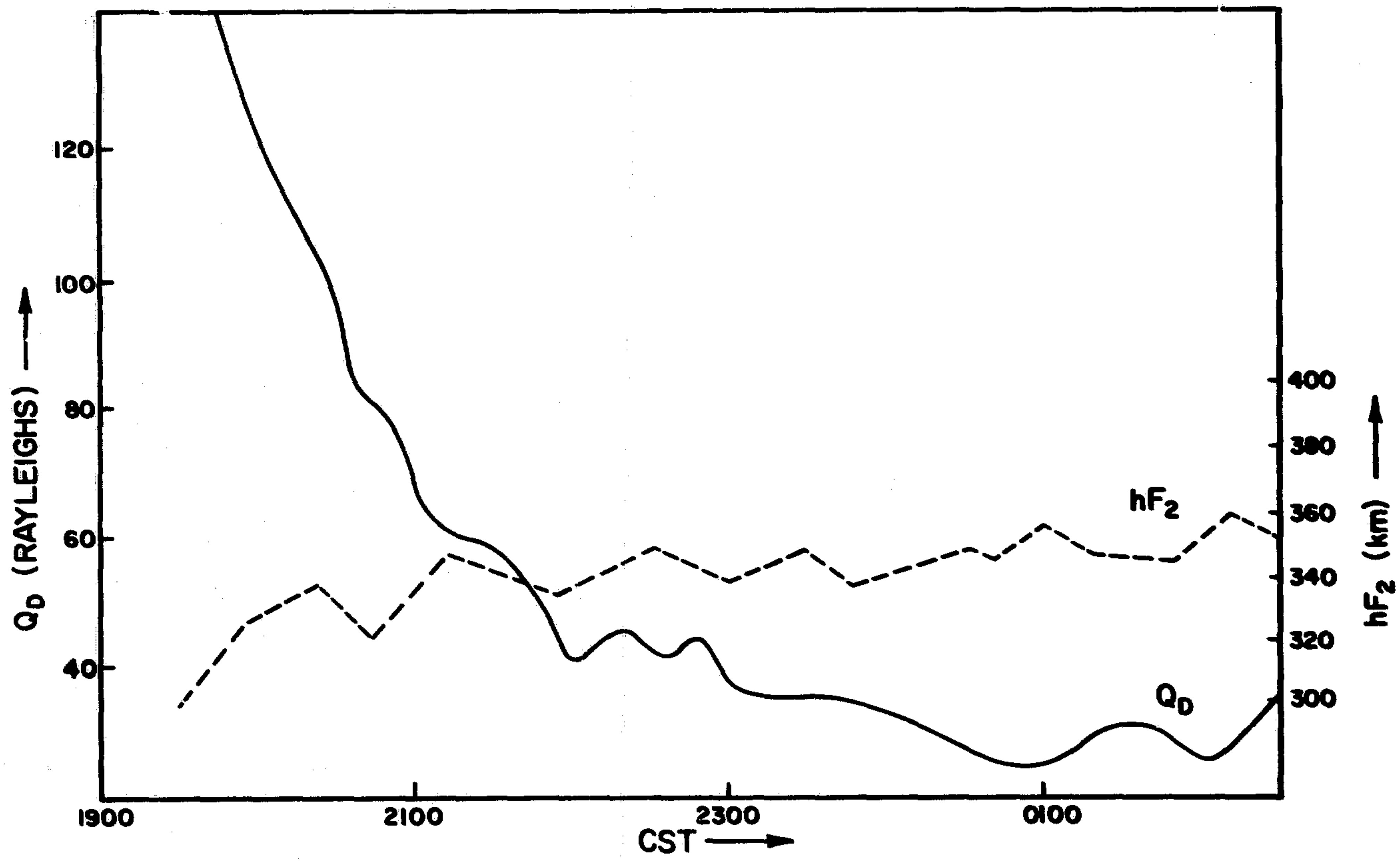

Figure 5.12 Red-line intensity Q_D and height of the F2-layer peak hF2 vs. time for the night of August 6/7, 1969.

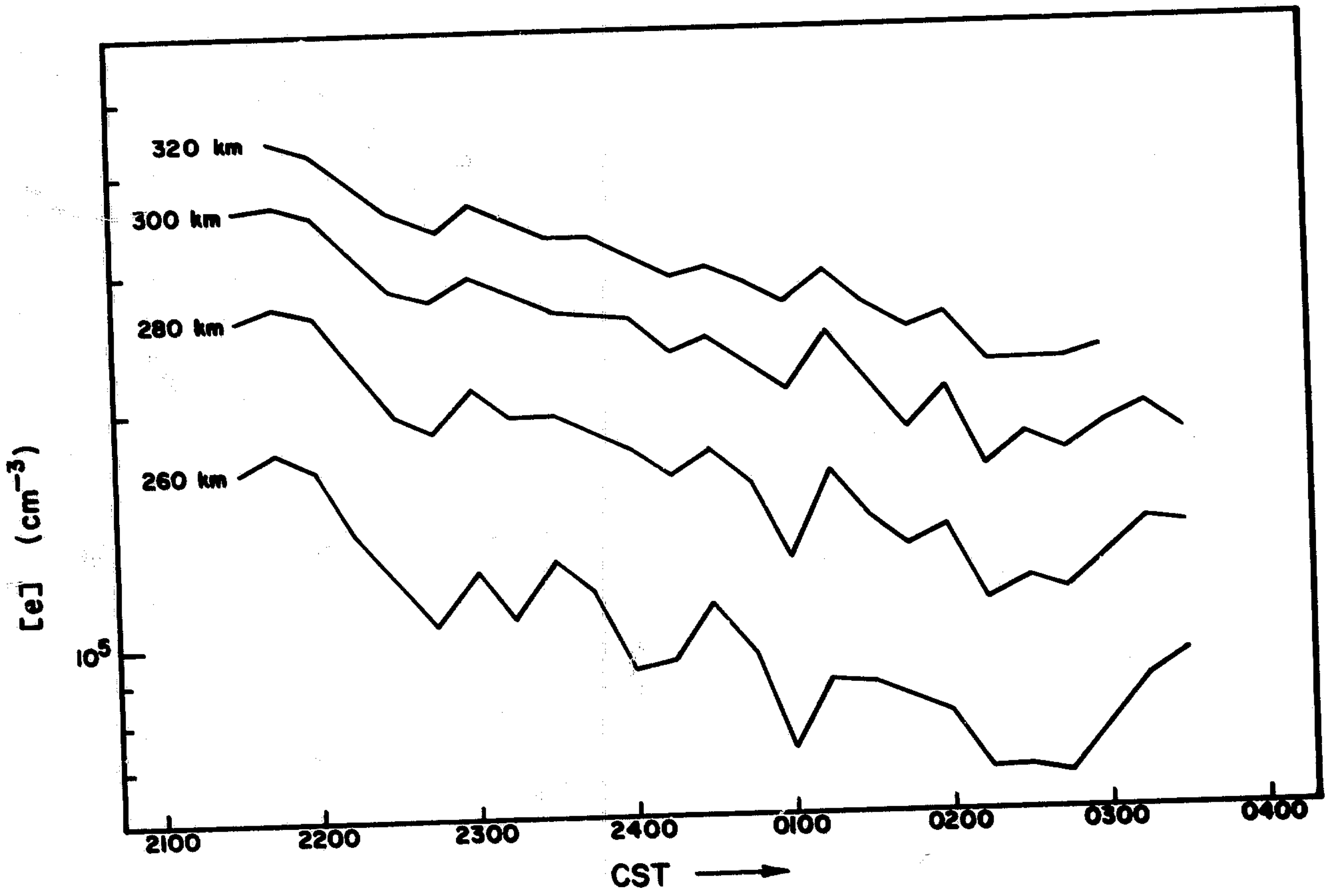

Figure 5.13 Electron density [e] vs. time for various altitudes on the night of August 6/7, 1969.

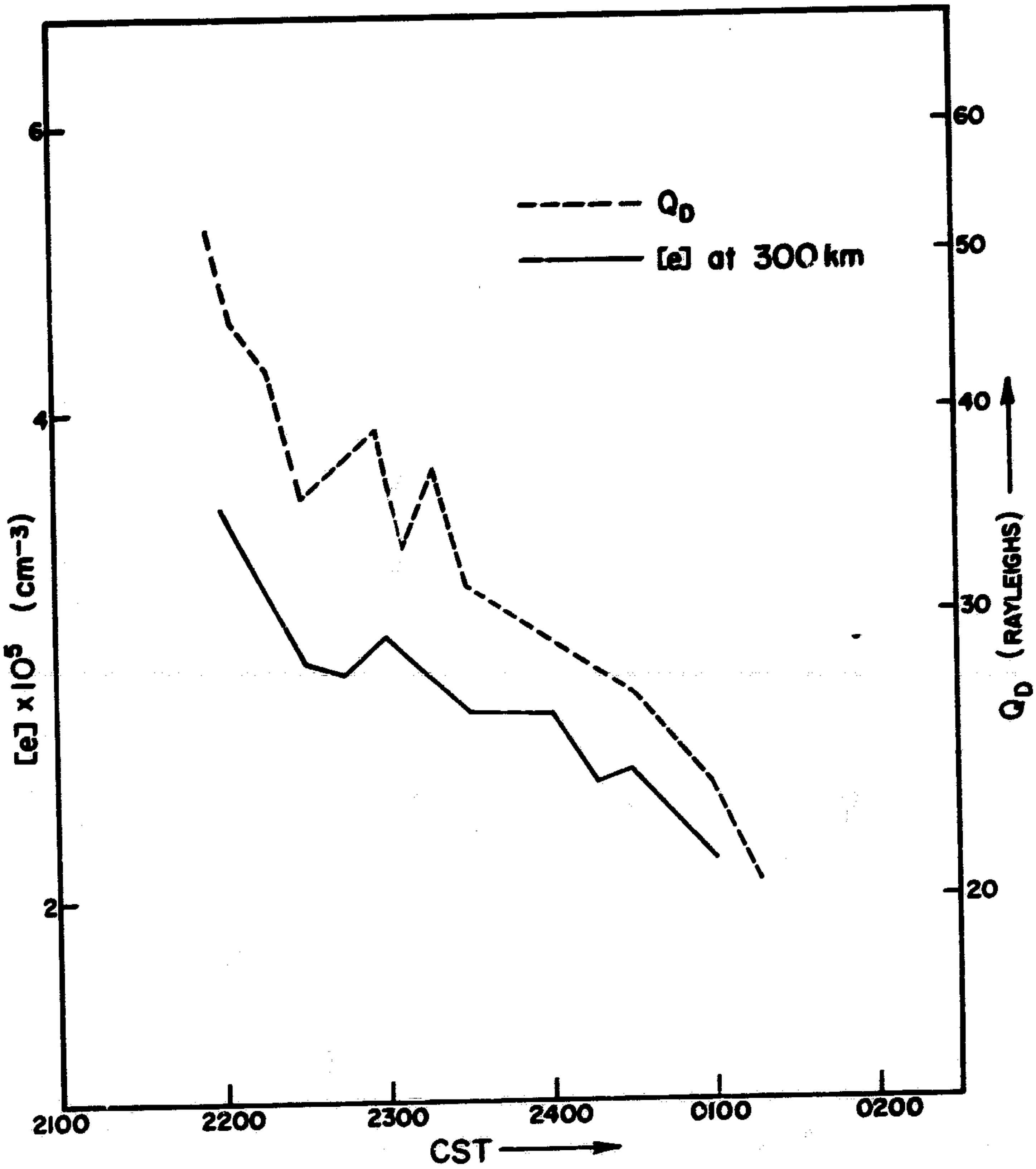

Figure 5.14 Rate of decay of [e] at 300 km and Q_D for the night of August 6/7, 1969.

lines agree quite well. The slightly larger slope of the log Q_D vs. time curve at the beginning of the night is probably due to the more rapid depletion of ionization at the bottom of the layer where a significant portion of the 6300Å emission is radiated. In Chapter 7 it will be shown that the peak OI(6300Å) emission height is above 260 km, so deviations from the shape preserving behavior of the electron distribution below these heights becomes less important to the behavior of the red line intensity.

5.3.3 Determination of exospheric temperature

The Chapman distribution may be closely approximated by a parabola at its peak, and the width of this parabola is a measure of the neutral particle scale height (Dungey, 1956; Wright, 1962). It is most convenient to fit a parabola to the log of the shape preserving solution (Equation 5.7):

$$\log[e] = \log K - H_1 \left(\frac{\beta_o}{D_o}\right)^{1/2} \exp\left(-\frac{z}{H_1}\right) - \frac{z}{2H_1} \quad . \tag{5.9}$$

The vertical distance from the peak of the F2 layer is z. Introducing the series expansion for $\exp(-\frac{z}{H_1})$ and retaining only terms to the second degree,

$$\log[e] = \log K - H_1 \left(\frac{\beta_o}{D_o}\right)^{1/2} + z \left[\left(\frac{\beta_o}{D_o}\right)^{1/2} - \frac{1}{2H_1}\right] - \frac{z^2}{2H_1} \left(\frac{\beta_o}{D_o}\right)^{1/2} \quad . \tag{5.10}$$

This approximation is satisfactory providing z is less than H_1. Equation (5.10) is of parabolic form and its fit to an actual electron density profile yields values for $\left(\frac{\beta_o}{D_o}\right)^{1/2}$ and H_1. A least squares approximation was used in the calculations.

The exospheric temperature T_∞ is related to the scale height H_1 by the relation

$$H_1 = \frac{RT_\infty}{mg} \tag{5.11}$$

where R = universal gas constant

m = molecular weight of atomic oxygen

g = acceleration of gravity .

In Figure 5.15 temperatures calculated by this method are compared with temperatures determined from 10.7 cm solar flux measurements made at Ottawa. The latter procedure is well known and may be found in Section 3.2 of the U.S. Standard Atmosphere Supplements (1966). The points are found to lie close to a line of slope unity and it is therefore concluded that these values closely approximate the true exospheric temperatures.

A further check on the method can be made by considering the value obtained for $(\frac{\beta_o}{D_o})^{1/2}$. Since

$$(\frac{\beta_o}{D_o})^{1/2} = \left[\frac{\gamma_1[O_2]_o[O]_o}{\sin^2 68^\circ \ D_o[O]_o}\right]^{1/2} , \tag{5.12}$$

$D_o[O]_o$ may be calculated knowing γ_1 from laboratory measurements, $[O_2]_o[O]_o$ from the model atmosphere, and $(\frac{\beta_o}{D_o})^{1/2}$ from the parabolic fit. Dalgarno (1964) presents values of $D_o[O]_o$ which can be used for comparison. For an exospheric temperature of 1060K and reference height of 310 km on the night of August 6/7, 1968, $(\frac{\beta_o}{D_o})^{1/2}$ was calculated to be 2.35×10^{-2} cm^{-1}. The calculated value of 2.6×10^{18} cm^{-1} sec^{-1} for $D_o[O]_o$ is low compared to Dalgarno's 6.9×10^{18} cm^{-1} sec^{-1}. Values of $D_o[O]_o$ from other sets of data were about a factor of two or three below Dalgarno's values. This discrepancy is probably due to the approximate nature of the parabolic fit method and

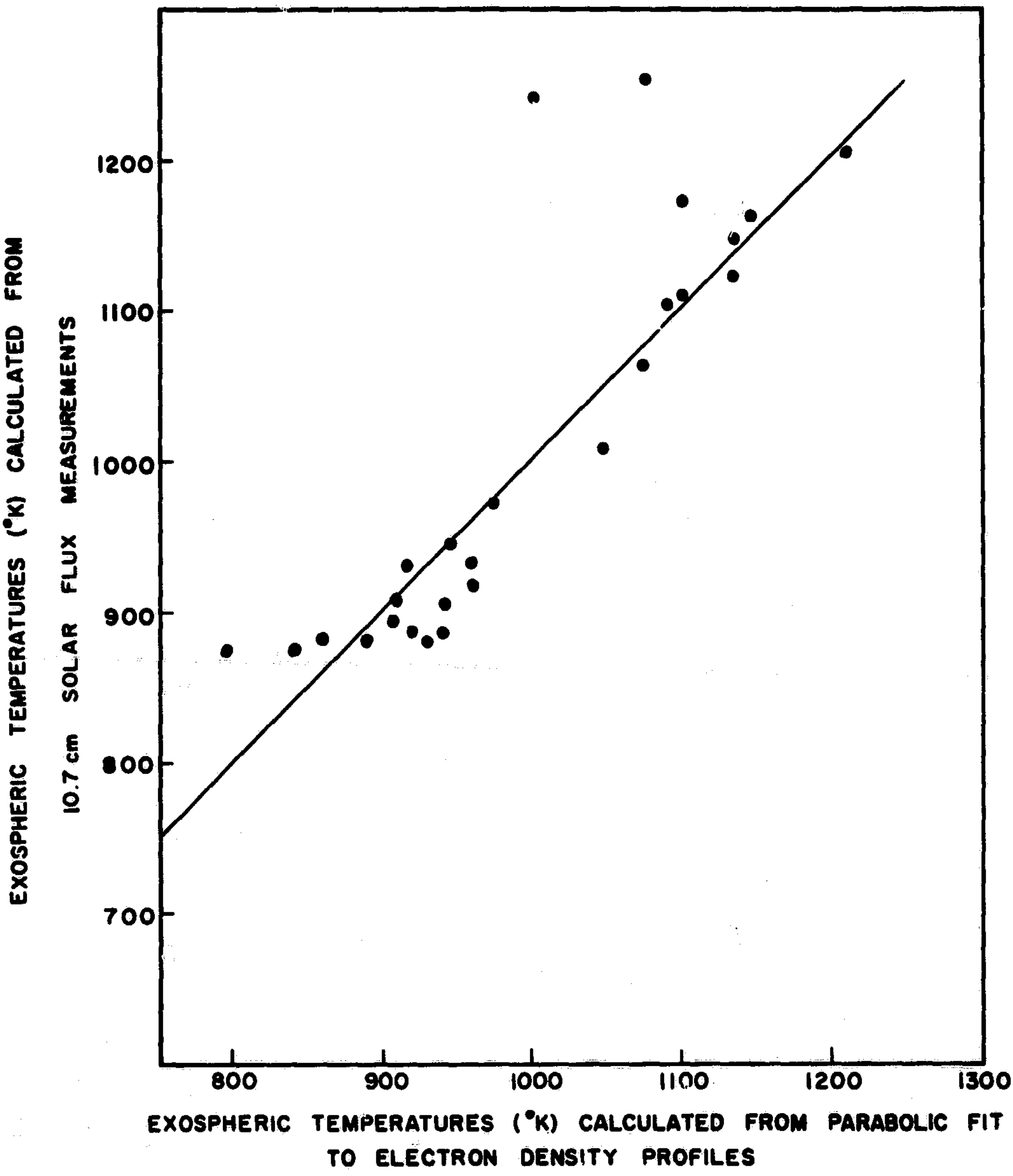

Figure 5.15 Comparison of exospheric temperatures calculated from 10.7 cm solar flux measurements and parabolic fit to electron density profiles (points are hourly averages for 2200-0300 CST for the months of July and August when data was available).

deviations of the actual electron density profiles from a Chapman distribution. However, it is concluded that these results satisfactorily indicate that the theory underlying the parabolic fit method of determining exospheric temperatures is approximately correct.

In the next section, the exospheric temperature is used as one of the boundary conditions needed to determine an atmospheric model.

5.4 Model Atmosphere

The atmospheric model used through the analysis is an analytic model which is originally due to Bates (1959) and was developed by Stein and Walker (1965) to include a wide range of boundary conditions. This model assumes an atmosphere in diffusive equilibrium above a certain altitude, h_o, and integration of the equation of hydrostatic equilibrium,

$$\frac{1}{k}\frac{dp_i}{dh} = \frac{d[i]}{dh} T + \frac{dT}{dh} [i] = \frac{g[i]m_i}{k} \qquad (5.13)$$

where p_i = partial pressure of the ith constituent

$[i]$ = number density of the ith constituent

m_i = molecular mass of the ith constituent

T = absolute temperature

h = altitude

g = the gravitational acceleration

k = Boltzmann's constant

and assuming a temperature profile of the form

$$T(z) = T_\infty(1-Ae^{-\tau z}) \; ; \; A = 1 - \frac{T_o}{T_\infty} \qquad (5.14)$$

where z = geopotential altitude

T_∞ = exospheric temperature

T_o = temperature at X_o

and τ determines the temperature gradient at X_o, yields the number density of the ith constituent as a function of altitude:

$$[i] = [i]_o \left[\frac{1 - A}{e^{\tau z} - A} \right]^{1+\gamma} e^{\tau z} \; ; \; \gamma = \frac{m_i g_o}{\tau k T_\infty} \; . \qquad (5.15)$$

The boundary conditions applied are:

h_o = 120 km

$[O_2]_o = 7.5 \times 10^{10}\ \text{cm}^{-3}$

$[N_2]_o = 4 \times 10^{11}\ \text{cm}^{-3}$

$[O]_o = 7.6 \times 10^{10}\ \text{cm}^{-3}$

T_o = 350°K

$\tau = 3.6 \times 10^{-7}\ \text{cm}^{-1}$

Exospheric temperatures calculated by the method described in Section 5.3.3 are inserted into Equation (5.14) to determine the temperature profile. The exospheric temperature varied from 800K to 1200K for the nights when data was taken. Figure 5.16 shows a temperature profile for an exospheric temperature of 1000K. The assumption in Section 3.3 that the region of interest is isothermal is shown to be fairly good, and it should be noted that this profile is in agreement with the one given by the U.S. Standard Atmosphere (1966) for the same exospheric temperature. Equation (5.15) is then used to find the height distribution of $[O_2]$, $[N_2]$, and $[O]$.

This chapter has shown the methods which are used to find values of Q_D, $[e]$, $[O_2]$, and $[N_2]$. The airglow intensities are measured with a ground-based

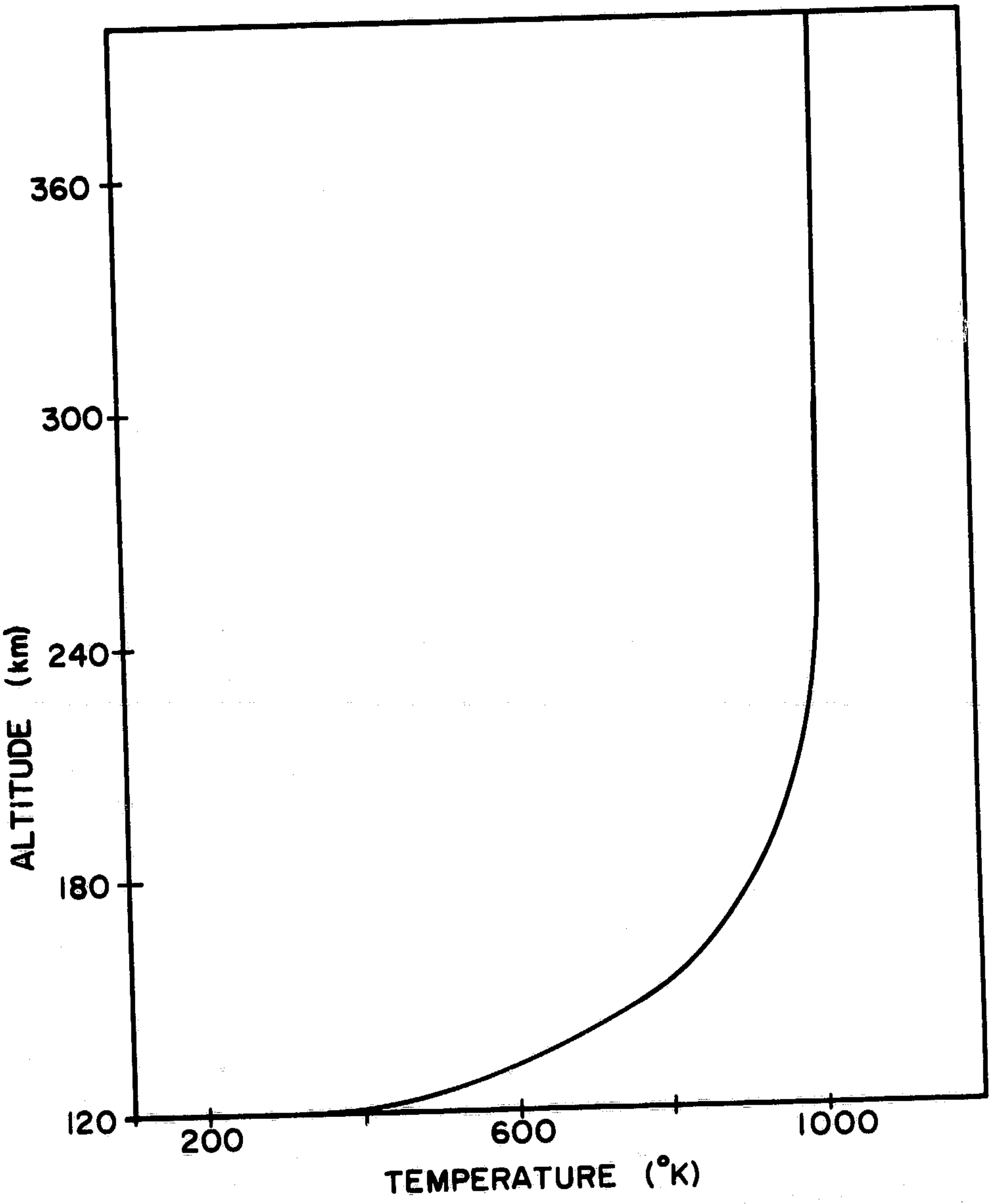

Figure 5.16 Temperature profile for exospheric temp. = 1000 K.

photometer. The electron density distributions are determined from ionograms which are taken simultaneously with the airglow observations. It has been shown from experimental evidence that the electron density and red-line intensity decrease with the same time constant, in agreement with the theory presented in Sections 3.3 and 5.3.2. A model atmosphere is assumed to calculate $[O_2]$ and $[N_2]$. Exospheric temperatures needed to determine the proper atmospheric model result from a parabolic fit to the electron density profiles assuming they approximate a Chapman distribution. The quantities Q_D, γ_1, [e], $[O_2]$, and $[N_2]$ will be utilized in the next chapter in conjunction with Equation 3.26 to calculate a relationship between K_{D_1} and $S_D(N_2)$.

6. QUENCHING OF THE $O(^1D)$ EMISSION

6.1 Introduction

Equation (3.26) is a theoretical relationship between the OI(6300Å) volume emission rate Q_D, the atmospheric parameters $[O_2]$, $[N_2]$, and $[e]$, and the rate coefficients γ_1, K_{D_1}, and $S_D(N_2)$. To find a relationship between K_{D_1} and $S_D(N_2)$, the remaining quantities in Equation (3.26) must be known. The previous chapter described the methods which are used to determine these remaining quantities. In Section 6.2 actual experimental data are utilized in conjunction with Equation (3.26) to relate K_{D_1} and $S_D(N_2)$. In Section 6.3 the theoretical temperature dependence of $S_D(N_2)$ is calculated from a statistical model for the decomposition of the activated nitrous oxide complex. This result is used in conjunction with the experimental data to show that K_{D_1} remains constant in the 800K to 1200K temperature range. A choice of $S_D(N_2) = 7 \times 10^{-11}$ $cm^3\ sec^{-1}$ is shown to be justified, and from the relationship between K_{D_1} and $S_D(N_2)$ calculated in Section 6.2, K_{D_1} is found to lie in the range $.06 < K_{D_1} < .18$.

6.2 Relationship between K_{D_1} and $S_D(N_2)$

For each time when both airglow intensities and ionograms are available, the appropriate model atmosphere is determined, and Equation (3.26) is used to relate K_{D_1} and $S_D(N_2)$. Now there are an infinite number of values of K_{D_1} and $S_D(N_2)$ which can satisfy Equation (3.26) when the other quantities are known. Thus a K_{D_1} vs. $S_D(N_2)$ curve is obtained for each set of Q_D, $[e]$, and the model atmosphere.

Exospheric temperatures for the data ranged from 800K to 1200K. Due to the possibility that K_{D_1} or $S_D(N_2)$ may exhibit a temperature dependence, the data is separated into four groups according to temperature:

Group I - 800K to 900K;

Group II - 900K to 1000K;

Group III - 1000K to 1100K;

Group IV - 1100K to 1200K.

For each set of Q_D and [e] within each group, a relationship is found between $S_D(N_2)$ and K_{D_1}. Thus a number of $S_D(N_2)$ vs. K_{D_1} curves is obtained within each group. For illustrative purposes, the Group III data are presented in Figure 6.1. The curves are nearly parallel, and spread apart somewhat due to the differences in temperature and errors inherent in the experimental technique and data reduction. Statistical information on the four groups of data appears in Table II. The next step is to average the curves within each group and thus obtain one curve for each group which represents the average K_{D_1} vs. $S_D(N_2)$ behavior for the average temperature of the group. The final result is four K_{D_1} vs. $S_D(N_2)$ curves at their respective average temperatures (see Figure 6.2).

The curves of Figure 6.2 are averages over different nights and therefore over slightly different atmospheric conditions. In addition, large variations in the value of Q_D(15R-100R) are also represented. If there is contamination present from other light sources, the Q_D used in Equation (3.26) should be smaller. This would cause a corresponding decrease in K_{D_1} and an increase in $S_D(N_2)$. The effect of atmospheric absorption would tend to increase the value of Q_D that should be used in Equation (3.26), thus making K_{D_1} slightly larger and $S_D(N_2)$ slightly smaller.

A possible procedure at this point would be to pick a likely value of $S_D(N_2)$ or K_{D_1} and read the other directly from the curves in Figure 6.2. However, these curves definitely indicate a temperature dependence of these quantities and it is the purpose of the present discussion to find out just how important

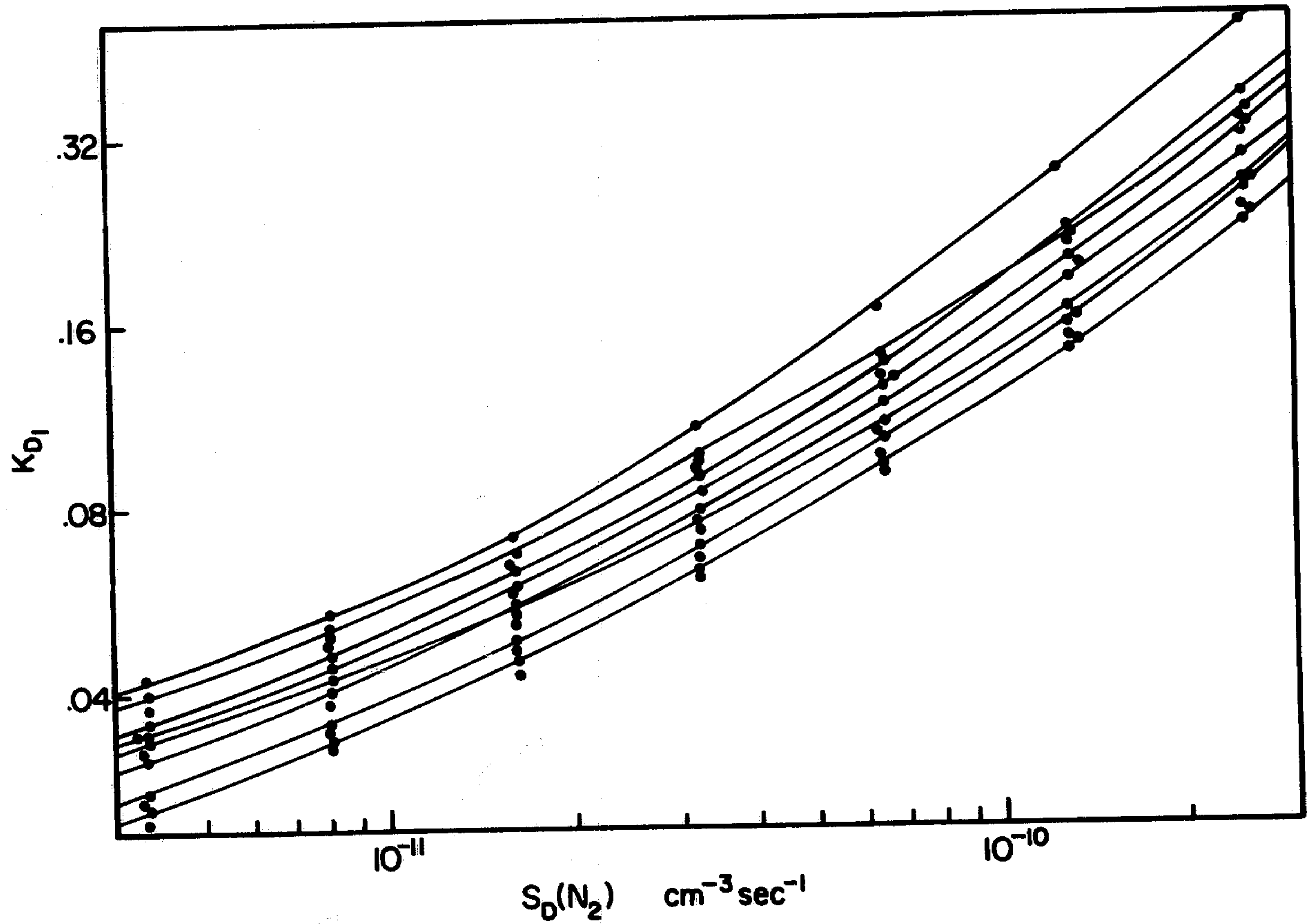

Figure 6.1 K_{D_1} vs. $S_D(N_2)$ curves for the Group III data.

TABLE II

DATA USED IN FIGURE 6.1

	Number of nights represented	Number of $S_D(N_2)$ vs. K_{D_1} curves obtained	Standard deviation of K_{D_1} at $S_D(N_2) = 7 \times 10^{-11}$ $cm^3\ sec^{-1}$
Group I	5	10	.004
Group II	4	16	.013
Group III	3	13	.002
Group IV	4	14	.012

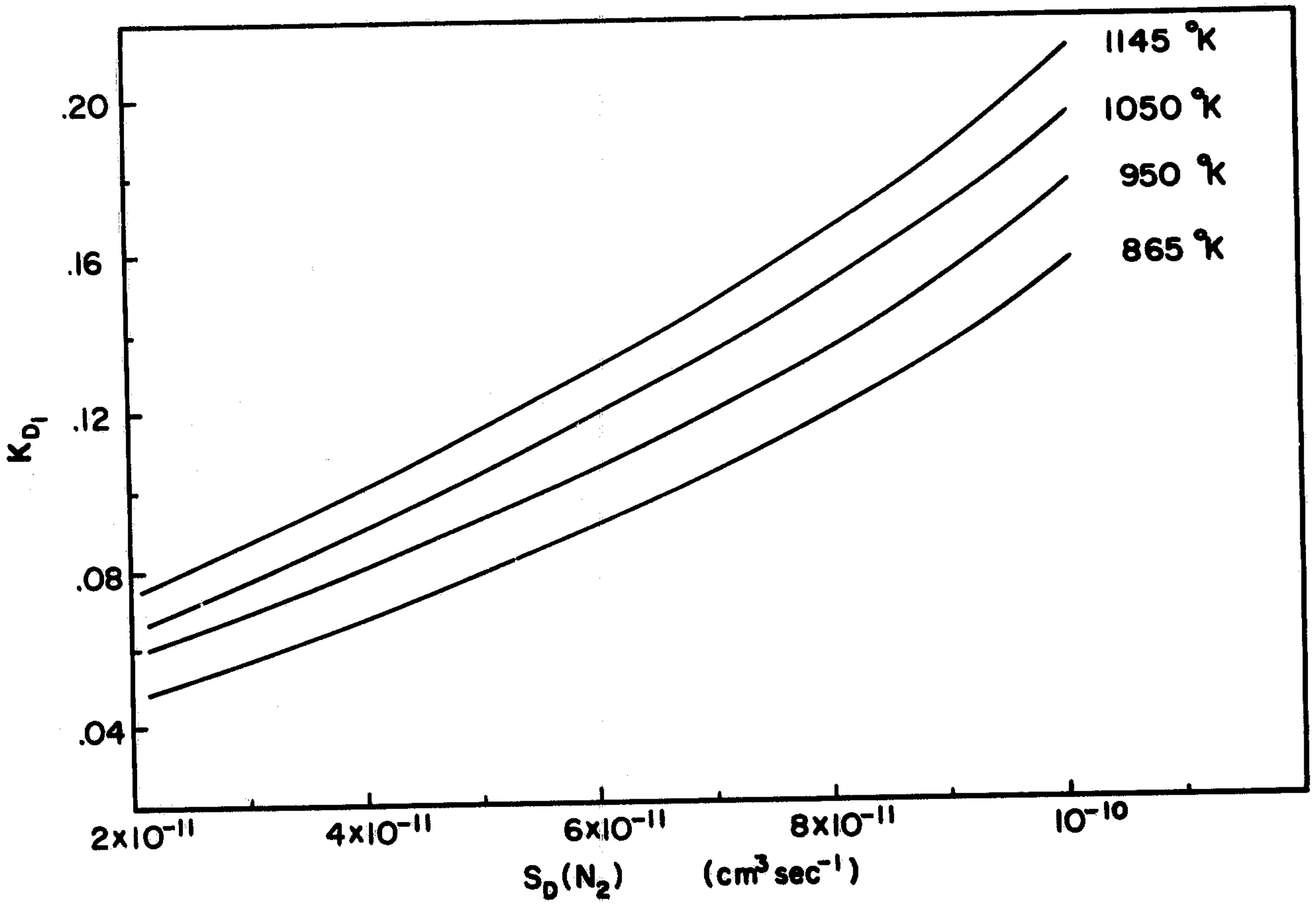

Figure 6.2 K_{D_1} vs. $S_D(N_2)$ curves for different exospheric temperatures.

this dependence might be. Although the separation between the curves appears to be rather small, it is possible that a large temperature variation is present in one or both of these quantities. For instance, a study of Figure 6.2 reveals the following possible temperature variations with respect to increasing temperature:

(1) Large decrease in $S_D(N_2)$ and a small decrease in K_{D_1}.

(2) Small decrease in $S_D(N_2)$ and a constant or slightly increasing K_{D_1}.

(3) Increase in $S_D(N_2)$ and a corresponding increase in K_{D_1}.

Demore and Raper (1962) and Snelling and Blair (1967) have shown experimentally that Equation (2.22) proceeds with essentially zero activation energy. That is, all collisions of N_2 with $O(^1D)$ result in the formation of a vibrationally-excited nitrous oxide complex. In the light of this evidence it seems very likely that reaction (2.22) is the correct mechanism for quenching of $O(^1D)$. The theory of decomposition of such a molecule is known at least well enough to predict the direction of temperature dependence of the decomposition rates. This theory will be applied to reaction (2.22) in the next section and it will be found that quenching of $O(^1D)$ by N_2 slightly decreases in efficiency as the temperature increases. This immediately eliminates possibilities (1) and (3) above and indicates that K_{D_1} remains relatively constant in the 800K to 1200K temperature range.

6.3 Temperature Dependence of the Quenching Coefficient

The temperature dependence of reaction (2.22) may be calculated by using the Rice-Ramsperger-Kassel (RRK) method (Benson, 1960; Johnston, 1966; Demore and Raper, 1964). Reaction (2.22) is first rewritten:

$$O(^1D) + N_2(X^1\Sigma_g^+) \xrightarrow{k_1} N_2O^*(X^1\Sigma_g^+) \tag{6.1}$$

$$N_2O^*(X^1\Sigma_g^+) \xrightarrow{k_2} N_2(X^1\Sigma_g^+) + O(^1D) \qquad (6.2)$$

$$N_2O^*(X^1\Sigma_g^+) \xrightarrow{k_3} N_2(X^1\Sigma_g^+) + O(^3P) \qquad (6.3)$$

The rate coefficient for quenching of $O(^1D)$ by N_2 is equal to $k_1/(1 + k_2/k_3)$.

The RRK statistical model consists of S oscillators all of the same frequency, coupled so that the state of the system (the activated complex) is given by its total vibrational energy. This model neglects perturbations due to coupling. In the limit of classical mechanics, an expression is written for k_2/k_3 (Demore and Raper, 1964):

$$\frac{k_2}{k_3} = \frac{A_2}{A_3}\left(\frac{E - E_2}{E - E_3}\right)^{S-1} \qquad (6.4)$$

where A_2 = frequency factor for (6.2)

A_3 = frequency factor for (6.3)

E_2 = critical energy for redissociation to $O(^1D)$ and N_2 = 84 Kcal

E_3 = critical energy for predissociation to $O(^3P)$ and N_2 = 55 Kcal

S = number of effective oscillators of N_2O^*

E = total energy of N_2O^*

Johnston (1966) compares calculations of other molecules using the quantum-statistical model and the classical model, and finds that the classical model is not a bad approximation. However, because of the uncertainty in determining A_2/A_3 and S for the present mechanism, values for these quantitites will be chosen which yield the highest k_2/k_3. Thus an upper limit will be found for k_2/k_3 which in turn will determine the highest rate of decrease of the rate coefficient vs. temperature that is possible. Since the mechanism has essentially zero activation energy (Demore and Raper, 1962), the thermal energy of the reactants has no influence on reaction (6.1), implying that k_1 is constant with temperature. Demore and Raper (1964) conclude that out of the possible values for A_2/A_3 and S, the following yield the highest k_2/k_3: $A_2/A_3 = 10^2$, $S = 2$. The total energy E is equal to the exothermicity of reaction (6.1) plus a contribution of thermal energy equal to SRT. Equation (6.4) may now be written

$$\frac{k_2}{k_3} = 10^2 \frac{2RT + 70}{2RT + 29170} \tag{6.5}$$

where the energies are now written in calories and R is the universal gas constant. The decrease in the quenching coefficient vs. temperature is plotted in Figure 6.3 and is normalized to the value of the coefficient at 300K. Thus a temperature increase from 300K to 1000K results in a decrease of about .6 in the quenching coefficient. It is emphasized that this is only an upper limit, and the decrease in $S_D(N_2)$ may thus lie anywhere between 0 and .6. Although the temperature variation is seen to be significant between 300K and 1000K, the value of $S_D(N_2)$ at higher temperatures is apparently not as sensitive to changes in temperature, and can be assumed to remain relatively constant between 800K and 1000K.

6.4 Results

Utilization of the data presented in Figure 6.2 requires the knowledge of either K_{D_1} or $S_D(N_2)$ to infer the other. In the light of recent laboratory (Noxon, 1968; Young, et al. 1968) and aeronomical (Peterson and Van Zandt, 1969) studies, and the theoretical calculation for the temperature dependence of

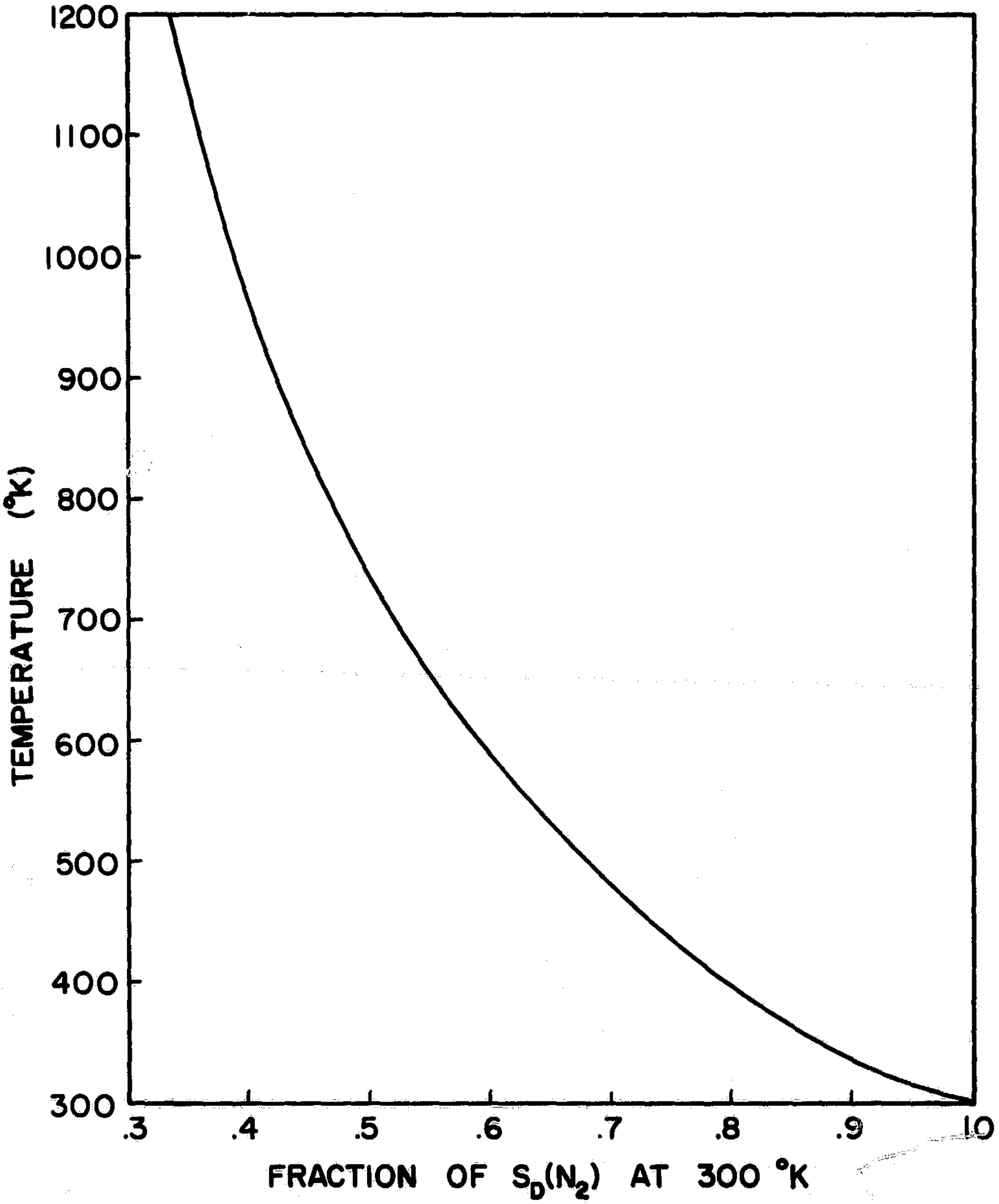

Figure 6.3 Decrease in $S_D(N_2)$ vs. temperature calculated by the RRK method and normalized to 300°K.

$S_D(N_2)$ made in the previous section, $S_D(N_2)$ is probably better known than ever before. This is because these methods of determining $S_D(N_2)$ are independent of K_{D_1} and hence can be used to infer a value for K_{D_1} from the data in Figure 6.2.

Recent laboratory measurement of the rate coefficient for quenching of $O(^1D)$ has been made by Noxon (1968) who reports a value of $S_D(N_2) = 1 \times 10^{-10}$ cm^3/sec, and by Young, et al. (1968) who find $S_D(N_2) = 5 \times 10^{-11}$ cm^3/sec. According to the temperature dependence calculated in the previous section, a laboratory value of $S_D(N_2)$ measured at 300K could decrease as much as a factor of three upon extrapolation to 1000K. Thus the rate coefficient at 1000K could be as small as 2×10^{-11} cm^3/sec or as large as 1×10^{-10} cm^3/sec. At this point one could do no better than assume that an intermediate value, of say 6×10^{-11} cm^3/sec, is a reasonable estimate.

Peterson and Van Zandt (1969) have calculated a rate coefficient of 5×10^{-11} cm^3/sec to 1×10^{-10} cm^3/sec depending on the model atmosphere used. Their technique for obtaining $S_D(N_2)$ depends on the fact that the F2 layer experiences large height excursions near the equator. By observing the relative variation in red line intensity for the upward and downward movements of the layer, they were able to deduce the above values for $S_D(N_2)$ within an accuracy of a factor of 2. Because the method only requires relative variations in the red line intensity, their results are independent of the calibration of the photometer, and of the constants K_{D_1} and γ_1. Their results fall in the same range as the aforementioned laboratory measurements.

Assuming a compromise value of $S_D(N_2) = 7 \times 10^{-11}$ cm^3/sec in the 800K to 1200K range, Figure 6.1 now yields values of K_{D_1} from .10 at 865K to .15 at 1145K. This predicts a slightly increasing K_{D_1} with temperature. Now the curves in Figure 6.1 were originally calculated in the analysis as a plot of

$\gamma_1 K_{D_1}$ vs. $S_D(N_2)$, and a constant value of $\gamma_1 = 2.5 \times 10^{-11}$ cm^3/sec was used to obtain the K_{D_1} - $S_D(N_2)$ curves. This procedure is satisfactory providing all one wants to obtain is an estimate of K_{D_1} in this temperature range. However, it is emphasized that a slight temperature dependence of K_{D_1} cannot be inferred from Figure 6.2 due to the fact that the temperature dependence of γ_1 has been ignored in the calculations. The measurements of Dunkin (1968) and Bohme, et al. (1967) indicate that γ_1 increase slightly in this temperature range. Taking this into account, K_{D_1} reduces to a steady value of .1 between 865K and 1145K. For other possible values of $S_D(N_2)$, K_{D_1} varies from about .06 to .18.

7. DISCUSSION AND SUGGESTIONS FOR FUTURE WORK

7.1 Results

Since the rate coefficient for quenching of $O(^1D)$ by O_2 is less than that by N_2 (Noxon, 1968; Young et al., 1968), and because N_2 is in greater abundance than O_2 above 120 km, the dominant quencher of $O(^1D)$ in this region of the upper atmosphere is concluded to be N_2.

A value of $.06 < K_{D_1} < .18$ is deduced by comparing the observed red-line intensity in the night airglow with theoretical calculations of the red-line intensity based on measurements of $S_D(N_2)$ made by Noxon (1968), Young et al., (1968), and Peterson and Van Zandt (1969), a model atmosphere (Stein and Walker, 1965), a laboratory-determined value of γ_1 (Bohme et al., 1967; Warneck, 1967; Dunkin et al., 1968), and electron density profiles determined from ionograms taken simultaneously with the airglow observations. This range of values for K_{D_1} is calculated on the assumption that all $O(^1D)$ is produced by dissociative recombination of O_2^+. If a value greater than the maximum possible value of 2 had been calculated, then this would indicate that perhaps the dissociative recombination of NO^+ should have been included in the theory. However, $K_{D_1} > 2$ is not the only condition under which this conclusion can be made. Although K_{D_2} is believed to be small, it has been shown that K_{D_1} is at least an order of magnitude smaller than its maximum possible value. In Section 3.3 it was shown that the relative contribution to the airglow intensity of the dissociative recombination of NO^+ as opposed to the dissociative recombination of O_2^+ is given approximately by K_{D_2}/K_{D_1}. Therefore, for a value of $K_{D_1} = .1$, a value of K_{D_2} as small as .01 would indicate that 10% of the total OI(6300Å) airglow intensity is due to the dissociative recombination of NO^+. Hence the dissociative recombination of NO^+ could possibly contribute a significant amount of the OI(6300Å) nightglow.

Assuming that the quenching of $O(^1D)$ by N_2 involves intermediate formation of N_2O^* (Demore and Raper, 1962, 1964; Snelling and Blair, 1967), a theoretical estimate based on the RKK statistical model (Benson, 1960; Johnston, 1966; Demore and Raper, 1964) for the maximum possible rate of decrease of $S_D(N_2)$ vs. temperature was calculated. The rate coefficient for quenching can decrease as much as a factor of 3 from 300K to 1000K. This is an upper limit, and the true rate of decrease of $S_D(N_2)$ with temperature is probably less. In addition, the temperature dependence is steepest at the lower temperatures, and it is concluded that temperature variations of $S_D(N_2)$ between 800K and 1200K are negligible. From the experimental data, this implies that K_{D_1} remains constant in this temperature range.

The height distributions of the 6300Å emission rate and the electron density for 0200 CST on the night of August 6/7, 1969, are plotted in Figure 7.1. The height of the F2-layer peak is 360 km and the maximum rate of 6300Å emission lies at 290 km. The half-width of the ε_D height distribution is approximately 100 km. These distributions are representative of all data taken, the height of the F2-layer peak never falling below 340 km or above 390 km, and the height of peak ε_D always remaining between 240 km and 300 km. One should also note that not much OI(6300Å) emission originates above the peak of the F2 layer, and thus the assumption of a Chapman distribution above the peak does not introduce much error in calculated red-line intensities.

The importance of quenching in studies of the red line can be illustrated by Figure 7.2 where the quenching factor

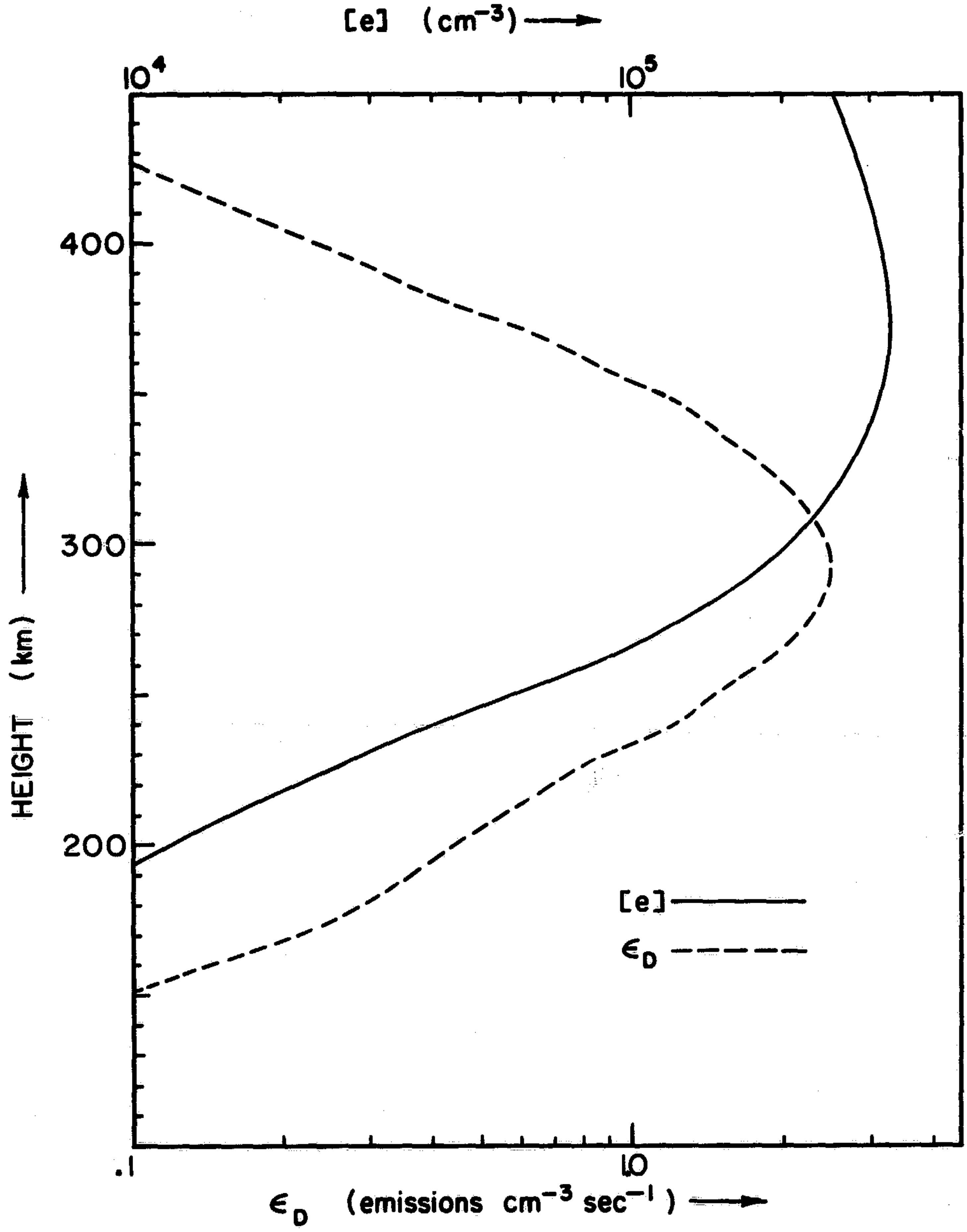

Figure 7.1 Height distributions of electron density [e] and OI(6300Å) emission rate ϵ_D.

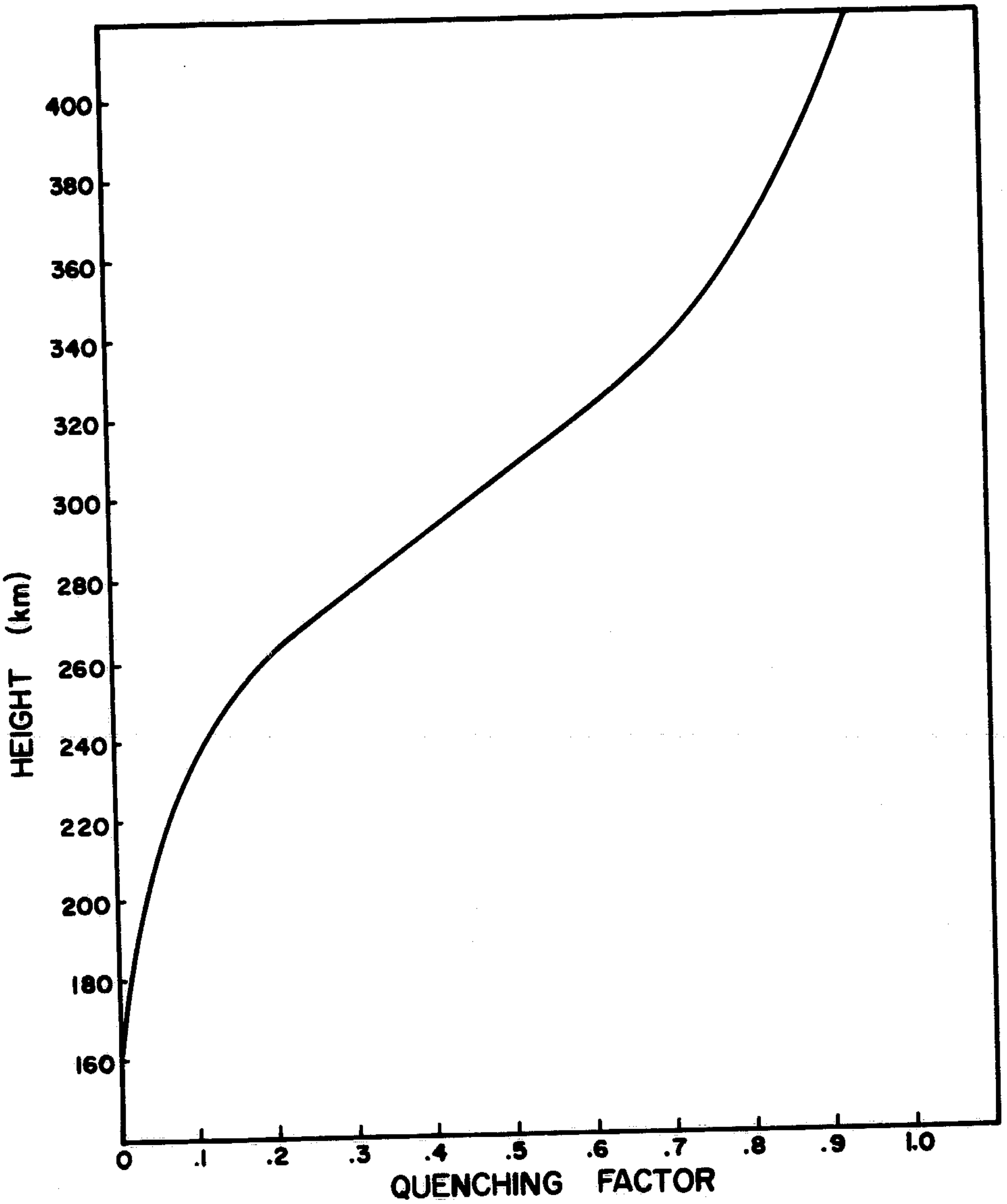

Figure 7.2 Quenching factor vs. height for $S_D(N_2)$ = 7×10^{-11} cm^{3}sec^{-1}.

$$\frac{1}{1 + 1.1 \times 10^{2}\, S_D(N_2)[N_2]} \tag{7.1}$$

is plotted vs. altitude for $S_D(N_2) = 7 \times 10^{-11}$ cm^3 sec^{-1} and an exospheric temperature of 1100K. Expression (7.1) is the factor in Equation (3.26) which accounts for the effect of quenching. It is seen that quenching can be important even above 300 km and becomes drastically important at lower altitudes.

From the experimental data, and expression (3.38) for the constant B in Barbier's formula (3.27), values of $3.5 \leq B \leq 4.5$ were calculated. However, comparisions with observed airglow intensities show that these values are too high, and that B should lie in the range $3.3 \leq B \leq 4.0$. Figures 7.3 and 7.4 compare observed airglow intensities with intensities calculated from Barbier's formula for B = 3.5 and B = 4.0. In Figure 7.3 the curve for B = 3.5 fits the observed intensities much better than for B = 4.0, whereas in Figure 7.4 both values give satisfactory results. The high values of B calculated from Equation (3.38) are partially due to the failure of Barbier's formula to include the effects of quenching, and also to the other simplifications which were made in its derivation. In particular, the value of $<[O_2]>$, the mean molecular oxygen concentration in the F layer, should be taken below the F2-layer peak where the peak emission height is found. When the emission layer is low and the effects of quenching become more important, even smaller values of B will be more appropriate. The height of peak emission never fell below 250 km when data was taken, so it was impossible to determine how important this effect could be. However, the fact that such a low layer of emission did not occur could indicate that such an event is in fact rare at this latitude, and that a value of B = 3.5 would be suitable for future calculations.

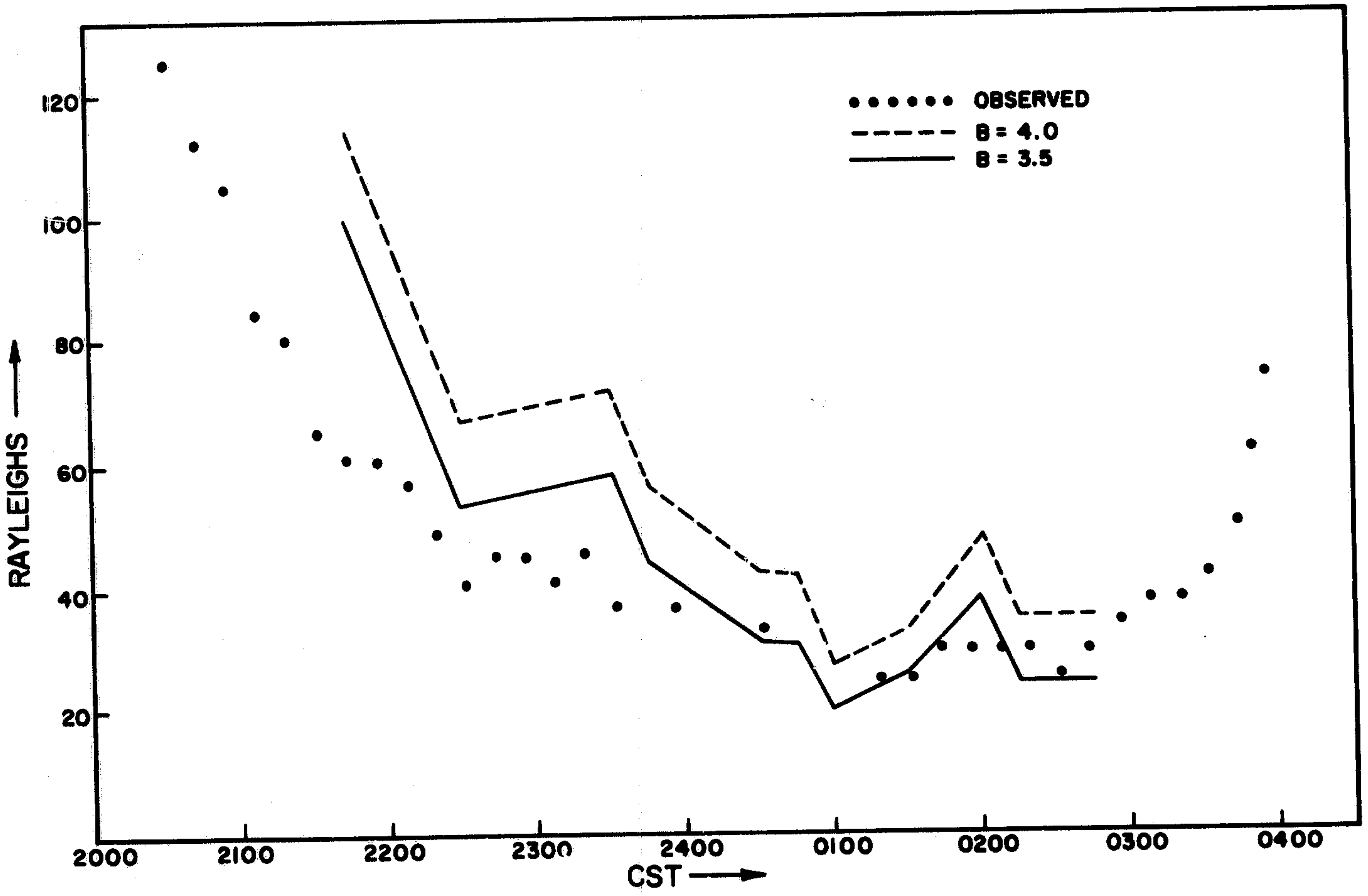

Figure 7.3 Comparison of observed OI(6300Å) intensities with intensities calculated from Barbier's formula.

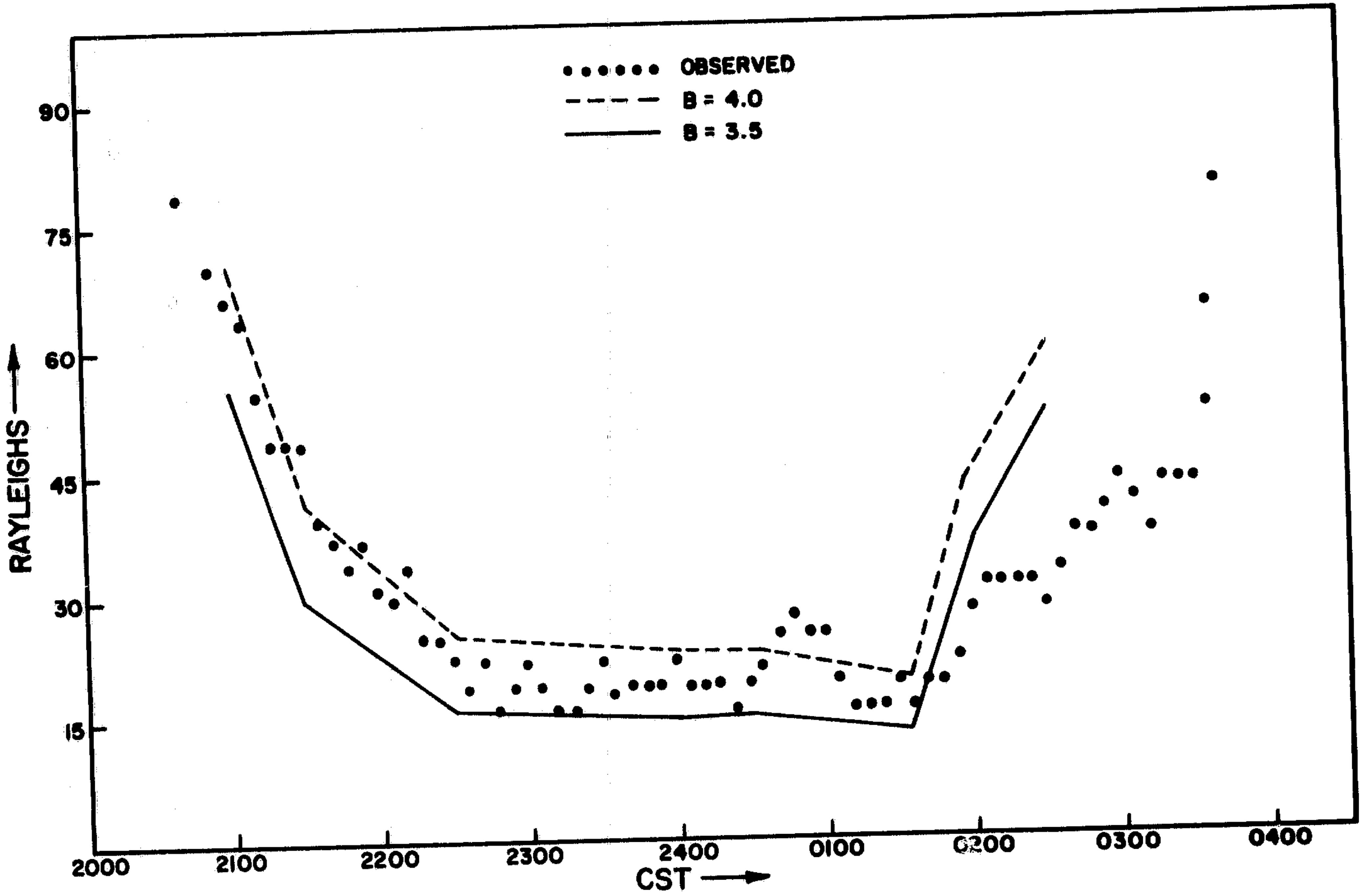

Figure 7.4 Comparison of observed OI(6300Å) intensities with intensities calculated from Barbier's formula.

7.2 Comparison with Results of other Workers

Gulledge, et al. (1968) used the rocket technique to observe a layer of red-line emission with peak emission rate at 245 km and half-width of about 75 km. Lagos, et al. (1963) have made theoretical calculations of parameters describing the emission layer under magnetically quiet conditions assuming the excitation of $O(^1D)$ is due to dissociative recombination, and the electron density profile approximates a Chapman layer. They have shown that the peak of the ε_D height distribution should be about 1.6 atomic oxygen scale heights below the F2-layer peak, and that the half-width of the ε_D height distribution is equal to 1.5 atomic oxygen scale heights. Figure 7.1 yields figures of 1.1 and 1.6 respectively for these quantities.

Peterson and Steiger (1966) have compared nightglow measurements with OI(6300Å) intensities calculated from simultaneously taken ionograms at Maui, Hawaii, and estimate that K_{D_1} be on the order of .1. This is in excellent agreement with the conclusions made in Section 7.1.

Zipf (1969) has studied the dissociative recombination of O_2^+ in the laboratory and has found the branching ratio for the production of ^3P, ^1D, and ^1S oxygen atoms at 300K and not including cascading effects to be 1.00:0.90:0.10 respectively. Since the ^1S state has a lifetime of .74 seconds, quenching of $O(^1S)$ is negligible at F region altitudes, and it is safe to assume that all $O(^1S)$ undergoes radiative transition to $O(^1D)$ with emission of a 5577Å photon. Therefore, including the $^1S \rightarrow {}^1D$ cascading effect, Zipf's measurements indicate that $K_{D_1} = 1.0$. This is nearly an order of magnitude larger than the result presented in Section 7.1, and implications of this disagreement are discussed below.

From observed airglow intensities and Equation (3.26), Zipf's value of $K_{D_1} = 1.0$ implies that the quenching coefficient be as high as 1×10^{-9} cm^3 sec^{-1}. This is too much larger than laboratory and aeronomical calculations of $S_D(N_2)$ to be plausible. Therefore, either $K_{D_1} = 1.0$ is not appropriate for use at temperatures as high as 1000K, or the quantities utilized in Equation (3.26) are in error. Zipf's measurements were made at 300K, and it is possible that K_{D_1} could decrease significantly from its value at 300K to 1000K. Also, inaccuracies in γ_1 and the model atmosphere could account for some of the difference between the results of this analysis and Zipf's measurements. The rate coefficient γ_1 has been determined in the laboratory by several workers (Bohme et al., 1967; Dunkin et al., 1968; Fehsenfeld et al., 1965; Warneck, 1967) and appears to be fairly well known. An approximate check on the model atmosphere will be made in the following.

7.3 A Check on the Atmospheric Model

Assuming the electron density several hours after sunset may be approximated by (see Section 5.3.2)

$$[e] = [e]_o \, e^{-\lambda_o t} , \qquad (7.2)$$

and utilizing Dungey's (1956) solution for the lowest eigenvalue:

$$\lambda_o = 1.06 \left\{ \frac{D_o \beta_o^{1/2}}{4 H_1^2} \right\}^{2/3} \qquad (7.3)$$

the atmospheric model may be checked by comparing values of λ_o determined from actual electron density profiles with those calculated from Equation (7.3). Under the assumption of diffusive equilibrium for [O] and $[O_2]$,

$$\beta(z) = \gamma_1[O_2] = \gamma_1[O_2]_0 1^{-2z/H_1} = \beta_{0e}^{-2z/H_1} \qquad (7.4)$$

$$D(z) = \frac{7.3 \times 10^{18}}{[O]} = \frac{7.3 \times 10^{18}}{[O]_0} e^{z/H_1} = D_o e^{z/H_1} \qquad (7.5)$$

Therefore

$$D(z)\beta(z)^{1/2} = D_o\beta_o^{1/2}$$

is a height-independent quantity. From the model atmosphere for T_∞ = 1100K,

$$D_o\beta_o^{1/2} = 2.3 \times 10^{18} \quad ,$$

and substitution into (7.3) yields $\lambda_o = 1.12 \times 10^{-4}$ sec^{-1}. For this model atmosphere and the shape-preserving solution,

$$\lambda_o = \beta(z) = \gamma_1[O_2]$$

at some altitude z'. For $\lambda_o = 1.12 \times 10^{-4}$ sec^{-1} and $\gamma_1 = 2.5 \times 10^{-11}$ cm^3 sec^{-1}, $[O_2] = 4.5 \times 10^6$ cm^3. From the model atmosphere this implies z' = 335 km. Now the actual electron density vs. time curves given in Figure 5.13 indicate a value of $\lambda_o = 2.77 \times 10^{-4}$. Therefore, at 335 km, $[O_2] = 1.1 \times 10^7$ cm^{-3}. Thus the molecular oxygen concentration deduced from the experimental data is about a factor of two greater than the value obtained from the shape-preserving electron density height distribution and the atmospheric model. If a greater molecular oxygen concentration were used in the calculations, a smaller value of K_{D_1} would have been obtained from Equation (3.26). This causes even greater disagreement with Zipf's measurements. It is concluded that much of the disagreement between the results of this analysis and those of Zipf's laboratory measurements is probably due to the temperature dependence of K_{D_1}. This is not a surprising result since the rate of the dissociative recombination of O_2^+ decreases with increasing temperature (Kasner and Biondi, 1968). However, final conclusions as to the temperature dependence of K_{D_1} should not be made until further laboratory and aeronomical measurements are in agreement.

7.4 Suggestions for Future Work

7.4.1 Predawn enhancements

The OI(6300Å) airglow can undergo sunrise and presunrise effects due to excitation of $O(^1D)$ by inelastic collisions of photoelectrons with atomic oxygen (see Section 2.3). Since the efficiency of the dissociative recombination of O_2^+ in producing $O(^1D)$ and the rate coefficient for quenching of $O(^1D)$ are approximately known, it is possible to calculate the OI(6300Å) emission due to the dissociative recombination of O_2^+ providing the electron density height distribution and exospheric temperature are known. Any contributions which are observed which are in excess of this contribution are due to other means of excitation of $O(^1D)$, such as inelastic collisions of photoelectrons with atomic oxygen. Thus the flux of photoelectrons needed to produce the required amount of 6300Å emission may be calculated, and the onset time of the enhancement together with the magnetically conjugate sunrise time will indicate whether the observed effect is due to locally produced photoelectrons, or photoelectrons produced in the magnetically conjugate sunlit ionosphere. If possible, observations of the predawn enhancement in red line intensity should be accompanied by measurement of the temperature of the F region. The temperature and red-line intensity should increase in unison.

7.4.2 Correlation of OI(6300Å) with other emissions

The OI(5577Å) emission is produced by the $^1S \rightarrow {}^1D$ transition of atomic oxygen. The Chapman reaction (Chamberlain, 1961):

$$O + O + O \rightarrow O(^1S) + O_2 \qquad (7.5)$$

accounts for the production of $O(^1S)$ in the 90 km to 110 km region of the atmosphere and additional $O(^1S)$ is produced in the F region by the dissociative recombination of O_2^+ (Peterson et al., 1966):

$$O_2^+ + e \rightarrow O(^1S) + O(^1D) \qquad (7.6)$$

The dissociative recombination of O_2^+ is the same mechanism responsible for OI(6300Å), and thus similar intensity variations might be observed between OI(5577Å) and OI(6300Å). This correlation may be impeded, however, by the predominance of reaction (7.5). Nevertheless, such a correlation may be possible under unusual atmospheric conditions, and these are often the most interesting and informative. For instance, it would be interesting to observe the green line while the red-line intensity was undergoing a pre-dawn enhancement. Excitation to $O(^1S)$ would require a more energetic flux of photoelectrons than is necessary to produce $O(^1D)$, and observation of any similar variations of OI(6300Å) and OI(5577Å) might give some indication as to the energy distribution of incoming photoelectrons.

The NI(5199Å) emission is produced by the $^2D \rightarrow {^4S}$ transition of atomic nitrogen. The dissociative recombination of NO^+ is energetically capable of the following:

$$NO^+ + e \longrightarrow N(^2D) + O(^3P) \qquad (7.7)$$

$$NO^+ + e \longrightarrow N(^4S) + O(^1D) \qquad (7.8)$$

$$N(^2D) + O(^3P) \longrightarrow N(^4S) + O(^1D) \quad . \qquad (7.9)$$

Dalgarno and Walker (1964) argue that reaction (7.8) violates conservation of spin. However, it was shown in Section 7.1 that as little as .01 excitations of $O(^1D)$ per recombination of NO^+ could contribute 10% of the total OI(6300Å) night airglow. This is sufficient justification to warrant study of reactions (7.7) to (7.9). Simultaneous observation of OI(6300Å) and NI(5199Å), in conjunction with theoretical calculations of the integrated emission rates, could provide valuable information on the relative importance of reactions (7.7) to (7.9). It is therefore suggested that an attempt be made to obtain a 5199Å interference filter for a sufficient period of time to carry out this study.

7.4.3 Time variations of OI(6300Å)

It is suggested that measurements of the OI(6300Å) night airglow continue on a periodic basis at the Urbana station. After sufficient data is accumulated, it will be possible to attempt correlations of OI(6300Å) behavior with solar activity, season, and geomagnetic activity. In addition, OI(6300Å) behavior at sunrise and twilight may offer valuable information on processes occurring in the upper atmosphere such as dissociative recombination, electron impact, and photodissociation; all of which contribute to OI(6300Å) in the presence of the sun's radiation (Noxon, 1968).

7.4.4 $O(^1D)$ in the atmospheres of Mars and Venus

The singlet state of atomic oxygen is produced by the photolysis of carbon dioxide:

$$CO_2 + h\nu \longrightarrow CO + O(^1D) \tag{7.10}$$

in the atmospheres of Mars and Venus (Shimizu, 1968). Shimizu reviews evidence suggesting constituents capable of quenching $O(^1D)$, such as CO_2, CO, N_2, and O_2. The amount of 6300Å emission which is radiated closely depends on the concentrations of the reactants responsible for producing O(^{1}D) and also on the concentration and efficiency of available quenching agents. Measurements of the 6300Å emission from Mars and Venus will no doubt provide a valuable complement to existing information and future measurements on the photochemistry and composition of their atmospheres. If sufficient data is available, an interesting problem would be to calculate the volume emission rate of OI(6300Å) from these planets, based on experimental, laboratory, and theoretical evidence. Perhaps several possible model atmospheres could be used, and in conjunction with eventual satellite measurements of OI(6300Å), the composition and processes of the atmospheres of Mars and Venus might be better understood.

REFERENCES

Balsley, B. B. (1969), Nighttime electric fields and vertical ionospheric drifts near the magnetic equator, J. Geophys. Res. 74, 1213-1217.

Barbier, D. (1959), Recherches sur la raie 6300 de la luminescence atmospherique nocturne, Ann. Geophys. 15, 179-217.

Bates, D. R. (1946), The origin of the night sky light, Monthly Notices Roy. Astron. Soc. 106, 509-514.

Bates, D. R. (1959), Some problems concerning the terrestrial atmosphere above about the 100 km level, Proc. Roy. Soc. London A253, 451-462.

Bates, D. R. and A. Dalgarno (1953), The altitudes of the luminous layers in the Earth's atmosphere, J. Atmos. Terrest. Phys. 4, 112-123.

Bellew, W. and S. Silverman (1966), General behavior of 6300Å [OI] at Sacramento Peak, New Mexico, Planet. Space Sci. 15, 407-416.

Benson, S. W. (1960), *The Foundations of Chemical Kinetics*, McGraw-Hill, New York.

Blacker, H. V. and M. Gadsden (1966), On the calibration of airglow photometers, Planet. Space Sci. 14, 921-928.

Blacker, H. V. and M. Gadsden (1967), The calibration of airglow photometers, ESSA Technical Memorandum IERTM-ITSA 85.

Blifford, I. H., Jr. (1966), Factors affecting the performance of commerical interference filters, Applied Optics 5, 105-111.

Bohme, D. K., P. P. Ong, J. B. Hasted and L. R. Megill (1967), Energy dependence of reactions of O^+ with N_2, O_2 - I. Drift tube experiments, Planet. Space Sci. 15, 1777-1780.

Broadfoot, A. L. and K. R. Kendall (1968), The airglow spectrum, 3100-10,000Å, J. Geophys. Res. 73, 426-428.

Budden, K. G. (1954), A method for determining the variation of electron density with height (N(z) curves) from curves of equivalent heights against frequency ((h',f) curves), Rept. Phys. Soc. Conf. on Physics of the Ionosphere, Cambridge, England, 332-339.

Carlson, H. C. (1966a), Evidence for a magnetic conjugate point origin of ionospheric heating, *Electron Density Profiles in Ionosphere and Exosphere*, ed. J. Frihagen, North-Holland Publishing Company, Amsterdam, 478-492.

Carlson, H. C. (1966b), Ionospheric heating by magnetic conjugate-point photoelectrons, J. Geophys. Res. 71, 195-199.

Chamberlain, J. W. (1961), Physics of the Aurora and Airglow, Academic Press, New York.

Cole, K. D. (1965), The pre-dawn enhancement of 6300Å airglow, Ann. Geophys. 21, 156-158.

Dalgarno, A. (1965), Ambipolar diffusion in the F region, J. Atmosph. Terrest. Phys. 26, 939.

Dalgarno, A. and J. C. G. Walker (1964), The red line of atomic oxygen in the day airglow, J. Atmosph. Sci. 21, 463-474.

Davis, T. N. and L. L. Smith (1965), Latitudinal and seasonal variations in the night airglow, J. Geophys. Res. 70, 1127-1138.

Demore, W. and O. F. Raper (1962), Reaction of $O(^1D)$ with nitrogen, J. Chem. Phys. 37, 2048-2052.

Demore, W. and O. F. Raper (1964), Deactivation of $O(^1D)$ in the atmosphere, Astrophys. J. 139, 1381-1383.

Doupnik, J. R. and E. R. Schmerling (1965), The reduction of ionograms from the bottomside and topside, J. Atmos. Terrest. Phys. 27, 917-941.

Dungey, J. W. (1956), The effect of ambipolar diffusion in the nighttime F layer, J. Atmos. Terrest. Phys. 9, 90-102.

Dunkin, D. B., F. C. Fehsenfeld, A. L. Schmeltekopf and E. E. Ferguson (1968), Ion-molecule reaction studies from 300°K to 600°K in a temperature-controlled flowing afterglow system, J. Chem. Phys. 49, 1365.

Fehsenfeld, F. C., P. D. Goldan, A. L. Schmeltekopf, and E. E. Ferguson (1965), Laboratory measurement of the rate of the reaction $O^+ + O_2 \rightarrow O_2^+ + O$ at thermal energy, Planet. Space Sci. 13, 579-582.

Fish, R. M. and S. A. Bowhill (1968), Instrumentation for the measurement of airglow, Aeronomy Report No. 26, Aeronomy Laboratory, Urbana, Illinois.

Gadsden, M. (1964), On the twilight sodium emission - I. Observations from a Southern hemisphere station, Ann. Geophys. 20, 261-272.

Gadsden, M. (1965), Some statiscal properties of pulses from photomultipliers, Appl. Opt. 4, 1446-1452.

Greenspan, J. A. (1966), Synoptic description of the 6300Å nightglow near 78° West longitude, J. Atmosph. Terrest. Phys. 28, 739-745.

Gulledge, I. S., D. M. Packer, S. G. Tilford and J. T. Vanderslice (1968), Intensity profiles of the 6300Å and 5577Å OI lines in the night airglow, J. Geophys. Res. 73, 5535-5547.

Hanson, W. B. (1963), Electron temperatures in the upper atmosphere, Space Research III, ed. W. Priester, 282-302.

Hunten, D. M. and M. B. McElroy (1966), Quenching of metastable states of atomic and molecular oxygen and nitrogen, Rev. Geophys. 4, 303-328.

Johnston, H. S. (1966), Gas Phase Reaction Rate Theory, Ronald Press Co., New York.

Kasner, W. H. and M. A. Biondi (1968), Temperature dependence of the electron - O_2^+ ion recombination coefficient, Phys. Rev. 174, 139-144.

Kulkarni, P. V. and C. L. Sanders (1964), Use of a radioactivated light source for the absolute calibration of two-color night airglow photometer, Planet. Space Sci. 12, 189-194.

Lagos, P., W. Bellew, and S. M. Silverman (1963), The 6300Å [OI] emission theoretical considerations on the luminosity profile, J. Atmosph. Terrest. Phys. 25, 581-587.

Laidler, K. J. (1950), Chemical Kinetics, McGraw-Hill, New York.

McGrath, W. D. and J. J. McGarvey (1967), Reactions of $O(^1D)$ atoms, Planet. Space Sci. 15, 427-455.

Nakamura, T. (1961), Latitude effect of the oxygen red line of night airglow and its relation with the ionospheric F-layer, Rept. of Ionosphere and Space Res. in Japan 15, 245-252.

Noxon, J. F. (1968), Day airglow, Space Sci. Rev. 8, 92-134.

Peterson, V. L. (1968), Comments on Barbier's formula for the intensity of the 6300Å nightglow, Ann. Geophys. 24, no. 1, 101-107.

Peterson, V. L. and W. R. Steiger (1966), F-region nightglow emissions of atomic oxygen. 2. Analysis of 6300Å and electron density data, J. Geophys. Res. 71, 2267-2277.

Peterson, V. L. and T. E. VanZandt (1969), $O(^1D)$ quenching in the ionospheric F-region, Planet. Space Sci. 17, 1725-1736.

Peterson, V. L., T. E. VanZandt and R. B. Norton (1966), F-region nightglow emissions of atomic oxygen. 1. Theory, J. Geophys. Res. 71, 2255-2265.

Purdy, C. M., L. R. Megill and F. E. Roach (1961), A new airglow photometer, J. Res. NBS 65c, 213-216.

Roach, F. E. and L. L. Smith (1967), The worldwide morphology of the atomic oxygen nightglow, Aurora and Airglow, ed. B. M. McCormac, Reinhold Publishing Corp. New York, 29-40.

Seaton, M. J. (1958), Oxygen red lines in the airglow. II. Collisional deactivation effects, Astrophys. J. 127, 67-74.

Shimizu, M. (1968), The recombination of CO and O in the upper atmospheres of Mars and Venus, Icarus 9, 593-597.

Smith, L. L. and W. R. Steiger (1968), Night airglow intensity variations in the [OI] 5577Å, [OI] 6300Å, and NaI 5890-96Å emission lines, J. Geophys. Res. 73, 2531-2538.

Snelling, D. R. and E. J. Blair (1967), Nonadiabatic decomposition of N_2O in the deactivation of $O(^1D)$ by N_2, J. Chem. Phys. 47, 228-234.

Stein, J. A. and J. C. G. Walker (1965), Models of the upper atmosphere for a wide range of boundary conditions, J. Atmos. Sci. 22, 11-17.

U. S. Standard Atmosphere Supplements (1966), U. S. Government Printing Office, Washington, D. C.

VanZandt, T. E. and V. L. Peterson (1968), Detailed maps of tropical 6300Å nightglow enhancements and their implications on the ionospheric F2 layer, Ann. Geophys. 24, no. 3, 747-759.

Wallace, L. and M. B. McElroy (1966), The visual dayglow, Planet. Space Sci. 47, 677-708.

Warneck, P. (1967), Studies of ion-neutral reactions by a photoionization mass spectrometer technique - III. Several ionospheric reactions, Planet. Space Sci. 15, 1349-1359.

Weller, C. S. and M. A. Biondi (1968), Recombination, attachment, and ambipolar diffusion of electrons in photoionized NO afterglows. Phys. Rev. 172, 198-206.

Wright, J. W. (1962), Diurnal and seasonal changes in structure of the mid-latitude quiet ionosphere, J. Res. NBS 66D, 297-312.

Young, R. A., G. Black and T. G. Slanger (1968), Reaction and deactivation of $O(^1D)$, J. Chem. Phys. 49, 4758-4768.

Zipf, E. C. (1968), Collisional deactivation of metastable atoms and molecules in the upper atmosphere, presented at the International Assoc. of Geomagnetism and Aeronomy Symposium on Laboratory Measurements of Aeronomic Interest, York University, Toronto, Canada.

Zipf, E. C. (1969), The dissociative recombination of O_2^+ ions into specifically identified final atomic states, to be published, Bull. Am. Phys. Soc.